# NEW INSIGHTS INTO HEME PEROXIDASES: INTERMEDIATES AND MECHANISMS

Thesis submitted for the degree of Doctor of Philosophy

at the University of Leicester

by

ANDREA GUMIERO

Department of Chemistry

Faculty of Science

University of Leicester

April 2011

*In memoriam*

*Ugo and Antonietta*

# STATEMENT

Unless otherwise acknowledged, the experimental work described in this thesis has been carried out by the author in the department of Chemistry and Henry Wellcome laboratories for Structural Biology, at the University of Leicester between October 2007 and March 2011. The work has not been submitted and is not presently being submitted for any other degree at this or any other university.

Signed: Date:

Department of Chemistry
University of Leicester
University Road Leicester
United Kingdom
LE1 7RH

# NEW INSIGHTS INTO HEME PEROXIDASES: INTERMEDIATES AND MECHANISMS

Andrea Gumiero

## ABSTRACT

Heme peroxidises catalyse the $H_2O_2$-dependent oxidation of substrates in a two-step process, through formation of two oxy-ferryl intermediates known as Compound I and Compound II. Despite the considerable effort worldwide, important aspects about the reactivity of these enzymes are still to be clarified. Amongst all, the determination of the nature of the Fe-O bond in the oxy-ferryl intermediates, as well as the mechanism by which protons are delivered to the oxy-ferryl species during turnover, are of highest relevance. In this thesis, high resolution crystal structures of both Compound I and Compound II intermediates in two heme peroxidases, cytochrome *c* peroxidase (C*c*P) and ascorbate peroxidase (APX), are presented. In order to rule out the photoreduction arising from X-ray exposure during data collection, which causes alteration of ferryl intermediate structures, a multicrystal method has been employed. Results indicate that Compound I, with an Fe-O distance of 1.63 Å for C*c*P and 1.73 Å for APX, is consistent with an unprotonated oxy-ferryl species ($Fe^{IV}$=O), whereas Compound II, with an Fe-O bond length of 1.83 Å and 1.84 Å for C*c*P and APX respectively, is consistent with a protonated oxy-ferryl species ($Fe^{IV}$-OH). Also presented in this thesis is the 2.40 Å structure of resting ferric C*c*P at room temperature obtained, for the first time, by neutron crystallography. This study allowed to establish the location of individual, exchangeable hydrogen atoms thus revealing the protonation states of several key active site residues in the distal (Arg48, Trp51, His52) and proximal (His163, Trp191, Asp235) heme regions. This information was used to revise the reaction mechanism of heme peroxidases and also to infer a possible delivery pathway of protons during turnover. All together, these data not only clarify long-standing inconsistencies on the nature of the oxy-ferryl species, but they also provide new insights into the reaction mechanism of heme peroxidases and provide important information which may apply to other categories of heme enzymes such as the cytochromes P450 and NO synthases.

# ACKNOWLEDGMENTES

I would like to thank my supervisors Professor Emma Raven and Dr Peter Moody for their support and help throughout my PhD. Their presence and their patient guidance have been not only the source of a precious scientific training, but also of an enriching life experience.

Special thanks go to Dr Sara Rafice, Dr Igor Efimov and Sameeh Al-Sarayreh for their friendship, advice, encouragement and support. I could not have made it through without them. I would also like to thank Dr Sandip Badyal, Dr Jaswir Basran and Mrs Nina Bhanji for their friendship and advice.

I am very grateful to Dr Matthew Blakeley, for collecting neutron crystallographic data and determining the structure of ferric C*c*P, and Dr Harriet E. Seward for EPR data on APX mutants.

Many thanks to Dr Wei-Cheng Huang and Dr Jackie Ellies, for the enjoyable group meetings, the help and all the discussions about cytochromes P450, and Dr Sarah Thackray for the long discussions about enzymes and the lovely dinners at "*Wagamama*".

A very special thank to the friends of my "*little Italy in Leicester"*, for their loyalty and for giving me the chance to smile even in the hardest moments.

I gratefully acknowledge the Leverhulme trust for funding this project.

# TABLE OF CONTENTS

# CHAPTER ONE

# CHAPTER TWO

# CHAPTER THREE

# CHAPTER FOUR

# CHAPTER FIVE

# LIST OF FIGURES

# LIST OF SCHEMES

# LIST OF TABLES

# ABBREVIATIONS

Amino Acids are abbreviated according to the three-letter codes recommended by the I.U.P.A.C Joint Commission on Biochemical Nomenclature (1985).

ENZYMES

| | |
|---|---|
| APX | Soybean ascorbate peroxidase |
| ARP | *Arthromyces ramous* peroxidase |
| BP1 | Barley peroxidase |
| KatG | Catalase peroxidase |
| C*c*P | Cytochrome *c* peroxidase |
| CPO | Chloroperoxidase |
| HRP | Horseradish peroxidase |
| LPO | Lactoperoxidase |
| LiP | Lignin peroxidase |
| MnP | Manganese peroxidase |
| MPO | Myeloperoxidase |
| NOS | NO synthase |
| PnP | Peanut peroxidase |
| P450 | Cytochrome P450 |
| TPO | Thyroid peroxidase |
| DNase | Deoxyribonuclease |

CHEMICALS

| | |
|---|---|
| Amp | Ampicillin |
| EDTA | Ethylenediaminetetraacetic acid |
| HEPES | *N*-2-Hydroxyethylpiperazine-*N*′-2-ethanesulphonic acid |
| IPTG | Isopropyl-β-D-thiogalactopyanoside |
| INH | Isoniazid |
| Kan | Kanamycin |
| KPi | potassium phosphate buffer |
| LB | Luria-Bertani broth |

| | |
|---|---|
| MPD | (±)-2-Methyl-2,4-pentanediol |
| PMSF | Phenylmethylsulphonyl fluoride |
| SHA | Salicylhydroxamic acid |
| SDS | Sodium dodecyl sulphate |
| THEMED | *N,N,N′,N′*-T etramethylethylenediamine |
| Tris | Trizma base (tri[hydroxymethyl]aminomethane) |

SYMBOLS

| | |
|---|---|
| A | Absorption |
| ε | Absorption coefficient |
| $K_a$ | Acidic dissociation constant |
| CT | Charge transfer |
| $K_d$ | Dissociation constant |
| rpm | Revolutions per minute |
| λ | Wavelength |

TECHNIQUES

| | |
|---|---|
| EPR | Electron paramagnetic resonance |
| ENDOR | Electron Nuclear DOuble Resonance |
| EXAFS | Extended X-ray Absoprtion Fine Structure |
| FPLC | Fast protein liquid chromatography |
| MALDI-TOF | Matrix-Assisted Laser Desorption/Ionisation - Time Of Flight |
| SDS-PAGE | Sodium dodecyl sulphate - polyacrylamide gel electrophoresis |
| UV-visible | Ultra violet- visible light spectroscopy |
| XAS | X-ray absorbance spectroscopy |

CRYSTALLOGRAPHY-RELATED SYMBOLS

| | |
|---|---|
| CCD | Charge-coupled device |
| CCP4 | Collaborative Computational Project No. 4 |
| Cukα | Cu X-ray source (λ = 1.5418 Å) |
| D-Lab | Laboratory for expression of deuterated proteins at ILL |
| DLS | Diamond Light Source |

| | |
|---|---|
| ESRF | European Synchrotron Radiation Facility |
| $F_o$ ($F_{obs}$) | Amplitude of observed structure factor |
| $F_c$ ($F_{calc}$) | Amplitude of calculated structure factor |
| ILL | Institute Laue-Langevin |
| Mok$\alpha$ | Mo X-ray source ($\lambda$ = 0.70926 Å) |
| PDB | Protein Data Bank |
| RMSD | Root-mean-square deviation |

FACILITIES

| | |
|---|---|
| PNACL | Protein and Nucleic Acid Chemistry Laboratory |
| PROTEX | Protein expression laboratory |

Chapter 1

# INTRODUCTION

Iron is the $26^{th}$ element of the periodic table, it belongs to the $6^{th}$ group of the transition metals and has an external electronic configuration $4s^2 3d^6$. From the point of view of physics, iron is the most stable element of the periodic table and as such, it is the eventual product of all the nuclear reactions (fission and fusion) that occur in the whole Universe. This is the reason why iron is the $4^{th}$ most abundant element of the earth's crust and one of the most abundant elements in the whole Universe (*1*).

Nature has evolved taking advantage of the high availability of iron. Owing to the reducing, oxygen-free, earth's primordial atmosphere, only ferrous iron ($Fe^{2+}$) was available and the first organisms incorporated and used this soluble ion for their metabolisms. However, when these organisms started to produce and release oxygen, the earth's atmosphere slowly changed and acquired an oxidative character. Ferrous ions were then oxidised and consequently the less soluble ferric species appeared; organisms had hence to adapt and revise the way iron had been handled so far. Eventually evolution led to systems where ferric ions were transported, stored and used as complexes, with iron coordinated to ligands, either small or large, or trapped inside proteins, by coordinating the side chains of specific residues like histidine, glutamic acid and cysteine. In the end, iron spread and became a crucial element for life in general, and nowadays it is known to be at the basis of a huge variety of biological processes (catalysis, cell signalling, regulation, oxygen transport, just to mention a few). Indeed, it is this widespread presence that draws the attention of the scientific community and also puts iron in a crucial position with respect to a number of different pathologies.

The different iron-containing proteins can be classified into two large families, on the basis of the iron-coordination system. The first one is that of heme-containing proteins, where iron is complexed to a porphyrin ring whereas the second family is that of non-heme iron containing proteins, amongst which are sulphur-iron containing clusters (*1*). Whilst the second is mainly made of electron transfer proteins, iron storage and iron transport proteins, the family of heme-containing proteins includes quite a large variety of specialised proteins, whose activity ranges from oxygen transport, to electron transfer and to oxygen activation in metabolic processes. This thesis focusses only on the first family of heme-containing proteins and some more precise aspects are discussed below.

## 1.1. HEME AND HEME-CONTAINING PROTEINS

Amongst all the methods Nature has developed to store, carry and use iron, chelation with porphyrins is certainly one of the most widespread and important.

Heme is actually the result of the complexation of iron into a large, unsaturated macrocyclic molecule, the "*protoporphyrin*". In Nature different *protoporphyrin* rings can be found and therefore different types of heme exist. Every *protoporphyrin* ring presents the same main structure, made of four pyrrole rings linked to each other by methene bridges, and differ only for the substituents bound outside the ring. The geometry of the whole macrocycle is planar and the iron, placed at the centre of the protoporphyrin ring, is coordinated to the nitrogen atoms of the four pyrrole rings (Figure [1. 1]). In this thesis only the iron-*protoporphyrin IX* complex, that is known as "heme *b"* (Figure [1. 1]), will be considered and it will be referred to as heme. The

*protoporphyrin IX* is a porphyrin ring distinguished by the four methyl groups at positions 1, 3, 5, 8, two vinyl groups at positions 2 and 4, and, finally, two propionates side chains at positions 6 and 7 (Figure [1. 2]). The *protoporphyrin IX* can coordinate either a ferric ion, in which case the complex is referred to as *hemin*, or a ferrous ion, in which case the complex would be the *heme*. However, it is nowadays quite established to refer to both the ferric and ferrous iron-protoporphyrin complexes as heme.

The geometry of the heme coordination allows the iron to accept two more ligands, above and below the heme plane. The two positions are generally indicated as fifth, or proximal, and sixth, or distal (Y and X respectively in Figure [1. 2]). The ligands occupying these positions change depending on the protein's family and can either be endogenous (when provided by the protein through the side chain of an amino acid) or exogenous (when it is not part of the polypeptidic chain). The proximal ligand is usually endogenous and it is often conserved amongst members of the same family, perhaps as a consequence of a linear evolution from a common ancestor. Evolution has selected, for this position, specific ligands, all able to modulate the chemical properties of the heme, on the basis of the physiological role of the enzyme. In hemoglobin and peroxidases, for instance, the proximal position is occupied by the imidazole ring of the side chain of a histidine whereas in cytochromes P450 the proximal ligand is always a thiolate (from the side chain of a cysteine). On the other hand, the distal position is occupied by endogenous ligands only in some specific cases (the electron transfer proteins cytochromes *b* or *c* for, instance), but in general it is left empty in order to accommodate an exogenous ligand (*e.g.* oxygen for hemoglobins and cytochromes P450, or hydrogen peroxide for heme peroxidases). It is rather obvious that Nature

and the coordination of both proximal and distal ligands are "first level" of close interactions, which directly control the activity of the heme. However, it would be limiting not to consider that the properties of the heme and the activity of the whole protein are also the result of a complex system of interactions occurring on a larger scale (network of hydrogen bonds, polar and apolar interactions, presence or absence of covalent bonds between the heme and the protein, *etc.*), which finely tune the chemical properties of each enzyme and reflect in the large variety of functions heme proteins perform in Nature. Heme enzymes such as the cytochromes P450 (*2*) are responsible for very important oxidative processes in human metabolism (*i.e.* hydroxylation of a large variety of organic substrates), while proteins like hemoglobin are the preferred oxygen transporters in all vertebrates (*1*). Heme proteins are also involved in cell-signalling, nitric oxide (NO) synthesis, hydrogen peroxide and radical scavenging, electron transfer and many other functions (*1*). Despite this extensive variety and complexity, heme proteins can be classified in three groups:

1. *Oxygen carriers*, like hemoglobin, myoglobin and other globular heme carriers such as dehaloperoxidase (DHP);

2. *Electron transfer proteins*, represented by proteins such as the cytochrome *b* and cytochrome *c*;

3. *Oxygen activator enzymes*, family that contains enzymes like the cytochromes P450, NO synthase, heme catalases, heme peroxidases and heme oxygenases.

The studies presented in this thesis relate to the heme peroxidases and more detailed information on these enzymes will be provided and discussed in the sections.

**Figure [1. 1]: Structure of heme (namely iron-protoporphirin IX)**

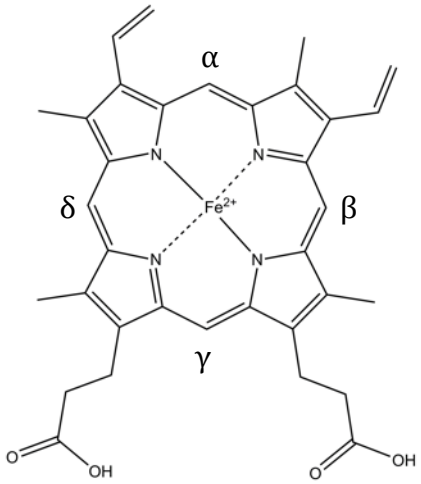


**Figure [1. 2]: Schematic representation of the heme plane (black line) showing the proximal position (Y) below the heme plane and distal position (X) above the heme plane.**

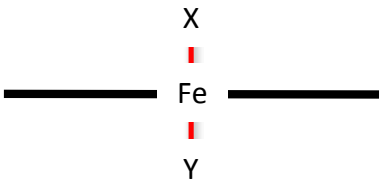

## 1.2. HEME PEROXIDASES

Hydrogen peroxide is usually formed in many organisms as a secondary product of oxygen-related metabolism, but its oxidative power is dangerous and organisms have developed ways to cope with this. Peroxidases are one of these responses that organisms have developed in response to this demand and their role is to reduce the hydrogen peroxide to water via the oxidation of various substrates. Furthermore, evolution has often taken advantage of the oxidative potential of the hydrogen peroxide and has employed peroxidases to carry out oxidations of resistant substrates such as lignin, for instance. Owing to their important role in preventing dangerous formation of radicals and oxidative stress, peroxidases are found in all organisms. Moreover, heme peroxidases are a group of enzymes of historical importance. Their activity and reaction mechanism have been long studied and the results used as a model for the interpretation of the reaction mechanism of many other heme enzymes.

Heme peroxidases were first classified by Welinder about 20 years ago (*3*). In this classification, the superfamily of mammalian peroxidases was identified and separated from a second superfamily, containing fungal, bacterial and plant peroxidases. The former, nowadays also referred to as the *peroxidase-cyclooxygenase* superfamily, has been recently re-organised on a genetic and phylogenetic bases (*4*) and contains enzymes like lactoperoxidase, myeloperoxidases and thyroid peroxidase. The latter, sometimes referred to as the *non-animal peroxidase* superfamily, is divided into three subfamilies, defined on the bases of structural characteristics:

**Class I** contains some plant (cytosolic, non secretory), yeast and bacterial peroxidases. Enzymes like ascorbate peroxidase (APX) and cytochrome *c* peroxidase (C*c*P), which are the main subjects of this thesis, belong to this family. Moreover, this is

also the class where the catalase-peroxidase (KatG) belongs. This enzyme has the peculiarity of catalysing the disproportion of hydrogen peroxide to water and oxygen. All the class I enzymes present a conserved structure, although their reaction mechanism might be different. The structure of these enzymes is rather simple and none of them contains carbohydrate chains, calcium ions or disulphide bridges.

**Class II** contains all the peroxidases secreted by fungal organisms and perhaps the most representative elements of this class are the lignin peroxidase (LiP) and manganese peroxidase (MnP). The enzymes of this family often show disulphide bridges and carbohydrates, together with Ca ions coordinated to the polypeptide chain.

**Class III** contains all the secretory plant enzymes. This is the family of one of the most important and studied heme peroxidase, horseradish peroxidase (HRP). This class is also made of more recently discovered peroxidases such as the barley peroxidase 1 (BP1). All these enzymes share common features like four disulphide bridges, carbohydrate chains and also N-terminal peptides for secretory control.

If evolution has led to a wide complexity of different enzymes capable of specific reactions and perfectly adapted to precise substrates and processes, it is also evident that some of the basic features are fundamentally conserved across all the classes and families of heme peroxidases and in some cases, heme proteins in general. These common features are discussed below.

### 1.2.1. THE ACTIVE SITE OF HEME PEROXIDASES: THE CONSERVED STRUCTURE

Despite the low primary structure similarity, heme peroxidases, mammalian and non-mammalian, show a highly conserved active site. First of all, the heme proximal

position is always occupied by a histidine, whose $N_\varepsilon$ coordinates the iron and the $N_\delta$ forms a hydrogen bond with the side chain of either an aspartic acid or an asparagine, respectively, in non-mammalian and mammalian peroxidases (Figure [1. 3]). It is interesting to note that the oxygen carrier proteins like hemoglobin show the same heme-histidine coordination on the proximal side, although there is no evidence for the common hydrogen bond network below the histidine. It is also interesting to observe that chloroperoxidase (CPO) represents an exception in the heme peroxidase superfamily as it has a proximal cysteine instead of a histidine, a feature typical of enzymes such as cytochromes P450. Focussing only on the family of non-animal peroxidases, conservation becomes more evident. Class I peroxidases show a longer, proximal hydrogen bond network, which extends from the carboxylic group of the conserved aspartic acid to the $N_\varepsilon$ of a tryptophan (Figure [1. 3]). In Class II and III the proximal tryptophan is replaced by phenylalanine. On the distal side, peroxidases show no endogenous ligand bound to the heme, but the $6^{th}$ position is usually occupied by a water molecule, weakly coordinated and easily exchanged with hydrogen peroxide during physiological activity. A conserved histidine appears above the distal water molecule (Figure [1. 3]) and it forms a hydrogen bond with the side chain of a conserved asparagine (Figure [1. 3]). Finally, the distal side of the Class I peroxidases also shows a conserved distal tryptophan that, likewise the proximal side, is replaced by a phenylalanine in Class II and Class III. It is important to point out that the conserved amino acids have all been observed to play important roles in the reaction mechanism of heme peroxidases (*5*) and most of them will be discussed in this work.

**Table [1. 1]: The conserved amino acids in heme peroxidases.**

| ***Class I*** | PDB code | Distal side | | | | Proximal side | | |
|---|---|---|---|---|---|---|---|---|
| **CcP** | 2XIL | Arg48 | Trp51 | His52 | Asn82 | His175 | Trp191 | Asp235 |
| **APX** | 1OAG | Arg38 | Trp41 | His42 | Asn71 | His163 | Trp179 | Asp208 |
| **KatG** | 2B2Q | Arg104 | Trp107 | His108 | Asn138 | His270 | Trp321 | Asp381 |
| ***Class II*** | | | | | | | | |
| **CiP** | 1H3J | Arg51 | Phe54 | His55 | Asn92 | His183 | Leu200 | Asp245 |
| **LiP** | 1B85 | Arg43 | Phe46 | His47 | Asn84 | His176 | Phe193 | Asp238 |
| **MnP** | 3M5Q | Arg42 | Phe45 | His46 | Asn80 | His173 | Phe190 | Asp242 |
| ***Class III*** | | | | | | | | |
| **HRP-C** | 1ATJ | Arg38 | Phe41 | His42 | Asn70 | His170 | Phe221 | Asp247 |
| **BP1** | 1BGP | Arg45 | Phe48 | His49 | Asn77 | His179 | Leu224 | Asp250 |

**Figure [1. 3]: Structure of the conserved active site of heme peroxidases (class I).**

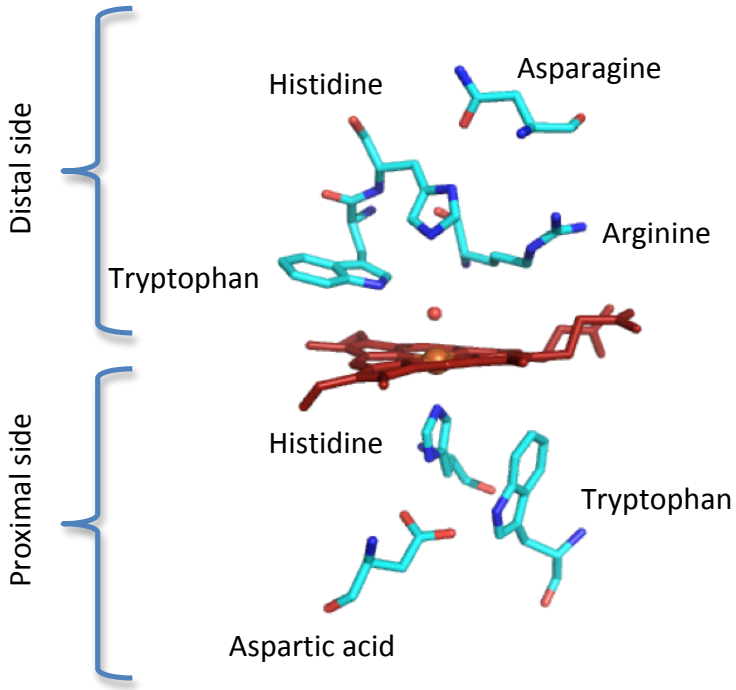

### 1.2.2. THE CONSERVED REACTION MECHANISM

Besides the high similarity of the active site structure, heme peroxidases have another very important aspect in common: the reaction mechanism. Generally speaking the process comprises three, sequential steps (Eq. 1, Eq. 2, Eq. 3).

$$\text{Enzyme} + H_2O_2 \longrightarrow \text{Compound I} + H_2O \qquad \textbf{Eq. 1}$$

$$\text{Compound I} + \text{Sub} \longrightarrow \text{Compound II} + \text{Sub}^{\bullet} \qquad \textbf{Eq. 2}$$

$$\text{Compound II} + \text{Sub} \longrightarrow \text{Enzyme} + \text{Sub}^{\bullet} + H_2O \qquad \textbf{Eq. 3}$$

At the beginning, the ferric heme of the resting protein is oxidised by hydrogen peroxide which undergoes a heterolytic cleavage (*6*). Hence, the reaction leads to the release of a water molecule and, most importantly, to formation of an intermediate known as Compound I (Eq. 1) that is 2-electron-equivalents more oxidised than the resting protein. The nature of Compound I has been the subject of a long debate in different proteins, not only in heme peroxidases. However extensive spectroscopic studies (*7-16*) have established that Compound I is made of an oxy-ferryl species ($Fe^{IV}$=O) and a radical, delocalised in most cases on the heme ring, to form a porphyrin π-cation and, in some cases, on the side chain of an amino acid. It must be added that before formation of Compound I, in some cases formation of another intermediate has been implicated (*17, 18*) and the species has been referred to as Compound 0 (see (*19*) for a review).

Compound 0 is thought to be formed as a precursor of Compound I in all cases and considered a very difficult species to trap, owing to its rapid decay to Compound I (*5*).

In the presence of a substrate, Compound I is reduced by one-electron to Compound II (Eq. 2), with loss of the heme/protein-based radical. Consequently, in the third step Compound II is finally converted back to the resting enzyme by oxidation of another molecule of substrate (Eq. 3). The precise nature of Compound I and Compound II will be discussed in detail later in Chapter 2.

Besides the intermediates observed during physiological activity, most heme peroxidases can form a further intermediate, generally indicated as the 'ferrous-oxy' species (also known as Compound III). Compound III can be obtained by reaction of Compound II with excess hydrogen peroxide (*20*) (Eq. 4) although it has also been observed as an unstable intermediate in the reaction of ferrous peroxidases with $O_2$ (*21*).

$$\text{Compound II} + H_2O_2 \longrightarrow \text{Compound III} + 2H_2O \qquad \textbf{Eq. 4}$$

# 1.3. TWO IMPORTANT HEME PEROXIDASES: CYTOCHROME *C* PEROXIDASE AND ASCORBATE PEROXIDASE

## 1.3.1. CYTOCHROME *C* PEROXIDASE

### *1.3.1.1. Introduction*

C*c*P is one of the most studied peroxidases (perhaps only second to HRP). First isolated from yeast mitochondria (*22*) in the '40s, it belongs to the Class I group of heme proteins and its role is to scavenge excess hydrogen peroxide in cells (*23*). Thanks to its ability to easily form large crystals (*24*), the C*c*P heme structure and

orientation was identified in 1978 and C*c*P was the first heme peroxidase to have its structure solved (*25*). When the structure was published, it provided considerable insight into the understanding of the reaction mechanism of the heme enzymes and it became a model for heme peroxidases and heme enzymes in general (*6*). As soon as other heme peroxidases were studied, however, it seemed clear that C*c*P was actually a very distinct enzyme as it differed from the general behaviour of the heme peroxidases in two main elements. First, Compound I of C*c*P does not show the classical porphyrin delocalised radical, but it instead has an indole radical on the side chain of the Trp191 (*26, 27*) and second, the substrate of C*c*P is not a small molecule, as for most heme peroxidases, but is actually a protein, cytochrome *c*. These two features will be discussed further in the next paragraphs.

*1.3.1.2. The nature of heme intermediates: tryptophan radical*

One important peculiarity of C*c*P lies in the location of the Compound I radical. Despite the general behaviour of heme peroxidases, which form a porphyrin π-cation radical upon reaction with hydrogen peroxide, C*c*P forms a protein radical identified on the Trp191 (*26, 27*). The peculiarity has been ascribed to the fact that, as opposed to other heme peroxidases, the substrate of C*c*P is another protein and evolution has adapted the protein to increase the efficiency of electron transfer. This is confirmed by the fact that ascorbate peroxidase (APX) has a structurally equivalent tryptophan residue, Trp179 (*28*), although a radical on this site has never been observed. It has been proposed that the absence of a tryptophan radical in APX could also be ascribed to the presence of a metal cation binding site close to the Trp179 (*29, 30*) and it has been partially confirmed by theoretical studies (*31*). Finally the stability of the Trp191

radical has been partially justified by the hydrogen bond formed between the $N_\varepsilon$ of the indole ring and the carboxylic group of the Asp235. ENDOR analysis has shown that upon formation of Compound I the proton of the $N_\varepsilon$ is not donated to the carboxylic group of the aspartic acid and remains on the indolic ring that becomes a cationic radical (*32*).

*1.3.1.3. The interaction with the substrate*

The physiological substrate of C*c*P is cytochrome *c*, a heme protein involved in the electron transfer chain of mitochondria. The study of the binding between C*c*P and cytochrome *c* has revealed the presence of two binding sites for cytochrome *c* (*33, 34*). The two sites appeared to have different affinities and electrostatic properties (*34*). The crystal structure of C*c*P in complex with Cytochrome *c* (*35*) (Figure [1. 4]-A) revealed one of the two sites and indicated that the most likely residues involved in binding are the acidic side chains of Glu290 and Aps34. However other studies identified more residues affecting this first binding site and the attention has focussed on Asp35 and Asp37 (*36*). On the other hand the lack of a crystal structure for the second binding site has made its identification a harder task and only the Lys149 has been identified as a potential residue involved in the binding (*37*). Moreover the weak binding activity of the second site (*34*) seems to indicate a possible non-physiological role for it. It is also important to note that the solved structure of the complex provided information that allowed the identification of the sequence of amino acids (Trp191, Gly192, Ala193 and Ala194) (*38, 39*) "wiring" the two heme groups together and accounting for the electron exchange between cytochrome *c* to C*c*P. This idea was also consistent with the radical delocalisation on the indole ring of the Trp191.

**Figure [1. 4]: Structure of the complex between A) C*c*P and cytochrome *c*, and B) APX and ascorbate.**

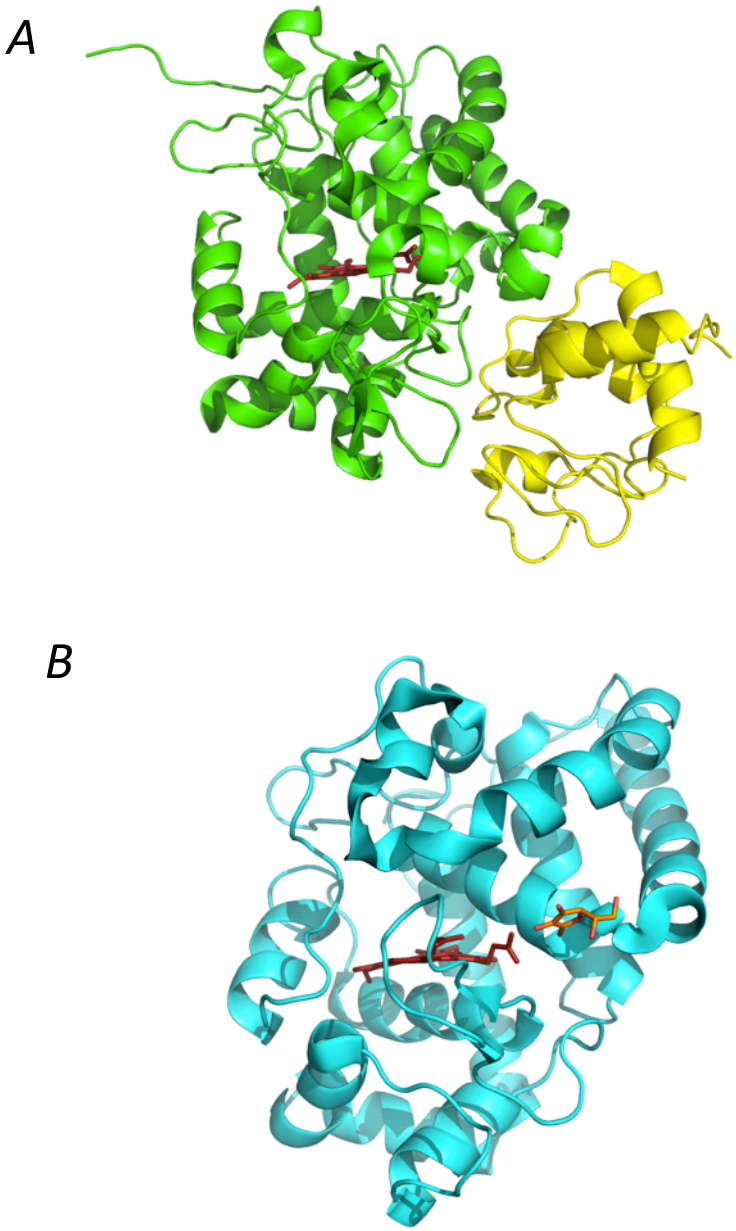


**Figure [1. 5]: The structure of ascorbate (Vitamin C)**

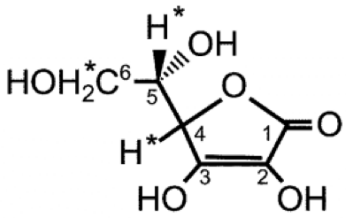

### 1.3.2. ASCORBATE PEROXIDASE

#### *1.3.2.1. Introduction*

Ascorbate peroxidase is one of the latest enzymes to have made its appearance on the scene of the heme research field and belongs to class I. It has been isolated from different species of plants and in all cases, either from chloroplasts (*40-50*) or cytosol (*51-60*), it has been observed to act as a scavenger of hydrogen peroxide by oxidation of ascorbic acid (vitamin C, Figure [1. 5]). Most of the structural and functional studies have been carried out on two cytosolic ascorbate peroxidases, one extracted from pea (pea-APX) and one from soy (soy-APX). Pea-APX was purified and sequenced a few years ago (*61, 62*) and its structure was the first to be obtained (*63*). Later, APX from soybean was isolated, purified (*60*) and finally crystallised in complex with ascorbate (*28*), providing the first identification of a physiological substrate binding site for a heme peroxidase.

#### *1.3.2.2. Heme intermediates in ascorbate peroxidase*

The reaction of APX with hydrogen peroxide was first studied by Patterson *et al.* (*64*) in pea-APX and the work led to the identification of a Compound I with a $\pi$-cation radical, typical of the heme peroxidases in general and also observed in HRP (*65*) (perhaps the most studied and representative of the field), MnP (*66*) and LiP (*67*). It was also observed that in absence of substrate, Compound I in APX quickly decayed to form another species, sometimes referred to as Compound I*. Further studies, by means of different spectroscopic techniques, showed that the same mechanism occurred in APXs from different sources (*56, 68-70*). Studies on Compound I* revealed that its spectroscopic features are almost identical to those of Compound II (*71*) and it

has a protein based radical, initially supposed to be delocalised on the aromatic ring of the side chain of a tryptophan (*72*). Nevertheless, reaction of both Compound I* and the actual Compound II with ascorbate occurs with a comparable rate and this shows that, unlike C*c*P, for APX the protein-stabilised radical is not a proper intermediate but it is only the effect of the decay of an unstable species. On a longer time scale, Compound I* decays irreversibly and covalent links between the heme and other residues appear (*73, 74*). Given the chemical identity of Compound I* and Compound II, no distinction is found between the two species anymore and they are both referred to as Compound II.

*1.3.2.3. The interaction with the substrate: APX as a general model*

Unlike C*c*P, the physiological substrate of APX is a small organic molecule, ascorbic acid (Figure [1. 5]). Studies from our group have demonstrated that the ascorbate binds near the heme γ-edge and a precise hydrogen bond network ensures its binding interactions. In particular, it has been noticed that the hydroxyl group of the ascorbate C2 lies within hydrogen bonding distance of the heme 7-propionate (*28*) (Figure [1. 4]-B). This specific interaction suggested a possible involvement of the heme propionates in the electron transfer mechanism during turnover and the original hypothesis has been later confirmed by theoretical studies (*75*). Moreover, in comparison with other heme peroxidases (like MnP for instance), these results helped generate a new general concept of substrate binding in heme peroxidases (see (*76*) for a recent review), that sees the heme γ-edge as the preferred binding site for physiological substrates in different cases and defines a precise role for the heme propionates in the reaction mechanism. These conclusions were also supported by

other studies on the activity of APX with other non-physiological substrates such as isoniazid (INH) or salicylhydroxamic acid (SHA). Structures of APX in complex with these two substrates were solved (*77, 78*) and the results showed binding of the substrates in the heme distal pocket and driven by hydrophobic interactions (Figure [1. 6]).

**Figure [1. 6]: View of the complex of APX with INH. The protein is shown as a grey surface while INH is presented as yellow sticks. Heme is in red.**

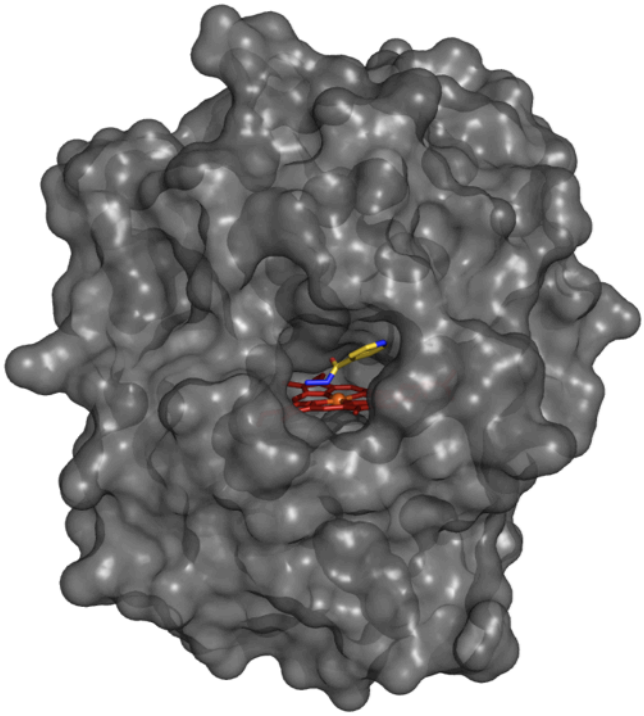

## 1.4. THE ISSUE OF THE OXY-FERRYL INTERMEDIATES

As previously indicated, the reaction mechanism of heme peroxidases follows three steps (Eq. 1, 2, 3) and proceeds through formation of two subsequent intermediates, Compound I and Compound II. In Compound I a radical and an oxy-ferryl species are found, whereas in Compound II only an oxy-ferryl species is present. Despite the large amount of data collected over the last 2-3 decades, which have provided important insights into the reaction mechanism of heme peroxidases, some aspects are yet to be clarified. Amongst all, the nature of the bond between the iron and the oxygen, in the oxy-ferryl species has a prominent role. Understanding this, in fact, would not only allow a more precise determination of the reaction mechanism of heme peroxidases, but it would also provide information, important to those heme enzymes such as CPO, cytochromes P450, heme catalases and NO synthase, whose reaction mechanism, likewise heme peroxidases, presents oxy-ferryl intermediates. In the next section an accurate comparison between the reaction cycle of heme peroxidase-like and other heme enzyme is presented, in order to identify those common elements that make heme peroxidases a model for the general case of heme enzymes.

### 1.4.1. INTERMEDIATES IN HEME ENZYMES

It is nowadays established that many heme enzymes may use a very similar reaction mechanism and most of the same intermediates occur in reactions of different heme-containing proteins. The cytochrome P450-like reaction cycle proceeds through reduction of the heme to ferrous state by means of a reducing partner (often NADPH or FADH), and hence formation of a ferrous-oxy species by reaction with

**Scheme [1.1]: Schematic representation of the general reaction mechanism of heme enzymes**

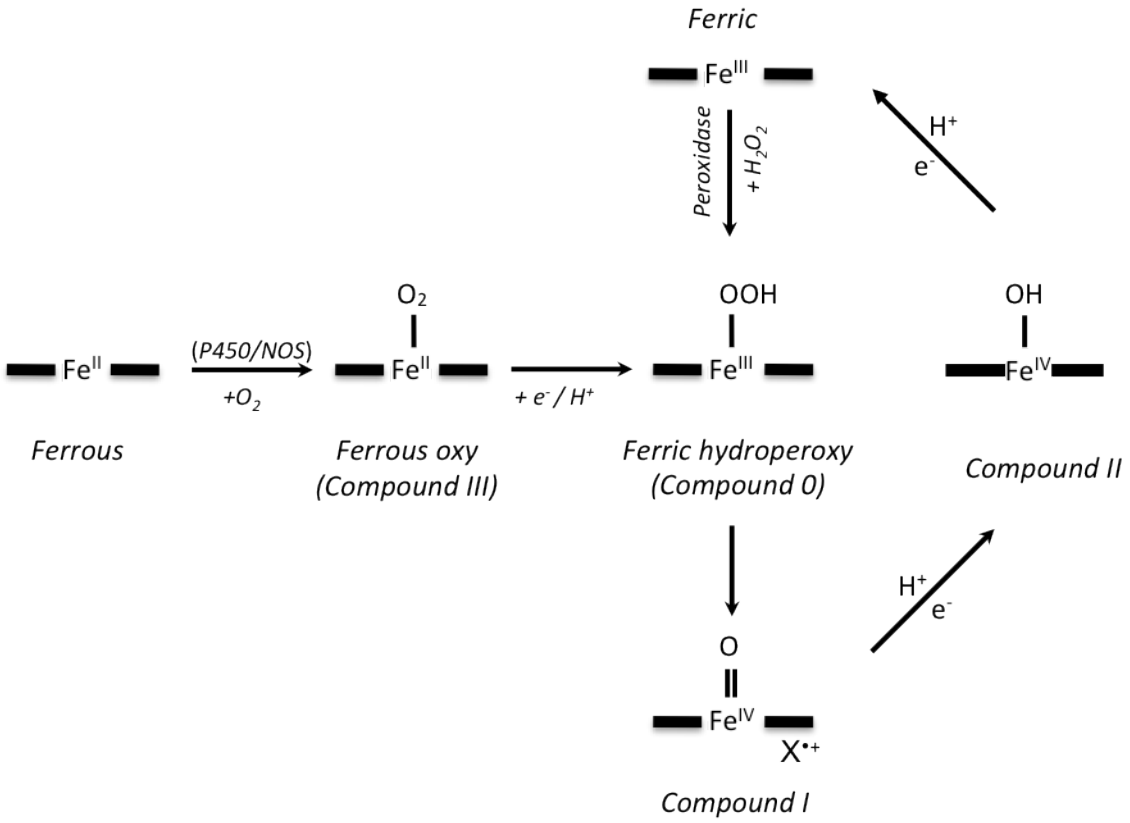


oxygen (Scheme [1.1]). It is interesting to note that the same ferrous-oxy species is also formed in hemoglobin and myoglobin and also in heme peroxidases by reaction of Compound II with an excess of hydrogen peroxide (*i.e.* non-physiological conditions). In the typical P450-like mechanism, the ferrous-oxy species is then reduced by addition of one electron equivalent, to form a heme-bound-hydroperoxy species that is equivalent to Compound 0. Just like for heme peroxidases, Compound 0 has never been isolated and beyond HRP, it has only been spectroscopically identified in mutants of myoglobin (*79*). The difficulty of trapping and isolating Compound 0 likely arises from the instability of this species that in turn quickly converts into Compound I. The latter is actually the oxidising species in many cases where the heme enzyme carries

out an oxidation and hence it is regarded as a very important intermediate. The structure of Compound I is believed to be the same for heme peroxidases as well as for all the other heme enzymes, although interesting studies have suggested that it might vary depending on the type of proximal ligand of the enzyme (*80*). On the basis of this theory, the electron-donation/withdrawn character of the different proximal ligands would cause the oxygen of the oxy-ferryl species to be either protonated or unprotonated.

Finally, it should be noted that Compound II is not observed in many heme enzymes such as the cytochromes P450, but it is a prerogative of heme peroxidases and only a few other heme enzymes.

### 1.4.2. THE UNCERTAINTY ABOUT THE NATURE OF THE OXY-FERRYL INTERMEDIATES

Over the last 30 years a number of studies have been produced, aimed at determining the nature of the bond between iron and oxygen in oxy-ferryl intermediates and in particular about Compound I, perhaps the real common key intermediates in many heme enzymes (see chapter 2 for a more detailed description). However, the picture that has been produced has proved confusing. Especially the crystallographic determinations of these intermediates has proved harder than expected, perhaps in consequence of both the elusive character of these intermediates and the extreme sensitivity to X-ray radiation. In some cases the results have even been contradictory. This all has generated uncertainty about the nature of the bond between the oxygen and the iron in the oxy-ferryl intermediates, confusion that calls for new and definitive experimental study which is able to provide conclusive answers about the issue of the nature of Compound I and Compound II.

Besides the experimental studies, theoretical approaches have provided interesting support to the experiments. They produced precise chemical descriptions of the models drawn on the basis of the various experimental results, defining crucial elements such as the nature of the bonds and the corresponding lengths, or the protonation states of the oxygen, depending on the nature of the Fe-O distances observed. Therefore, in order to have a general idea about this species, a brief description of the theoretical models produced is reported below.

*1.4.2.1. The theoretical models on heme coordination and oxy-ferryl species*

The first theoretical studies were aimed at the interpretation of spectroscopic features, observed with different techniques, in species obtained by reaction of enzymes like hemoglobin and myoglobin with both oxygen and hydrogen peroxide, or C*c*P and HRP with hydrogen peroxide (see (*81*) for a general summary up to the mid-1980s). Over the last 2-3 decades, theoretical studies have concentrated more specifically on the ferryl species in enzymes like the peroxidases and cytochromes P450 (see (*82*) for a recent review). Initially, no clear distinction was done between Compound I and Compound II and a unique model for the oxy-ferryl intermediates was developed, providing and iron-oxygen distance around 1.65 Å (*83*). In this model the oxygen was tightly bound to the iron and the bond between the two elements described as a covalent, double bond. No proton was allowed on the oxygen. When publication of X-ray structures appeared, experimental results showed a longer distance between oxygen and iron in ferryl intermediates, consistent with 1.80-1.85 Å. This was the case of C*c*P Compound I (*84, 85*) or Compound II of CPO (*86*), myoglobin (Mb) (*87*) and HRP (*84*). Models developed on these results showed that, if this was

the case, oxygen-iron bond was better defined as a single covalent bond and that the oxygen was likely to be protonated (*88, 89*). Longer distances were instead modelled for the case of ferric heme coordinating weak or strong field ligands. Coordination of a strong field ligand like the hydroxyl ion ($OH^-$) leads to formation of a complex with $Fe^{III}$-O distance set around 1.95 Å (*81*) while distances longer than 2.30 Å are expected for the binding of a weak field ligand like water (*81*).

**Table [1. 2]: Summary of the theoretical bond distances calculated for different heme species**

| Species | Fe-O distance (Å) | Reference |
|---|---|---|
| Compound I | 1.65 | (*83*) |
| Compound II | 1.80-1.85 | (*88, 89*) |
| Heme-hydroxyl complex | 1.95 | (*81*) |
| Heme-water complex | 2.30 | (*81*) |

## 1.5. THE ROLE OF THE HYDROGEN BONDS IN HEME PEROXIDASES

As previously discussed, the structures of the distal and proximal heme sides, in peroxidases, are conserved and so are the hydrogen bond networks that entail these residues. The role of these hydrogen bond networks (and the corresponding protonation state of the involved residues) was first postulated by Poulos and Kraut (*6*), who considered that these were the source of an inductive effect (usually referred to as the *push/pull* effect), able to modulate the activity of the enzymes. The various studies that followed, carried out over the last 30 years, have eventually confirmed this original model, extending its validity to the point that it is now an established and generally accepted model for heme peroxidases. Details of this model are reported below.

### 1.5.1. THE DISTAL HEME SIDE

The model indicates that the oxygen of the side chain of the distal asparagine (Figure [1. 3]) forms a hydrogen bond with the protonated $N_\delta$ of the distal histidine. On the contrary, the $N_\varepsilon$ of the distal histidine is supposed to be unprotonated and able to act as a base. Upon reaction with hydrogen peroxide, the $N_\varepsilon$ of the distal histidine is able to extract a proton from hydrogen peroxide, activating the molecule and leading to formation of Compound 0. The protonated histidine releases the proton to the hydrogen peroxide and causes the heterolytic cleavage of the peroxide bond. The hydrogen bond seems to play an important role in this acid/base mechanism: through the inductive effect caused by the hydrogen bond, the distal asparagine can modulate the properties of the distal histidine allowing this process (*pull* effec*t (6, 90)*). Two more hydrogen bonds on the distal heme side are instead considered important for the stabilisation of the oxy-ferryl intermediates. One is formed between the oxygen of the ferryl species and the $N_\varepsilon$ of the distal arginine (Figure [1. 3]) whilst the second is formed between the oxygen and the $N_\varepsilon$ of the distal tryptophan (Figure [1. 3]).

### 1.5.2. THE PROXIMAL HEME SIDE

As anticipated in section 1.2.1., the conserved proximal triad (histidine, aspartic acid and tryptophan, Figure [1. 3]) is also entailed by a hydrogen bond network. The structure is consistent with a model where the $N_\delta$ of the proximal histidine donates a hydrogen bond to one of the two oxygen atoms of the carboxylic group of the proximal aspartic acid, whilst the $N_\varepsilon$ of the proximal tryptophan donates a hydrogen bond to the

other oxygen of the aspartic acid side chain. The geometry of the network suggests that an inductive effect may be produced (*push* effect *(6, 90)*), which, provides an increased electron density on the imidazole ring of the proximal histidine, that helps to stabilise the oxy-ferryl species during turnover.

### 1.5.3. POSSIBLE NEW INSIGHTS INTO THE HYDROGEN BOND NETWORKS

The detailed description reported in section 1.5. indicates that hydrogen bond networks are crucial for the activity of the heme peroxidases and their role should be investigated in more depth, in order to gain new insights into the mechanism of these and other heme enzymes. Understanding them would not only fill the possible gaps in the present model, but it could also provide new information to report on key aspects, such as the mechanism by which protons are delivered to the oxy-ferryl species during turnover, that have not been explored yet. However, determination of the protonation states and hydrogen bond networks is not an easy task, especially using X-ray crystallography that presents important technical limitations in this sense (discussed further in the next section). On X-ray structures hydrogen bonds can only be extrapolated by measuring distances between atoms other than hydrogen and this can lead to incomplete or even incorrect results.

# 1.6. THE USE OF CRYSTALLOGRAPHIC TECHNIQUES

## 1.6.1. X-RAY CRYSTALLOGRAPHY IN HEME PEROXIDASES.

This thesis reports on crystallographic studies of two heme peroxidases, APX and C*c*P. In order to better understand the role that crystallography played in the field of heme peroxidases, as well as the potentials and the limitations this method presents in solving structures of heme enzymes, some of the crucial aspects are discussed in the following paragraphs.

Over the last few decades, X-ray crystallography has offered interesting insights into the understanding of heme peroxidases, providing structures able to help clarify many of the aspects of their reactivity. Thanks to the early availability of crystals (*24*), the first structure of ferric C*c*P was reported more than 30 years ago (*25, 91*), while the first attempt to determine the structure of Compound I in C*c*P dates back to 1987 (*92*). Over the last decade attention was mainly drawn to the determination of the nature of the heme-ferryl species and a more detailed description of the results published will be given later in Chapter 2. In general, with the increase of available structures, it became clear that X-ray radiation, used for data collection, was able to affect the nature of the heme species analysed. This effect was eventually described by Berglund *et al*. (*84*) through an analysis of photoreduction in the ferryl species of HRP, induced by X-ray radiation and monitored with single-crystal spectroscopy. This work clarified that heme proteins were extremely sensitive to photoreduction and showed that the consequences of X-ray exposure on iron coordination could be observable long before any other effect.

In order to better understand the effects caused by X-ray radiation on crystals of peroxidases, the fundamental issue of the crystallographic studies carried out with this thesis, a more detailed description is given in the following paragraphs.

### 1.6.2. THE INTERACTION OF X-RAYS WITH MATTER

X-rays are an electromagnetic radiation whose energy ranges between 0.1 and 100 keV. Just like all electromagnetic radiation, X-rays have a dual nature and can be described as particle-like entities (photons) and waves. X-rays interact with both the charged particles within atoms, protons and electrons. However, the magnitude of the effects caused by the interaction with protons is considerably smaller, if compared to the magnitude of the effects induced on electrons, and this is mainly due to the higher mass of the protons and the higher energy of nuclear phenomena. Therefore, it is possible to consider the interaction between X-rays and matter as the sole interaction between X-rays and electrons.

When a sample is irradiated with X-rays, the electrons in the atoms undergo a series of phenomena that can be all ascribed to two main effects, the absorbance and the scattering of X-rays. These are at the basis of widespread techniques such as X-ray spectroscopy, X-ray scattering and X-ray crystallography (*93*) and, for the purpose of this thesis, are discussed. The scattering is the effect that controls the X-ray diffraction phenomenon on which crystallography is based, whilst absorbance is at the basis of phenomena such as the photoreduction, relevant for the determination of the nature of Compound I and Compound II.

*1.6.2.1. The scattering of X-rays*

When X-rays hit a sample, the electric field of the electromagnetic wave interacts with the electrons of the atoms and causes them to transiently resonate. Since electrical charges in movement, the oscillating electrons themselves become a source of electromagnetic radiation, giving rise to the emission of new radiation, identical to the incoming ones (*i.e.* with the same energy and therefore wavelength), which are scattered out of the atoms in any direction. This process, referred to as elastic scattering (or Rayleigh scattering), is the principle on which techniques such as X-ray crystallography are based. However, elastic scattering is not the only effect to be observed. Another important phenomenon, known as Compton effect (or X-ray inelastic scattering) occurs and because of this, the scattered radiation usually consists of a distribution of wavelengths. Interpretation of the Compton effect requires consideration of the particle-like nature of the electromagnetic radiation. When X-ray photons hit the electrons, part of the carried energy can be transferred to the electrons and the incoming photons are re-emitted with only part of the original energy. Plank's equation relates the kinetic energy of a photon (E) to the frequency of the corresponding electromagnetic radiation ($\upsilon$):

$$E = h\upsilon \qquad \textbf{Eq. 5}$$

where *h* is Plank's constant. On this basis, the emitted photons, carrying less kinetic energy, correspond to waves scattered with longer wavelengths (lower frequency), thus justifying the energy distribution observed in the scattering. Moreover, the electrons, which have absorbed part of the energy of the photons, are excited and can be ejected from their orbitals. They are usually referred to as recoil electrons (*93, 94*).

*1.6.2.2. X-ray absorbance*

As mentioned above, the particle-like nature of the electromagnetic radiations justifies the fact that energy, carried by the X-ray photons, can be transferred to the electrons when the radiation hits a sample. The process by which the energy is transferred is defined as absorbance. Upon absorption of X-ray radiation various effects can take place and these are briefly discussed here.

The energy associated with X-rays (between 0.1 and 100 keV) is comparable to the ionisation energy of electrons in the atomic inner shells (usually electrons contained in the quantic levels *n*=1 or *n*=2). In other words, the energy of an X-ray radiation, when absorbed, is sufficient to excite the electrons up to the point that these are ejected from their orbitals. The released electrons, known as the *photoelectrons*, are relocated in external, empty atomic orbitals or, in the case of molecules, even in empty molecular orbitals (on the basis of the energy of the incoming radiation and the selection rules defined by quantum theory). The phenomenon by which the radiation causes the electrons to be ejected from their original states is named the *photoelectric effect.* Formation of photoelectrons is at the basis of a series of phenomena such as photoreduction and crystal damage, and will be discussed later. However the phenomenon is largely affected by the properties of both the absorbing atoms and the incoming waves. As determined by classical physics, the number of photoelectrons ($n_e$) produced by irradiation with X-rays, is, in first approximation, proportional to the absorbance cross section ($\sigma_e$) which, in turn, is proportional to the wavelength ($\lambda$) of the radiation and the number of electrons (Z) in the atom as follow:

$$n_e \propto \sigma_e \propto \lambda^3 Z^4 \qquad \textbf{Eq. 6}$$

This indicates that high energy X-rays induce a smaller photoelectric effect on the irradiated atoms and that the photoelectric effect is more pronounced in larger atoms. The case of carbon atoms is shown in Figure [1. 7] (*93*), where variation of photoelectric effect with the energy of incoming radiation is shown. Furthermore, in the same figure the photoelectric effect is compared to the variation of the elastic scattering (Rayleigh) and inelastic scattering (Compton). Data show that an increase in X-ray energy not only induces a decrease in the photoelectric effect, but it causes the Rayleigh scattering to be considerably diminished.

**Figure [1. 7]: Variation of photoelectric effect, Compton (inelastic) and Rayleigh (elastic) scattering with radiation wavelength (93).**

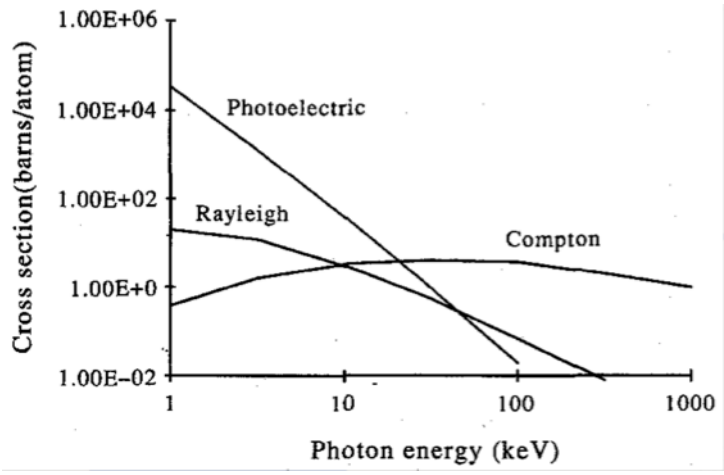


Besides the photoelectric effect, other phenomena are caused by absorbance of X-ray radiation. One of these is the Auger effect. This occurs when the vacancy left by a photoelectron in an inner shell is filled by another electron, which decays from a close, higher-energy orbital. The decaying electron releases part of its energy that may be absorbed by another electron. The latter, excited by the absorbed energy, can be ejected and form what is generally called an Auger electron (*93, 94*).

### 1.6.3. PHOTOREDUCTION AND RADIATION DAMAGE: THE EFFECTS OF X-RAYS ON PROTEINS

As previously indicated, the interaction of X-rays with matter induces various phenomena. The scattering is the basis of the X-ray crystallography used in this thesis, whilst the absorbance is the basis of techniques such as X-ray spectroscopy. However the absorbance is also the source of the photoelectric effect that has negative consequences on the stability of the structures of organic or biological samples, such as protein crystals. The release of photoelectrons causes effects that span from the reduction of chemical species (photoreduction) (*95, 96*) and changes in coordination geometry of ligands around a metal, to more evident damage, such as the breakage of covalent bonds, formation of radicals, and eventually a general degradation of the protein structure, generally referred to as radiation damage (see (*97*) for a recent review). More precisely, the photoelectrons produced can spread all over the protein causing immediate photoreduction of species such as metal ions. At the same time, they can cause the almost immediate breakage of covalent bonds like C-H, S-H, N-H and O-H with formation of various radicals (*98, 99*). Furthermore, owing to the considerable fraction of water contained in protein crystals, the electrons can also be solvated and form both hydrogen and hydroxyl radicals. All these effects occur in a few picoseconds and form what is collectively named the *primary effect* of radiation damage (*99*). Afterwards, in a second process, the primary species (*i.e.* the species formed because of the primary effect) “slowly” diffuse in the crystals and in a few milliseconds they induce further effects which eventually lead to breakage of C-C, C-N and C-O bonds and consequent degradation of the whole protein and of the crystal

lattice. These second set of phenomena are generally indicated as *secondary effect* of radiation damage (*99*).

A huge improvement to radiation damage in general was obtained by keeping the temperature of the crystals low during data collection. Reduction of temperature to that of liquid nitrogen (77 K) or just above, considerably slows any diffusion-based process (*95*) and, although photoreduction and primary effects (*96, 98*) still occur, formation of the corresponding primary species is constricted within very small areas of the protein, and secondary effects become negligible over a range of time corresponding to the collection of a dataset. It was first estimated that at 77 K, 50% of the decay of the crystal was achieved after a dose of about 20 MGy (*95*) but more recent studies showed that this threshold can be extended up to 30 MGy (*100*).

### 1.6.4. PHOTOREDUCTION IN METAL-CONTAINING PROTEINS

Although use of cryogenic conditions during data collection has significantly improved the quality and the feasibility of X-ray crystallography experiments, this has not provided a way to limit the photoreduction that, in some cases, even at small doses, affects the resolved structure. A prominent case in this sense is that of metal-containing enzymes. Upon X-ray irradiation, the photoelectron released can induce changes in the oxidation states of metal ions, modifying geometry of the coordinated ligands, long before any secondary effect is evident (*97, 101*). The consequences of these changes may of course be negligible or unimportant for the determination of an overall protein structure, however metal centres are often the core of the active sites and the geometry of their coordination is a determinant for the catalytic activity of the enzyme. It is therefore evident that photoreduction causes potential problems when

investigating the reaction mechanism of metal-containing proteins, and it may result eventually in an incorrect interpretation of the experimental data. This is certainly the case for the heme peroxidases. The geometrical configuration of the iron, with the heme and of the nearby amino acidic residues, is in general very sensitive to changes in the iron oxidation state. But even more sensitive is the structure of the oxy-ferryl heme intermediates, the subject of this thesis, where the high oxidation state of the iron (IV) and the presence of a very reactive oxygen atom, results in extremely electrophilic centres, that are able to act as a trap for the electrons released during X-ray exposure.

### 1.6.5. AVOIDING THE PHOTOREDUCTION EFFECT

When photoreduction is a major problem even at very low X-ray doses, this raises the issue of determining new ways to rule such an effect out. It has been proposed that some improvements can be achieved by using a temperature below that of liquid nitrogen (77 K) (*102*). However, the use of cryogenic fluids, such as liquid He, increases the costs of the experiments considerably, it is not always accessible and may not be effective. On the other hand, different (and perhaps more effective) methods could be used.

#### *1.6.5.1. The use of high energy X-ray radiation*

One possibility lies in the use of high energy X-ray beams and in this sense some data have recently been published (*103*). As shown in Figure [1. 7], the increase of energy reduces the photoelectric effect, although it simultaneously increases the Compton effect and decreases the amount of Rayleigh scattering, eventually causing a

loss of resolution. Besides these physical limitations, technical problems in the use of high energy X-ray radiation also arise from the low availability of short wavelength X-ray sources, which are accessible only on specific beamlines at synchrotron facilities, or at in-house instruments, with X-ray sources such as Mo anodes ($Mok\alpha = 0.7$ Å).

*1.6.5.2. The use of multicrystal methods*

Another possibility lies in use of a multi-crystal method. In this case the full dataset necessary for the determination of the structure, is not collected from a single crystal as usual. On the contrary, many crystals are exposed to X-rays, each for a very short time, thus receiving a dose of radiation that induces negligible effects of photoreduction. The whole dataset is an accumulation of all the small amounts of data collected from the different crystals. Interesting results have been obtained with this method over the last decade (*84, 104*), however the most important limitation in this case lies in the large number of crystals necessary, which are often not available.

*1.6.5.3. The use of neutron crystallography*

Besides the use of X-rays, another possibility for the crystallographic determination of the structure of proteins may arise with the use of neutron beams as the diffracting radiation. Neutron crystallography has steadily gained more importance over the last two decades, although the number of structures available on the protein data bank (PDB) web site obtained with this technique is still very small.

The key difference between neutron crystallography and X-ray crystallography lies of course in the physics of the neutron interactions with atoms. Neutrons are subatomic particles with about of the same mass as protons (≈ $10^{-27}$ Kg) but have no

charge. Moreover, their physics can be described by both wave-like and particle-like nature. The two natures are determined by De Broglie's equation,

$$\lambda = \frac{h}{mv} \qquad \textbf{Eq. 7}$$

Indicating that a particle of mass *m* and speed *v*, can also be described as a wave whose wavelength is $\lambda$ (*h* is Plank's constant). The absence of any charge causes neutrons to be scattered only by the nuclei and since no interaction with the electrons occurs during exposure, the sample does not undergo any chemical change, such as photoreduction or radiation damage. When the neutrons hit the nuclei, these, in a first approximation, behave as solid spheres that vibrate elastically and themselves become new sources of neutron radiation, identical to the incoming ones. The scattered neutrons can be regarded as waves and as such, in ordered samples like crystals, they will give rise to the phenomenon of diffraction. This is the basis for neutron crystallography.

The physics of the neutron scattering presents interesting consequences. In terms of wave mechanics, the wave function of the scattered neutrons is

$$-b\frac{e^{i\vec{k}\vec{r}}}{|r|} \qquad \textbf{Eq. 8}$$

where $\vec{k}$ is the vector of the direction of the scattered neutrons, $\vec{r}$ is the vector difference between the incoming beam and the scattered one, and most importantly, $b$ is the scattering length. The value that $b$ assumes is specific for each atom, as it depends only on the energy of the excited states the atoms can reach upon interaction with the incoming neutrons, and it does not depend on the size of the atom (see Table [1. 3] for a list of *b* values relative to some atoms). A particular case of scattering

occurs when, upon collision, the energy transfer from the neutrons to the nuclei is enough to induce formation of an excited species. In this case the excited nucleus vibrates, scattering neutrons with an anomalous character and the scattering length *b* assumes unexpected values, as observed for hydrogen atoms (Table [1. 3]). However, the anomalous scattering is usually observed only for hydrogen atoms in crystallographic and scattering experiments and the reason lies in the energy of the beams used for such experiments. In fact, neutrons produced for scattering and diffraction are *thermal* or *cold* (*i.e.* their molar energy corresponds to *RT* at 293 K or below), while the energy of the exited nuclear states for atoms heavier than hydrogen is higher. Therefore, the collisions of the neutrons do not allow the nuclei to reach the exited state and consequently anomalous scattering is not observed.

**Table [1. 3]: The values of b for some biologically interesting atoms.**

| Element | Atomic number | Scattering length *b* (fm) | Coherent cross section (barn) | Incoherent cross section (barn) |
|---|---|---|---|---|
| H | 1 | -3.74 | 1.758 | 80.27 |
| D | 1 | 6.67 | 5.59 | 2.05 |
| C | 12 | 6.64 | 5.51 | 0.001 |
| N | 13 | 9.36 | 11.01 | 0.5 |
| O | 16 | 5.80 | 4.23 | 0.0008 |
| Fe | 27 | 9.45 | 11.22 | 0.4 |

*1.6.5.4. Advantages and limitations of using neutron crystallography*

As mentioned above, neutrons interact directly with the nuclei and, therefore, no effects are produced on the electronic shells. The first important consequence is of course that no photoreduction occurs during exposure. Secondly the direct interaction with the nuclei allows for the determination of the position of light elements such as

hydrogen and deuterium atoms, which are almost invisible to X-ray diffraction, unless at very high resolution, owing to the insufficient intensity of scattering (*105*). Moreover, the different scattering length of hydrogen and deuterium atoms (Table [1. 3]) allows the two elements to be distinguished (*105*).

This would be the case, for instance, of protein crystals grown or soaked in deuterated mother liquor (deuterated crystals) (*106, 107*), where deuterium atoms would only be found in place of exchangeable hydrogen atoms. In this sense, neutron crystallography can be regarded as a precise tool that is able to unveil specific structural aspects, impossible to observe otherwise, and eventually may allow for a better and more accurate understanding of the enzymatic reaction mechanism.

Despite the many advantages, neutron crystallography is not yet widely used mainly because of the hard to overcome technical limitations. First of all, neutron beams are produced by means of nuclear reactors or from spallation sources and, amongst all the facilities worldwide, only three are dedicated to macromolecular crystallography (*108*), in most part the sources are dedicated to studying the physics of the particles. The limited availability of facilities is even more complicated by the low intensity of the neutron beams, which results in an extremely long data collection and the need for crystals as large as possible. Furthermore, the use of deuterated crystals, easy to achieve and affordable, results in incomplete nuclear density maps as the unexchanged hydrogen atoms, with their negative scattering lengths, cancel out the scattering of nearby heavier atoms, requiring thus an X-ray/neutron joint study to solve the complete structure of the protein. On the other hand, the use of fully deuterated crystals (*i.e.* perdeuterated crystals), even though effective in overcoming the limitations of the negative scattering of hydrogen atoms, can be very expensive

and often leads to crystal forms of the proteins which are not suitable for neutron crystallography.

## 1.7. THESIS AIM: INSIGHTS INTO THE REACTION MECHANISM OF HEME PEROXODASES.

The main objective of the project is to determine for the first time the exact structure of Compound I and Compound II in both C*c*P and APX, and by comparison, try to generalise the results, extending them to the whole field of heme, oxygen activator enzymes. This objective has been pursued by means of crystallographic techniques, particularly suitable for the determination of the sought structural details. This has entailed:

a. use of multicrystal approach for the determination of the X-ray crystal structures of resting state, Compound I and Compound II of C*c*P
b. use of multicrystal approach combined with high-energy X-ray radiation for the determination of the X-ray crystal structures of resting state, Compound I, Compound II and Compound III of APX
c. investigate the feasibility of neutron crystallography for the determination of unaltered structures and hydrogen bond networks of heme-containing enzymes by solving the structure of C*c*P in its resting state.

The results are presented on a chemical species-basis, in order to allow, where possible, a direct comparison of the structures of the same intermediate in the two different proteins. This should provide a view on the results not only limited to the characteristic of the determined species, but it should allow extrapolation to the general case.

**Reference**


1. Crichton, R. (2001) *Inorganic Biochemistry of Iron Metabolism: From Molecular Mechanisms to Clinical Consequences*, Second edition ed., Wiley.
2. Montellano, P. R. O. d. (2005) *Cytochrome P450 Structure, Mechanism, and Biochemistry*, Third edition ed., Springer US.
3. Welinder, K. G., Mauro, J. M., and Norskov-Lauritsen, L. (1992) Structure of plant and fungal peroxidases, *Biochem Soc Trans 20*, 337-340.
4. Zamocky, M., Jakopitsch, C., Furtmüller, P. G., Dunand, C., and Obinger, C. (2008) The peroxidase–cyclooxygenase superfamily: Reconstructed evolution of critical enzymes of the innate immune system, *Proteins: Structure, Function, and Bioinformatics 72*, 589-605.
5. Dunford, B. (2010) *Peroxidases and Catalases: Biochemistry, Biophysics, Biotechnology and Physiology*, Second edition ed., Wiley.
6. Poulos, T. L., and Kraut, J. (1980) The stereochemistry of peroxidase catalysis, *J Biol Chem 255*, 8199-8205.
7. Browett, W. R., Gasyna, Z., and Stillman, M. J. (1988) Temperature dependence and electronic transition energies in the magnetic circular dichroism spectrum of horseradish peroxidase compound I, *Journal of the American Chemical Society 110*, 3633-3640.
8. Hashimoto, S., Tatsuno, Y., and Kitagawa, T. (1986) Resonance Raman evidence for oxygen exchange between the FeIV = O heme and bulk water during enzymic catalysis of horseradish peroxidase and its relation with the heme-linked ionization, *Proc Natl Acad Sci U S A 83*, 2417-2421.
9. Hashimoto, S., Teraoka, J., Inubushi, T., Yonetani, T., and Kitagawa, T. (1986) Resonance Raman study on cytochrome c peroxidase and its intermediate. Presence of the Fe(IV) = O bond in compound ES and heme-linked ionization, *J Biol Chem 261*, 11110-11118.
10. Iizuka, T., Kotani, M., and Yonetani, T. (1968) A thermal equilibrium between high- and low-spin states in ferric cytochrome c peroxidase and some discussion on the enzyme-substrate complex, *Biochim Biophys Acta 167*, 257-267.
11. Lang, G., Spartalian, K., and Yonetani, T. (1976) Mossbauer spectroscopic study of compound ES of cytochrome c peroxidase, *Biochim Biophys Acta 451*, 250-258.
12. Moss, T. H., Ehrenberg, A., and Bearden, A. J. (1969) Moessbauer spectroscopic evidence for the electronic configuration of iron in horseradish peroxidase and its peroxide derivatives, *Biochemistry 8*, 4159-4162.
13. Myers, D., and Palmer, G. (1985) Magnetic circular dichroism studies on the heme and tryptophan components of cytochrome c peroxidase, *J Biol Chem 260*, 3887-3890.
14. Oertling, W. A., and Babcock, G. T. (1985) Resonance Raman scattering from horseradish peroxidase compound I, *Journal of the American Chemical Society 107*, 6406-6407.
15. Roberts, J. E., Hoffman, B. M., Rutter, R., and Hager, L. P. (1981) Electron-nuclear double resonance of horseradish peroxidase compound I. Detection of the porphyrin pi-cation radical, *J Biol Chem 256*, 2118-2121.

16. Sitter, A. J., Reczek, C. M., and Terner, J. (1985) Heme-linked ionization of horseradish peroxidase compound II monitored by the resonance Raman Fe(IV)=O stretching vibration, *J Biol Chem 260*, 7515-7522.
17. Dunford, H. B., and Hewson, W. D. (1977) Effect of mixed solvents on the formation of horseradish peroxidase compound I. The importance of diffusion-controlled reactions, *Biochemistry 16*, 2949-2957.
18. Baek, H. K., and Van Wart, H. E. (1989) Elementary steps in the formation of horseradish peroxidase compound I: direct observation of compound 0, a new intermediate with a hyperporphyrin spectrum, *Biochemistry 28*, 5714-5719.
19. Hiner, A. N. P., Raven, E. L., Thorneley, R. N. F., GarcIa-Cánovas, F., and RodrIguez-López, J. N. (2002) Mechanisms of compound I formation in heme peroxidases, *Journal of Inorganic Biochemistry 91*, 27-34.
20. Noble, R. W., and Gibson, Q. H. (1970) The reaction of ferrous horseradish peroxidase with hydrogen peroxide, *J Biol Chem 245*, 2409-2413.
21. Wittenberg, J. B., Noble, R. W., Wittenberg, B. A., Antonini, E., Brunori, M., and Wyman, J. (1967) Studies on the equilibria and kinetics of the reactions of peroxidase with ligands. II. The reaction of ferroperoxidase with oxygen, *J Biol Chem 242*, 626-634.
22. Altschul, A. M., Abrams, R., and Hogness, T. R. (1940) CYTOCHROME C PEROXIDASE, *Journal of Biological Chemistry 136*, 777-794.
23. Yonetani, T., and Ohnishi, T. (1966) Cytochrome c Peroxidase, a Mitochondrial Enzyme of Yeast, *Journal of Biological Chemistry 241*, 2983-2984.
24. Yonetani, T. (1967) Studies on cytochrome c peroxidase. X. Crystalline apo-and reconstituted holoenzymes, *J Biol Chem 242*, 5008-5013.
25. Poulos, T. L., Freer, S. T., Alden, R. A., Xuong, N. H., Edwards, S. L., Hamlin, R. C., and Kraut, J. (1978) Crystallographic determination of the heme orientation and location of the cyanide binding site in yeast cytochrome c peroxidase, *J Biol Chem 253*, 3730-3735.
26. Erman, J. E., Vitello, L. B., Mauro, J. M., and Kraut, J. (1989) Detection of an oxyferryl porphyrin pi-cation-radical intermediate in the reaction between hydrogen peroxide and a mutant yeast cytochrome c peroxidase. Evidence for tryptophan-191 involvement in the radical site of compound I, *Biochemistry 28*, 7992-7995.
27. Sivaraja, M., Goodin, D. B., Smith, M., and Hoffman, B. M. (1989) Identification by ENDOR of Trp191 as the free-radical site in cytochrome c peroxidase compound ES, *Science 245*, 738-740.
28. Sharp, K. H., Mewies, M., Moody, P. C., and Raven, E. L. (2003) Crystal structure of the ascorbate peroxidase-ascorbate complex, *Nat Struct Biol 10*, 303-307.
29. Bonagura, C. A., Sundaramoorthy, M., Bhaskar, B., and Poulos, T. L. (1999) The Effects of an Engineered Cation Site on the Structure, Activity, and EPR Properties of Cytochrome c Peroxidase,Ä†, *Biochemistry 38*, 5538-5545.
30. Bonagura, C. A., Sundaramoorthy, M., Pappa, H. S., Patterson, W. R., and Poulos, T. L. (1996) An Engineered Cation Site in Cytochrome c Peroxidase Alters the Reactivity of the Redox Active Tryptophan,Ä†, *Biochemistry 35*, 6107-6115.
31. Jensen, G. M., Bunte, S. W., Warshel, A., and Goodin, D. B. (1998) Energetics of Cation Radical Formation at the Proximal Active Site Tryptophan of Cytochrome

c Peroxidase and Ascorbate Peroxidase, *The Journal of Physical Chemistry B 102*, 8221-8228.

32. Huyett, J. E., Doan, P. E., Gurbiel, R., Houseman, A. L. P., Sivaraja, M., Goodin, D. B., and Hoffman, B. M. (1995) Compound ES of Cytochrome c Peroxidase Contains a Trp .pi.-Cation Radical: Characterization by Continuous Wave and Pulsed Q-Band External Nuclear Double Resonance Spectroscopy, *Journal of the American Chemical Society 117*, 9033-9041.
33. Stemp, E. D., and Hoffman, B. M. (1993) Cytochrome c peroxidase binds two molecules of cytochrome c: evidence for a low-affinity, electron-transfer-active site on cytochrome c peroxidase, *Biochemistry 32*, 10848-10865.
34. Mauk, M. R., Ferrer, J. C., and Mauk, A. G. (1994) Proton linkage in formation of the cytochrome c-cytochrome c peroxidase complex: electrostatic properties of the high- and low-affinity cytochrome binding sites on the peroxidase, *Biochemistry 33*, 12609-12614.
35. Pelletier, H., and Kraut, J. (1992) Crystal structure of a complex between electron transfer partners, cytochrome c peroxidase and cytochrome c, *Science 258*, 1748-1755.
36. Zhou, J. S., Tran, S. T., McLendon, G., and Hoffman, B. M. (1997) Photoinduced electron transfer between cytochrome c peroxidase (D37K) and Zn-substituted cytochrome c: Probing the two-domain binding and reactivity of the peroxidase, *Journal of the American Chemical Society 119*, 269-277.
37. Stemp, E. D. A., and Hoffman, B. M. (1993) Cytochrome c peroxidase binds two molecules of cytochrome c: Evidence for a low-affinity, electron-transfer-active site on cytochrome c peroxidase, *Biochemistry 32*, 10848-10865.
38. Rosenfeld, R. J., Hays, A. M., Musah, R. A., and Goodin, D. B. (2002) Excision of a proposed electron transfer pathway in cytochrome c peroxidase and its replacement by a ligand-binding channel, *Protein Sci 11*, 1251-1259.
39. Hays Putnam, A. M., Lee, Y. T., and Goodin, D. B. (2009) Replacement of an electron transfer pathway in cytochrome c peroxidase with a surrogate peptide, *Biochemistry 48*, 1-3.
40. Jablonski, P. P., and Anderson, J. W. (1982) Light-Dependent Reduction of Hydrogen Peroxide by Ruptured Pea Chloroplasts, *Plant Physiol. 69*, 1407-1413.
41. Gillham, D. J., and Dodge, A. D. (1986) Hydrogen-peroxide-scavenging systems within pea chloroplasts, *Planta 167*, 246-251.
42. Nakano, Y., and Asada, K. (1987) Purification of Ascorbate Peroxidase in Spinach Chloroplasts; Its Inactivation in Ascorbate-Depleted Medium and Reactivation by Monodehydroascorbate Radical, *Plant and Cell Physiology 28*, 131-140.
43. Chen, G.-X., and Asada, K. (1989) Ascorbate Peroxidase in Tea Leaves: Occurrence of Two Isozymes and the Differences in Their Enzymatic and Molecular Properties, *Plant and Cell Physiology 30*, 987-998.
44. Tanaka, K., Takeuchi, E., Kubo, A., Sakaki, T., Haraguchi, K., and Kawamura, Y. (1991) Two immunologically different isozymes of ascorbate peroxidase from spinach leaves, *Arch Biochem Biophys 286*, 371-375.
45. Chen, G.-X., Sano, S., and Asada, K. (1992) The Amino Acid Sequence of Ascorbate Peroxidase from Tea Has a High Degree of Homology to That of Cytochrome c Peroxidase from Yeast, *Plant and Cell Physiology 33*, 109-116.

46. Miyake, C., Cao, W.-H., and Asada, K. (1993) Purification and Molecular Properties of the Thylakoid-Bound Ascorbate Peroxidase in Spinach Chloroplasts, *Plant and Cell Physiology 34*, 881-889.
47. Amako, K., Chen, G.-X., and Asada, K. (1994) Separate Assays Specific for Ascorbate Peroxidase and Guaiacol Peroxidase and for the Chloroplastic and Cytosolic Isozymes of Ascorbate Peroxidase in Plants, *Plant and Cell Physiology 35*, 497-504.
48. Meneguzzo, S., Sgherri, C. L. M., Navari-Izzo, F., and Izzo, R. (1998) Stromal and thylakoid-bound ascorbate peroxidases in NaCl-treated wheat, *Physiologia Plantarum 104*, 735-740.
49. Yoshimura, K., Ishikawa, T., Nakamura, Y., Tamoi, M., Takeda, T., Tada, T., Nishimura, K., and Shigeoka, S. (1998) Comparative study on recombinant chloroplastic and cytosolic ascorbate peroxidase isozymes of spinach, *Arch Biochem Biophys 353*, 55-63.
50. Heering, H. A., Jansen, M. A. K., Thorneley, R. N. F., and Smulevich, G. (2001) Cationic Ascorbate Peroxidase Isoenzyme II from Tea:‚Äâ Structural Insights into the Heme Pocket of a Unique Hybrid Peroxidase‚Äâ†, *Biochemistry 40*, 10360-10370.
51. Dalton, D. A., Hanus, F. J., Russell, S. A., and Evans, H. J. (1987) Purification, Properties, and Distribution of Ascorbate Peroxidase in Legume Root Nodules, *Plant Physiol. 83*, 789-794.
52. Elia, M. R., Borraccino, G., and Dipierro, S. (1992) Soluble ascorbate peroxidase from potato tubers, *Plant Science 85*, 17-21.
53. Koshiba, T. (1993) Cytosolic Ascorbate Peroxidase in Seedlings and Leaves of Maize (Zea mays), *Plant and Cell Physiology 34*, 713-721.
54. Ishikawa, T., Takeda, T., and Shigeoka, S. (1996) Purification and characterization of cytosolic ascorbate peroxidase from komatsuna (Brassica rapa), *Plant Science 120*, 11-18.
55. De Gara, L., de Pinto, M. C., and Arrigoni, O. (1997) Ascorbate synthesis and ascorbate peroxidase activity during the early stage of wheat germination, *Physiologia Plantarum 100*, 894-900.
56. Kvaratskhelia, M., Winkel, C., and Thorneley, R. (1997) Purification and Characterization of a Novel Class III Peroxidase Isoenzyme from Tea Leaves, *Plant Physiol. 114*, 1237-1245.
57. Ohya, T., Morimura, Y., Saji, H., Mihara, T., and Ikawa, T. (1997) Purification and characterization of ascorbate peroxidase in roots of Japanese radish, *Plant Science 125*, 137-145.
58. Battistuzzi, G., D'Onofrio, M., Loschi, L., and Sola, M. (2001) Isolation and Characterization of Two Peroxidases from Cucumis sativus, *Archives of Biochemistry and Biophysics 388*, 100-112.
59. Preger, V., Pesaresi, A., Pupillo, P., and Trost, P. (2001) Ascorbate-independent electron transfer between cytochrome<i>b</i><sub>561</sub> and a 27 kDa ascorbate peroxidase of bean hypocotyls, *Protoplasma 217*, 137-145.
60. Dalton, D. A., Diaz del Castillo, L., Kahn, M. L., Joyner, S. L., and Chatfield, J. M. (1996) Heterologous expression and characterization of soybean cytosolic ascorbate peroxidase, *Arch Biochem Biophys 328*, 1-8.

61. Mittler, R., and Zilinskas, B. A. (1991) Purification and Characterization of Pea Cytosolic Ascorbate Peroxidase, *Plant Physiol. 97*, 962-968.
62. Mittler, R., and Zilinskas, B. A. (1991) Molecular cloning and nucleotide sequence analysis of a cDNA encoding pea cytosolic ascorbate peroxidase, *FEBS Lett 289*, 257-259.
63. Patterson, W. R., and Poulos, T. L. (1995) Crystal structure of recombinant pea cytosolic ascorbate peroxidase, *Biochemistry 34*, 4331-4341.
64. Patterson, W. R., Poulos, T. L., and Goodin, D. B. (1995) Identification of a porphyrin pi cation radical in ascorbate peroxidase compound I, *Biochemistry 34*, 4342-4345.
65. Theorell, H., and Ehrenberg, A. (1952) Magnetic properties of some peroxide compounds of myoglobin, peroxidase and catalase, *Archives of Biochemistry and Biophysics 41*, 442-461.
66. Wariishi, H., Akileswaran, L., and Gold, M. H. (1988) Manganese peroxidase from the basidiomycete Phanerochaete chrysosporium: spectral characterization of the oxidized states and the catalytic cycle, *Biochemistry 27*, 5365-5370.
67. Khindaria, A., and Aust, S. D. (1996) EPR Detection and Characterization of Lignin Peroxidase Porphyrin pi-Cation Radical†, *Biochemistry 35*, 13107-13111.
68. Marquez, L. A., Quitoriano, M., Zilinskas, B. A., and Dunford, H. B. (1996) Kinetic and spectral properties of pea cytosolic ascorbate peroxidase, *FEBS Lett 389*, 153-156.
69. Lad, L., Mewies, M., Basran, J., Scrutton, N. S., and Raven, E. L. (2002) Role of histidine 42 in ascorbate peroxidase. Kinetic analysis of the H42A and H42E variants, *Eur J Biochem 269*, 3182-3192.
70. Lad, L., Mewies, M., and Raven, E. L. (2002) Substrate binding and catalytic mechanism in ascorbate peroxidase: evidence for two ascorbate binding sites, *Biochemistry 41*, 13774-13781.
71. Alexander N. P. HINER, J. N. R.-L., Marino B. ARNAO, Emma LLOYD RAVEN,, and ACOSTA, F. G.-C. a. M. (2000) Kinetic study of the inactivation of ascorbate peroxidase by hydrogen peroxide, *Biochem. J. 348,* , 321-328.
72. Hiner, A. N., Martinez, J. I., Arnao, M. B., Acosta, M., Turner, D. D., Lloyd Raven, E., and Rodriguez-Lopez, J. N. (2001) Detection of a tryptophan radical in the reaction of ascorbate peroxidase with hydrogen peroxide, *Eur J Biochem 268*, 3091-3098.
73. Zoi Pipirou, A. R. B., Clive M. Metcalfe, Sharad C. Mistry, Sandip K. Badyal,, and Bernard J. Rawlings, a. E. L. R. (2007) Autocatalytic Formation of a Covalent Link between Tryptophan 41 and the Heme in ascorbate Peroxidase, *Biochemistry 46*, 2174-2180.
74. Zoi Pipirou, A. R. B., Dimitri A. Svistunenko, Igor Efimov, Jaswir Basran, Sharad C. Mistry, Christopher E. Cooper, and Emma Lloyd Raven. (2007) The Reactivity of Heme in Biological Systems: Autocatalytic Formation of Both Tyrosine-Heme and Tryptophan-Heme Covalent Links in a Single Protein Architecture, *Biochemistry 46*, 13269-13278.
75. Guallar, V. (2008) Heme electron transfer in peroxidases: the propionate e-pathway, *J Phys Chem B 112*, 13460-13464.

76. Gumiero, A., Murphy, E. J., Metcalfe, C. L., Moody, P. C., and Raven, E. L. (2010) An analysis of substrate binding interactions in the heme peroxidase enzymes: A structural perspective, *Arch Biochem Biophys*.
77. Metcalfe, C., Macdonald, I. K., Murphy, E. J., Brown, K. A., Raven, E. L., and Moody, P. C. (2008) The tuberculosis prodrug isoniazid bound to activating peroxidases, *J Biol Chem 283*, 6193-6200.
78. Sharp, K. H., Moody, P. C., Brown, K. A., and Raven, E. L. (2004) Crystal structure of the ascorbate peroxidase-salicylhydroxamic acid complex, *Biochemistry 43*, 8644-8651.
79. Brittain, T., Baker, A. R., Butler, C. S., Little, R. H., Lowe, D. J., Greenwood, C., and Watmough, N. J. (1997) Reaction of variant sperm-whale myoglobins with hydrogen peroxide: the effects of mutating a histidine residue in the haem distal pocket, *Biochem. J. 326*, 109-115.
80. Behan, R. K., and Green, M. T. (2006) On the status of ferryl protonation, *Journal of Inorganic Biochemistry 100*, 448-459.
81. (1982) *Iron Porphyrins*, Vol. 1, ADDISON-WESLEY Publishing company.
82. Guallar, V., and Wallrapp, F. H. (2010) QM/MM methods: Looking inside heme proteins biochemisty, *Biophysical Chemistry 149*, 1-11.
83. Ghosh, A., Almlof, J., and Que, L. (1994) Density Functional Theoretical Study of Oxo(porphyrinato)iron(IV) Complexes, Models of Peroxidase Compounds I and II, *The Journal of Physical Chemistry 98*, 5576-5579.
84. Berglund, G. I., Carlsson, G. H., Smith, A. T., Szoke, H., Henriksen, A., and Hajdu, J. (2002) The catalytic pathway of horseradish peroxidase at high resolution, *Nature 417*, 463-468.
85. Fulop, V., Phizackerley, R. P., Soltis, S. M., Clifton, I. J., Wakatsuki, S., Erman, J., Hajdu, J., and Edwards, S. L. (1994) Laue diffraction study on the structure of cytochrome c peroxidase compound I, *Structure 2*, 201-208.
86. Green, M. T., Dawson, J. H., and Gray, H. B. (2004) Oxoiron(IV) in chloroperoxidase compound II is basic: implications for P450 chemistry, *Science 304*, 1653-1656.
87. Hersleth, H. P., Dalhus, B., Gorbitz, C. H., and Andersson, K. K. (2002) An iron hydroxide moiety in the 1.35 A resolution structure of hydrogen peroxide derived myoglobin compound II at pH 5.2, *J Biol Inorg Chem 7*, 299-304.
88. Conradie, J., Swarts, J. C., and Ghosh, A. (2004) Models of High-Valent Heme Protein Intermediates: A Quantum Chemical Study of Iron(IV) Porphyrins with Two Univalent Axial œÄ-Bonding Ligands, *The Journal of Physical Chemistry B 108*, 452-456.
89. Rovira, C., and Fita, I. (2003) The Proximal Hydrogen-Bonded Residue Controls the Stability of the Compound II Intermediate of Peroxidases and Catalases, *The Journal of Physical Chemistry B 107*, 5300-5305.
90. Nonaka, D., Wariishi, H., Welinder, K. G., and Fujii, H. (2010) Paramagnetic 13C and 15N NMR analyses of the push and pull effects in cytochrome c peroxidase and Coprinus cinereus peroxidase variants: functional roles of highly conserved amino acids around heme, *Biochemistry 49*, 49-57.
91. Poulos, T. L., Freer, S. T., Alden, R. A., Edwards, S. L., Skogland, U., Takio, K., Eriksson, B., Xuong, N., Yonetani, T., and Kraut, J. (1980) The crystal structure of cytochrome c peroxidase, *J Biol Chem 255*, 575-580.

92. Edwards, S. L., Nguyen, H. X., Hamlin, R. C., and Kraut, J. (1987) Crystal structure of cytochrome c peroxidase compound I, *Biochemistry 26*, 1503-1511.
93. Pavlinsky, G. V. (2008) *Fundamentals of X-Ray Physics*, Cambridge International Science Publishing, Cambridge, , GBR.
94. Dyson, N. A. (1973) *X-rays in atomic and nuclear physics*, Longman Group Limited, London.
95. Henderson, R. (1990) Cryo-Protection of Protein Crystals against Radiation Damage in Electron and X-Ray Diffraction, *Proceedings of the Royal Society of London. Series B: Biological Sciences 241*, 6-8.
96. Nave, C. (1995) Radiation damage in protein crystallography, *Radiation Physics and Chemistry 45*, 483-490.
97. Carugo, O., and Carugo, K. D. (2005) When X-rays modify the protein structure: radiation damage at work, *Trends in Biochemical Sciences 30*, 213-219.
98. Henderson, R. (1995) The potential and limitations of neutrons, electrons and X-rays for atomic resolution microscopy of unstained biological molecules, *Quarterly Reviews of Biophysics 28*, 171-193.
99. Ravelli, R. B. G., and McSweeney, S. M. (2000) The [`]fingerprint' that X-rays can leave on structures, *Structure 8*, 315-328.
100. Owen, R. L., RudiV±o-PiV±era, E., and Garman, E. F. (2006) Experimental determination of the radiation dose limit for cryocooled protein crystals, *Proceedings of the National Academy of Sciences of the United States of America 103*, 4912-4917.
101. Yano, J., Kern, J., Irrgang, K.-D., Latimer, M. J., Bergmann, U., Glatzel, P., Pushkar, Y., Biesiadka, J., Loll, B., Sauer, K., Messinger, J., Zouni, A., and Yachandra, V. K. (2005) X-ray damage to the Mn4Ca complex in single crystals of photosystem II: A case study for metalloprotein crystallography, *Proceedings of the National Academy of Sciences of the United States of America 102*, 12047-12052.
102. Corbett, M. C., Latimer, M. J., Poulos, T. L., Sevrioukova, I. F., Hodgson, K. O., and Hedman, B. (2007) Photoreduction of the active site of the metalloprotein putidaredoxin by synchrotron radiation, *Acta Crystallographica Section D 63*, 951-960.
103. Unno, M., Chen, H., Kusama, S., Shaik, S., and Ikeda-Saito, M. (2007) Structural characterization of the fleeting ferric peroxo species in myoglobin: experiment and theory, *Journal of the American Chemical Society 129*, 13394-13395.
104. Meharenna, Y. T., Doukov, T., Li, H. Y., Soltis, S. M., and Poulos, T. L. (2010) Crystallographic and Single-Crystal Spectral Analysis of the Peroxidase Ferryl Intermediate, *Biochemistry 49*, 2984-2986.
105. Niimura, N., and Bau, R. (2008) Neutron protein crystallography: beyond the folding structure of biological macromolecules, *Acta Crystallogr A 64*, 12-22.
106. Petit-Haertlein, I., Blakeley, M. P., Howard, E., Hazemann, I., Mitschler, A., Podjarny, A., and Haertlein, M. (2010) Incorporation of methyl-protonated valine and leucine residues into deuterated ocean pout type III antifreeze protein: expression, crystallization and preliminary neutron diffraction studies, *Acta Crystallographica Section F 66*, 665-669.
107. Budayova-Spano, M., Bonnete, F., Ferte, N., El Hajji, M., Meilleur, F., Blakeley, M. P., and Castro, B. (2006) A preliminary neutron diffraction study of

rasburicase, a recombinant urate oxidase enzyme, complexed with 8-azaxanthin, *Acta Crystallogr Sect F Struct Biol Cryst Commun 62*, 306-309.

108. Blakeley, M. P., Langan, P., Niimura, N., and Podjarny, A. (2008) Neutron crystallography: opportunities, challenges, and limitations, *Curr Opin Struct Biol 18*, 593-600.

Chapter 2

# OXY-INTERMEDIATES OF CYTOCHROME *C* PEROXIDASE AND ASCORBATE PEROXIDASE

## 2.1. INTRODUCTION

This chapter presents the crystallographic determination of Compound I and Compound II for both C*c*P and APX. For clarity, the chapter is divided into two parts, the first relative to Compound I, and the second relative to Compound II.

Together with these intermediates, two more (non-physiological) species are presented. The first is Compound III of APX, obtained directly by reaction of Compound II of APX with excess of hydrogen peroxide (and for this reason presented together with Compound II). The second one is the ferrous structure of both C*c*P and APX, obtained by complete reduction of the heme by X-ray radiation (presented at the end of the part 2). The nature of the ferric enzymes is instead broadly discussed in Chapter 3.

# 2.2. PART 1: THE STRUCTURE OF COMPOUND I

## 2.2.1. INTRODUCTION

The nature of Compound I in heme peroxidases has been extensively studied using a variety of techniques. Early studies were carried out on HRP and C*c*P by means of spectroscopic techniques such as XAS, EXAFS (*1-4*) and resonance Raman (*5, 6*). Afterwards more studies appeared and attention was drawn towards crystallographic methods (*7-9*). However, the picture that emerged was quite confusing. The original X-ray absorbance studies (XAS and EXAFS) (*1-4*) consistently proposed a model where the oxygen-iron distance was around 1.65 Å; this same result was later confirmed by studies on CPO (*10*). On the other hand, the crystallographic studies indicated an oxygen-iron distance ranging from about 1.75 to 1.90 Å. The difference between the measurements is significant. Theoretical studies (see Chapter 1) have shown that a distance of 1.65 Å is compatible with an oxy-ferryl species where the oxygen is unprotonated and forms a double bond with the ferryl ion ($Fe^{IV}$=O) (*11*) while a longer distance, around 1.80 Å, is consistent with formation of a ferryl species with a single bond and protonated oxygen ($Fe^{IV}$-OH) (*11*). Finally, distances in the range between 1.95 Å and 2.80-3.00 Å should correspond to formation of species spanning from ferric low spin heme (with strong field ligands such as $CN^-$ or $OH^-$) to ferric high spin (with weak field ligands such as water) (*11*). It is therefore clear, overall, that the results are inconsistent and the differences measured report on a change of the chemical properties of the ferryl species, which cannot be neglected.

Amongst the various causes for the inconsistency of the Fe-O distances measured, photoreduction may play a crucial role in crystallographic works (*8, 12, 13*)

as this effect may cause structural alterations of the heme-oxy intermediates during data collection. This is likely to be the case of Compound I of C*c*P previously determined (*7, 9*). Recently, photoreduction has been taken into account (*8, 14*). Berglund *et al.* (*8*) have published a structure of Compound I of HRP obtained by photoreduction of Compound III (due to the difficulty in isolating Compound I for this enzyme), whose purity, however, is only 80%. In conclusion, all the experimental data collected seem to provide a picture of Compound I that is still rather confused[1].

The work presented here addresses this issue and through the crystallographic, multicrystal study of Compound I of C*c*P, it provides the first precise determination of the structure of a Compound I in a heme peroxidase. Moreover, for the first time we present the structure of Compound I of APX, obtained through the photoreduction of APX Compound III, and solved by means of a multicrystal method using a high energy X-ray radiation (0.6 Å).

## 2.2.2. RESULTS

### *2.2.2.1. Compound I of CcP*

The structure of the Compound I intermediate of C*c*P has been determined using a multicrystal approach (using only a small percentage of the total data set (*8*)) to allow the collection of diffraction data before it is affected by photoreduction (Figure [2. 1]-A). Data and refinement statistics are shown in Table [2. 1]. The authenticity of this Compound I species was confirmed using single crystal microspectrophotometry (Figure [2. 2]-A). The spectrum shows the typical Compound I peaks (530, 560 and 632

[1] During the processing of the data reported here, a new multicrystal study of C*c*P Compound I appeared (14). The results reported are, at first approximation, consistent with the results presented here. See Discussion (section 2.3) for a more accurate comparison of the data.

nm) in the visible region, which is similar to previously published spectra (530 nm, 560 nm, 630sh nm (*15*)) and consistent with our spectra in solution under the same conditions (*i.e.* using the same ratio of [enzyme]:[H2O2], Figure [2. 2]-A).

**Figure [2. 1]: The structures of CcP Compound I (A) and APX Compound I (B), showing electron density maps calculated with coefficients $2F_o$-$F_c$ contoured at 2σ in blue and the $F_o$-$F_c$ map (contoured at 4σ, shown in green) calculated after refinement omitting the oxygen. Oxygen atoms are shown as red spheres, the heme is in red, and the iron is shown as an orange sphere. Key residues are labelled.**

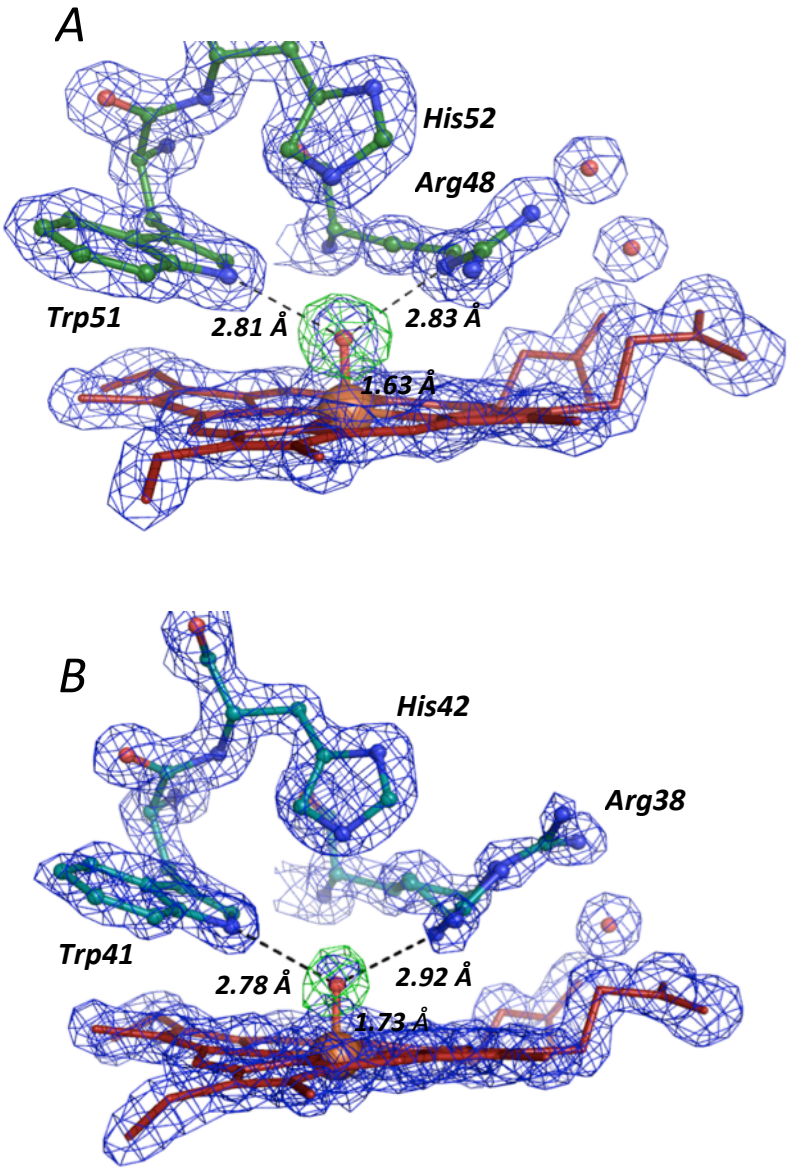

**Table [2. 1]: Statistics of X-ray data collection and refinement for Compound I of C*c*P and APX**

| **Data collection**[§] | **C*c*P* Compound I** | **APX** Compound I** |
|---|---|---|
| Space group | $P2_12_12_1$ | $P4_22_12$ |
| Cell dimension a, b, c (Å) | 51.04, 75.04, 106.80 | 82.03, 82.03, 75.23 |
| Resolution (Å) | 32.93 - 1.67 (1.76 - 1.67) | 30.00 - 1.50 (1.54 - 1.50) |
| $R_{merge}$ (%) | 6.6 (24.0) | 5.1 (33.2) |
| I /σI[§] | 10.9 (3.8) | 14.61 (4.48) |
| Completeness (%) | 92 (81) | 88.6 (84.7) |
| Multiplicity | 2.9 (2.6) | 3.0 (3.0) |
| **Refinement** | | |
| Resolution (Å) | 33.11 - 1.68 | 27.73 - 1.50 |
| No. reflections | 40890 | 37890 |
| $R_{work}/R_{free}$ (%) | 14.4 / 20.0 | 14.9 / 21.5 |
| Protein | 2425 | 2390 |
| Ligand/ion | 97 | 53 |
| Water | 685 | 463 |
| Overall *B*-factors | 16.39 | 19.32 |
| †ESU (Å) | 0.049 | 0.040 |
| R.m.s. deviations | | |
| Bond lengths (Å) | 0.01 | 0.01 |
| Bond angle distances (Å) | 0.024 | 0.024 |

[§]Outer bin data in brackets.

*Data collected at home source at wavelength λ=1.5418 Å merging together the first 9 degrees data from 10 crystals.

**Data collected at Diamond Light Source beam line IO4 at wavelength λ=0.6 Å merging the first 15 degrees data from 3 crystals.

As the atomic cross section decreases with the wavelength (*8*), the use of a high energy beam considerably reduced the photoelectric effect and thus decreased the number of crystals needed.

† Calculated by the maximum likelihood method (*16*).

The structure, Figure [2. 1]-A, reveals an electron density peak for the oxygen atom at 1.63 Å from the iron. This is considerably shorter than previous crystallographic estimates of the Compound I bond length in C*c*P (1.87 Å (*9*) and 1.7 – 2.0 Å (*7*)). The Estimated Standard Uncertainty (ESU) of the iron and oxygen atom positions calculated by full-matrix inversion (*17*) are 0.017 Å and 0.066 Å respectively. The overall structure of Compound I remains unchanged compared to that of the (nominally) ferric protein (pdb code 1ZBY). The ferryl iron is positioned about 0.3 Å out of the heme plane in the direction of the distal histidine; the proximal histidine moves with it to bring it closer to the heme plane. This structural shift might be important for stabilization of the high-valent heme intermediate. The $N_\varepsilon$ of Trp51 is seen to be within hydrogen bonding distance of the ferryl oxygen, as is the $N_\varepsilon$ of Arg48, Figure [2. 1]-A. The side chain of Arg48 has been observed in two orientations in ferric C*c*P – one with the guanidinium group positioned near the oxygen and above the iron ("in"), the other pointing away ("out") (*7, 9, 18*) – but only one of these ("in") is seen in the Compound I structure here.

Upon X-ray exposure, photoreduction occurs leading ultimately to the formation of ferrous heme. After the equivalent of the exposure needed to collect a full set of diffraction data (a dose of » 0.35 MGy), the spectrum corresponds to that of fully reduced, ferrous C*c*P (*vide infra, z*Figure [2. 7]-B), but this species first becomes evident after exposure to an absorbed dose of only 0.10 – 0.15 MGy, suggesting that photoreduction occurs very rapidly in the beam.

**Figure [2. 2]: UV-visible spectra of Compound I. A, comparison of the single crystal spectrum of CcP Compound I (solid line) and CcP Compound I in solution. B, single crystal spectrum of APX Compound I.**

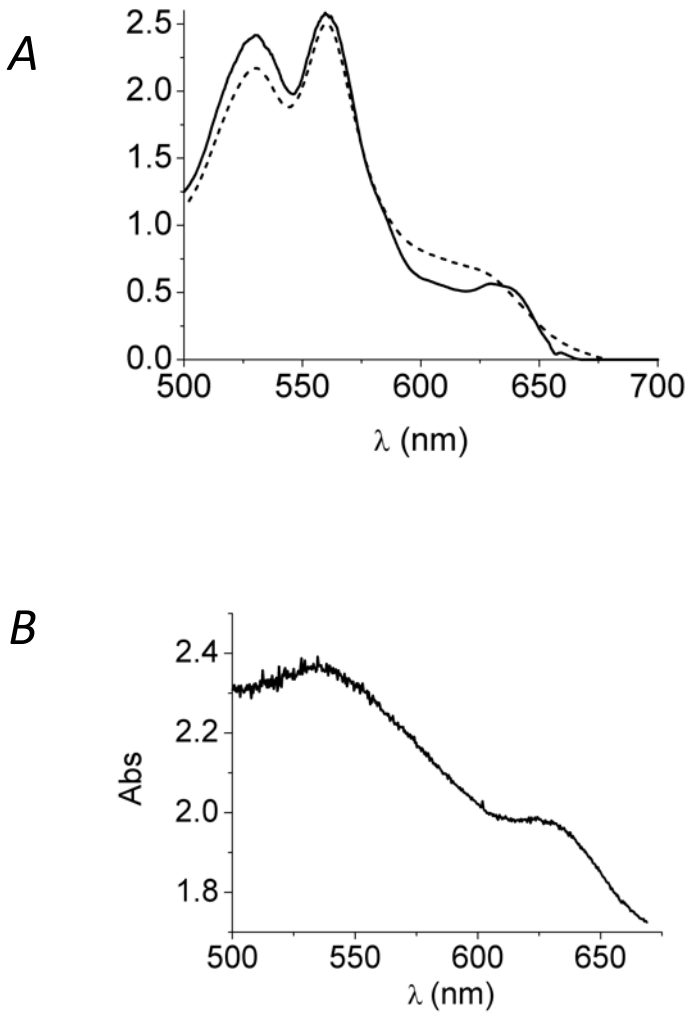


*2.2.2.2. Compound I of APX*

The Compound I intermediate of APX converts rapidly to Compound II (*19*), and we are thus unable to isolate this form in the crystal by soaking with peroxide. We can, however, access the Compound I intermediate through the ferrous-oxy ($Fe^{II}$-$O_2$) species (Compound III) which is used in other catalytic heme enzymes (such as the P450s) as a route to formation of Compound I. In peroxidases, the ferrous-oxy intermediate can be formed by reaction of Compound II with excess peroxide (*8*) and

will be discussed in the following section; photoreduction of the ferrous-oxy (Compound III) species thus formed in the crystal converts it to the desired Compound I by cleavage of the O-O bond (*8*). We observe that after a dose of ≈0.15 MGy, a structure is seen in which only a single atom of oxygen is bound in the distal position above the iron. Single crystal spectrophotometry (Figure [2. 2]-B) confirms that this is predominantly Compound I (*20*) and the structure is shown in Figure [2. 1]-B. In this case the multicrystal approach has been used together with high energy X-ray radiation (0.6 Å) in order to reduce the number of crystals needed for the analysis (*12, 21*) and to compensate for the lack of available APX crystals.

The structure of APX Compound I (Figure [2. 1]-B) shows an iron-oxygen bond length of 1.73 Å, which is slightly longer than that obtained for the Compound I structure of C*c*P above (most likely because the structure still contains some $O_2$ bound to the heme, residual ferrous-oxy heme) but still shorter than previous crystallographic measurements from C*c*P. The ESUs of the iron and oxygen positions (*17*) are 0.016 Å and 0.09 Å respectively.

### 2.2.3. DISCUSSION

Compound I of C*c*P is stable enough for its structure to be obtained directly. The single crystal spectra, and the similarity with the solution spectra, give a high degree of confidence that the structure corresponds to Compound I. Our crystallographic analyses for this ferryl intermediate in Compound I of C*c*P measures the bond length as 1.63 Å, firmly in the realm of an unprotonated iron-oxo double bond. It is substantially shorter than a previous estimate of 1.87 Å (*9*), but this structure was affected by

photoreduction. During data processing, Meharenna *et al.* published an analogous multicrystal study of C*c*P Compound I (*14*). Although potentially consistent with our results, those data indicate a slightly longer Fe-O distance in C*c*P Compound I (1.75 Å). Such a difference is likely to arise from the fact that Meharenna *et al.* (*14*) have used a slightly larger X-ray dose and consequently, on the basis of our results, we believe the structure they have presented is still affected by photoreduction (although only marginally).

Compound I of C*c*P can be compared directly with that of APX. Compound I of APX is not stable so its structure has been obtained indirectly, from photoreduction of the ferrous-oxy intermediate. Nevertheless, the single crystal spectra for the APX Compound I structure are consistent with published data in solution and the bond lengths in the two Compound I structures are in good agreement. For APX, the bond length is slightly longer (1.73 Å) than for C*c*P (1.63 Å), most likely due to the presence of residual ferrous-oxy heme (which would increase the apparent bond length). Both bond lengths for Compounds I of C*c*P and APX are shorter than other estimates (*7, 9*). *Both of the Compound I structures show an observed bond length consistent with an unprotonated ferryl ($Fe^{IV}$=O) heme species.*

The Compound I intermediates of APX and C*c*P are not exactly the same. C*c*P Compound I contains a tryptophan radical (Trp191) that is the site of the second oxidising equivalent (*22*). APX contains the equivalent tryptophan residue (Trp179), but does not use it; instead, APX Compound I contains a porphyrin $\pi$-cation radical and its spectrum thus differs from that of C*c*P Compound I. These spectroscopic features have sometimes appeared confusing and led to the classification of C*c*P Compound I as structurally equivalent to Compound II (*23*). Our data suggest that the difference in the

location of the second oxidising equivalent does not affect the nature of the oxy-ferryl species and actually C*c*P Compound I is structurally and chemically consistent with that of APX or HRP.

# 2.3. PART 2: THE STRUCTURE OF COMPOUND II AND NON-PHYSIOLOGICAL INTERMEDIATES

## 2.3.1. INTRODUCTION

In contrast to Compound I, Compound II is generally a stable and isolatable species in heme peroxidases. The preliminary studies on this species were those on Compound II of HRP (*1-3*) and were carried out by means of X-ray absorption methods. Nevertheless, the results proved rather contradictory. Penner-Hahn *et al.*(*2, 3*) reported data fitted by a model where both Compound I and Compound II had similar structures, suggesting that the $Fe^{IV}$-O distance was around 1.65 Å even in HRP Compound II. However similar studies carried out by Chance *et al.* (*1*) proposed a much longer iron(IV)-oxygen bond, set at 1.90 Å. More recent X-ray absorbance data on CPO (*23*) suggested an oxy-ferryl species instead with an Fe-O bond length of 1.82 Å, which was more compatible with a theoretical ferryl model possessing a protonated oxygen ($Fe^{IV}$-OH) (*11*). Finally an X-ray absorption study on Compound II of Mb (a species formed under non-physiological conditions by reacting the protein with $H_2O_2$) revealed an oxy-ferryl species with an oxygen atom at 1.69 Å from the iron.

An important contribution to the spectroscopic interpretation of the nature of Compound II also came from resonance Raman studies (*24-26*). In all the cases reported, the frequency of the vibration of the Fe-O bond was consistent with a model where the oxygen was unprotonated and sat at a distance of about 1.65 Å from the iron (*27*).

On the other hand, more recent structural information was obtained by means of X-ray crystallography. Berglund *et al.* (*8*) showed that in HRP, the Fe-O distance of

Compound II is 1.84 Å, while the structure of Compound II of Mb (*28*) showed an even longer bond length, set around 1.92 Å.

As for Compound I (Chapter 2, Part 1), the case of Compound II appears similarly confused. On the basis of theoretical calculations (*11*), the differences in the measurements are not negligible as the different bond lengths correspond to different chemical species (see Chapter 1). Moreover the fact that the use of different techniques yields different results implies that perhaps some systematic error might have occurred. Photoreduction can be one of these. The structure of Compound II of HRP (*8*) was obtained with a multicrystal method and therefore such an effect should be completely ruled out. However the inconsistency between some of the other results strongly suggests the requirement for new and more definitive data, which would cast new light on the discussion of the nature of Compound II in heme peroxidases and perhaps bring it to a conclusion. In this work we present for the first time the X-ray structure of "pure" sample of Compound II of APX. This was obtained using the combination of a multicrystal approach and high energy X-ray radiation to rule out the structural modifications caused by the photoreduction effect and simultaneously reduce the required number of crystals to a minimum (*21*). The structure of C*c*P Compound II obtained by photoreduction of its predecessor Compound I and solved by means of a multicrystal approach is also presented. Finally, in this Chapter the structure of Compound III (ferrous-oxy species) of APX is presented, obtained by reaction of Compound II with an excess of hydrogen peroxide and solved by means of a multicrystal method with the use of high energy X-ray radiation.

## 2.3.2. RESULTS

### *2.3.2.1. Compound II of cytochrome c peroxidase*

As for APX Compound I, Compound II of C*c*P is not stable enough to be trapped and isolated directly in the crystal, but can be accessed indirectly through photoreduction of Compound I. The spectrum of C*c*P Compound II is very similar to that of Compound I (the only difference between the two species is that the Trp191 radical has been reduced in Compound II (*15*)), which makes spectroscopic identification of Compound II in the crystal more difficult, but the intensity of the α- and β-bands decreases on reduction of Compound I to Compound II (*15*). To obtain a structure for C*c*P Compound II, we used diffraction data after an exposure of 0.15 – 0.20 MGy where the α- and β-bands decreased, but formation of ferrous heme is still negligible (as monitored by the presence of the characteristic 585 nm peak for the ferrous species, Figure [2. 4]-A, see also Paragraph 2.3.2.4.). Figure [2. 3]-A shows the structure of the Compound II species thus obtained (collection and refinement statistics reported in Table [2. 1]); single crystal spectra (Figure [2. 4]-A) confirm the assignment and are in agreement with previous spectra for Compound II (*15*).

In this case, the Fe-O distance is observed to clearly increase, and is now longer (1.83 Å) than that for both C*c*P Compound I (1.63 Å) and APX Compound I (1.73 Å) (Chapter 2, Part 1), and almost identical to that seen in APX Compound II (1.84 Å, *vide infra*). The ESUs of the iron and oxygen positions (*17*) are 0.017 Å and 0.065 Å respectively. Arg48 mostly remains in the "in" position although some positive electron density is observed that is consistent with a low occupancy in the "out" position.

**Table [2. 2]: Statistics of X-ray data collection and refinement for Compound II of C*c*P and APX and Compound III of APX**

| **Data collection**[§] | **C*c*P* Compound II** | **APX** Compound II** | **APX Compound III** |
|---|---|---|---|
| Space group | $P2_12_12_1$ | $P4_22_12$ | $P4_22_12$ |
| Cell dimension a, b, c (Å) | 51.05, 75.14, 106.92 | 81.82, 81.82, 75.24 | 81.97, 81.97, 75.16 |
| Resolution (Å) | 32.93 - 1.67 (1.76-1.67) | 30.00 - 1.65 (1.69 - 1.65) | 40.95 - 1.55 (1.59 - 1.55) |
| $R_{merge}$ (%) | 10.5 (26.8) | 7.4 (42.3) | 6.8 (65.0) |
| I /σI[§] | 5.4 (2.4) | 12.1 (2.11) | 13.15 (2.0) |
| Completeness (%) | 83.5 (75.8) | 99.7 (99.2) | 87.9 (69.7) |
| Multiplicity | 2.1 (2.0) | 3.6 (2.6) | 3.7 (1.4) |
| **Refinement** | | | |
| Resolution (Å) | 33.13-1.68 | 27.7-1.65 | 57.96-1.55 |
| No. reflections | 43031 | 40250 | 50009 |
| $R_{work}/R_{free}$ (%) | 14.8/19.9 | 14.3/19.9 | 16.0/20.4 |
| Protein | 2456 | 2297 | 2295 |
| Ligand/ion | 97 | 55 | 57 |
| Water | 745 | 524 | 479 |
| Overall *B*-factors | 17.62 | 16.8 | 17.8 |
| †ESU (Å) | 0.052 | 0.053 | 0.044 |
| R.m.s. deviations | | | |
| Bond lengths (Å) | 0.01 | 0.02 | 0.01 |
| Bond angle distances (Å) | 0.025 | 0.025 | 0.026 |

[§]Outer bin data in brackets.

*Data collected at home source at wavelength λ=1.5418 Å merging together the first 9 degrees data from 10 crystals.

**Data collected at Diamond Light Source beam line IO4 at wavelength λ=0.6 Å merging the first 15 degrees data from 3 crystals.

As the atomic cross section decreases with the wavelength (*8*), the use of a high energy beam considerably reduced the photoelectric effect and thus decreased the number of crystals needed.

† Calculated by the maximum likelihood method (*16*) .

**Figure [2. 3]: The structures of CcP Compound II (A) and APX Compound II (B), showing electron density maps calculated with coefficients $2F_o$-$F_c$ contoured at 2σ in blue and the $F_o$-$F_c$ map (contoured at 4σ, shown in green) calculated after refinement omitting the oxygen. Oxygen atoms are shown as red spheres, the heme is in red, and the iron is shown as an orange sphere. Key residues are labelled.**

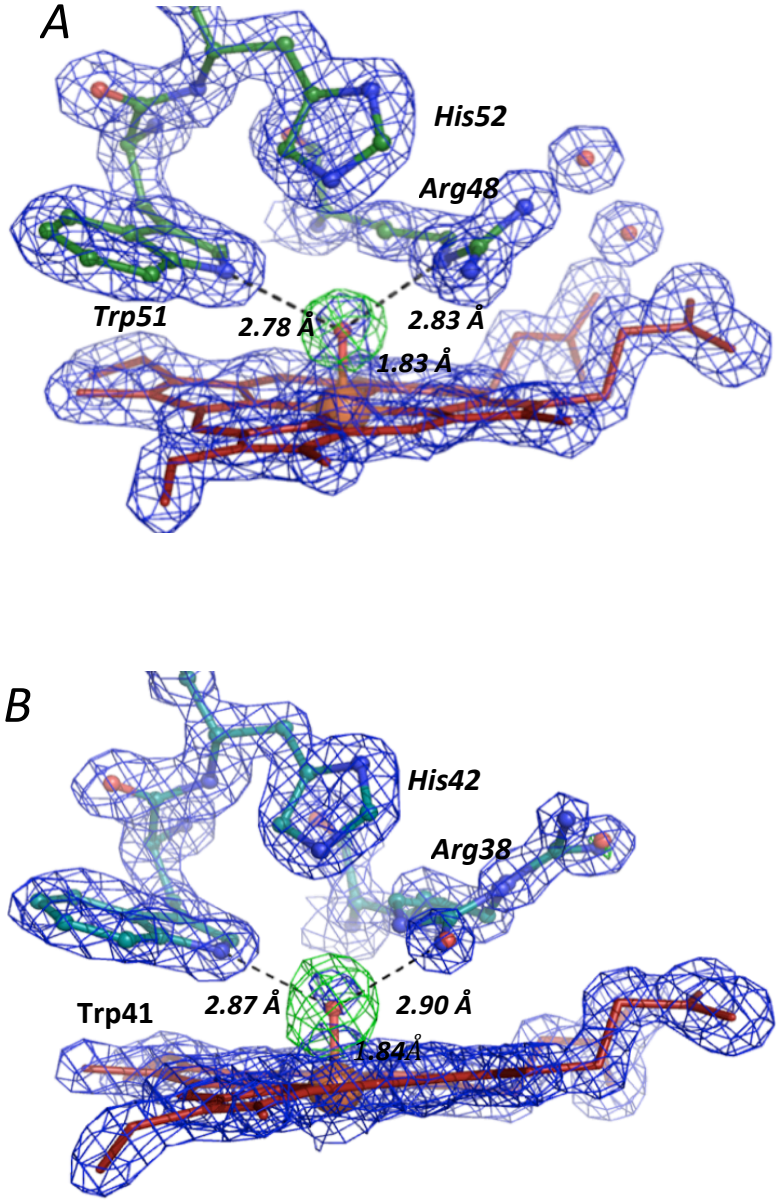

**Figure [2. 4]: UV-visible spectra of Compound II. A, comparison of the single crystal spectrum of C*c*P Compound II (solid line), C*c*P Compound I (dotted line) and ferrous C*c*P (dashed-dotted line). B, comparison of the single crystal spectrum of APX Compound II (solid line) with the spectrum of APX Compound II in solution (dotted line)**

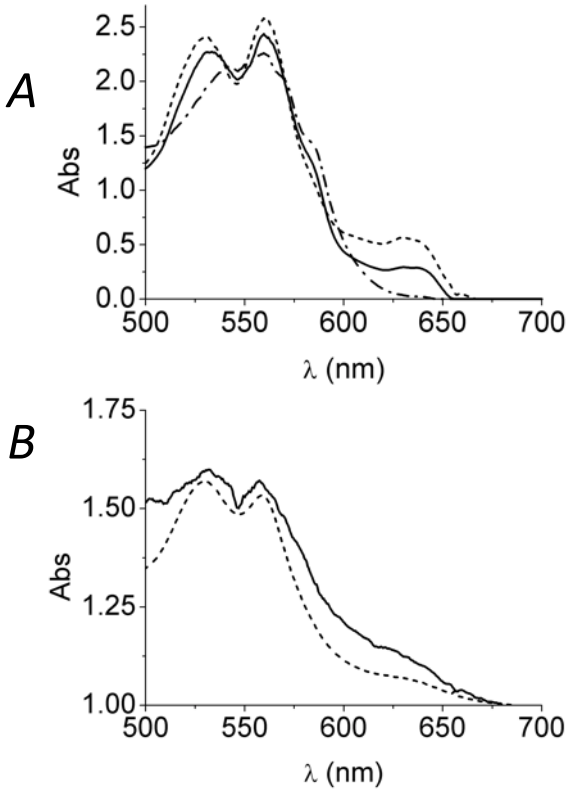


*2.3.2.2. Compound II of ascorbate peroxidase*

Compound II of APX is an isolatable species (*20*) and its structure was directly solved using the multicrystal approach to avoid photoreduction. Even in this case the multicrystal approach was used in combination with high energy X-ray radiation (wavelength of λ=0.6 Å). This considerably diminished the number of crystals needed for the study, given the much smaller photoreduction effect occurring in these conditions (*12*) (see Chapter 1), thus accommodating the low number of available crystals of APX.

The corresponding structure of the Compound II of APX is shown in Figure [2. 3]-B. Microspectrophotometry was used to unambiguously confirm that the crystal was

Compound II (Figure [2. 4]-B). Peaks are observed at 531 and 558 nm, which compare well with the spectrum of Compound II obtained in solution by reaction of ferric APX with peroxide under the same conditions ($\lambda_{max}$= 530 nm, 559 nm) and shown for comparison in Figure [2. 4]-B. In this Compound II crystal structure, the iron-oxygen bond length is 1.84 Å, which is 0.21 Å longer than that for the Compound I derivative of C*c*P above. The ESU of the iron and oxygen positions (17) are 0.015 Å and 0.088 Å respectively. Compared to Compound I this clearly indicates a lengthening of the Fe-O bond in the Compound II structure. The similarity of the single crystal and solution spectra for Compound II (Figure [2. 4]-B), and the fact that the bond length for the Compound II species is much shorter than that for either the published ferric (2.08 Å) or ferrous APX (2.20 Å see Paragraph 2.3.4.), provides confidence that the assignment of the structure as a Compound II species is correct. The ferryl iron also moves out of the heme plane by 0.15 Å toward the distal histidine (compared to the ferric enzyme) and the proximal histidine (His163) also shifts in the same direction, in the same way as observed for Compound I of C*c*P (Paragraph 2.2.). The side chain of the distal arginine is seen in both the "in" (as in Compound I) and "out" (as in the ferric enzyme) conformations.

#### *2.3.2.3. Compound III of ascorbate peroxidase*

Compound III ($Fe^{II}$-$O_2$, also referred to as ferrous-oxy) is a feature of oxygen-activator enzymes like the cytochromes P450, where it is formed as a short-lived species that quickly decays to produce Compound I (Scheme [1. 1]). In heme peroxidases, the ferrous-oxy intermediate can be formed from reaction of Compound II with excess peroxide (*8*). The ferrous-oxy species is analogous to the ferric-

hydroperoxide species (sometimes referred to as Compound 0, $Fe^{III}$-OOH) that precedes Compound I, and can therefore report on this transient precursor.

**Figure [2. 5]: The structures of APX Compound III, showing electron density maps calculated with coefficients $2F_o$-$F_c$ contoured at 2σ in blue and the $F_o$-$F_c$ map (contoured at 4σ, shown in green) calculated after refinement omitting the oxygen. Oxygen atoms are shown as red spheres, the heme is in red, and the iron is shown as an orange sphere. Key residues are labelled.**

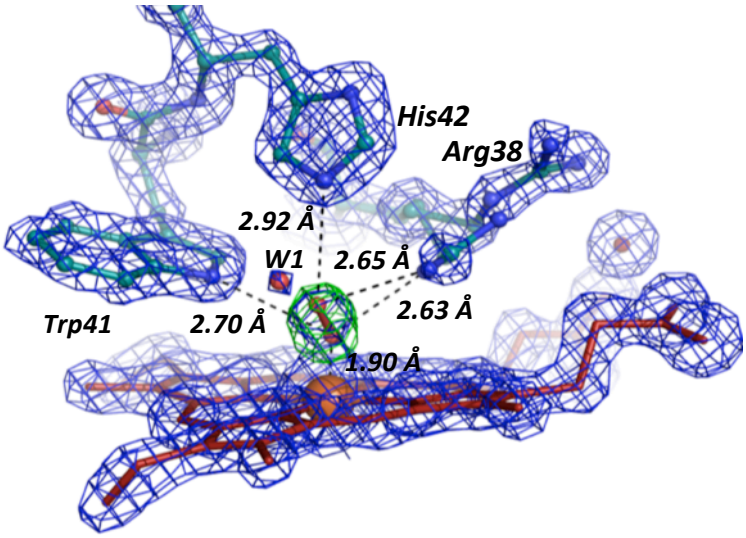


**Figure [2. 6]: UV-visible spectra of APX Compound III**

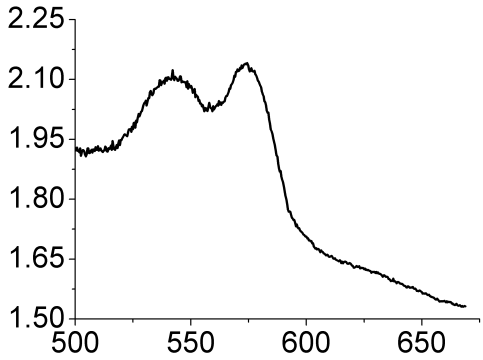


The structure of Compound III of APX is shown in Figure [2. 5]. It must be noted that since C*c*P does not form a stable Compound II, Compound III for this enzyme cannot be produced. An electron density peak larger than those observed for the Compound I and Compound II structures is clearly seen and interpreted as a dioxygen species. This is confirmed by single crystal spectrophotometry (peaks at 548 and 575

nm, Figure [2. 6]). There are hydrogen-bonding interactions from the $O_1$ of the bound ligand to $N_\varepsilon$ of His42 (2.92 Å), $N_\varepsilon$ of Trp41 (2.70 Å) and $N_\varepsilon$ of Arg38 (2.65 Å). In this case, Arg38 (equivalent to Arg48 in C*c*P) is observed occupying both "in" and "out" positions and there is a water molecule, seen adjacent to Trp41 (W1 in Figure [2. 5]), which shifts away from the heme to accommodate the bound $O_2$ species. Photoreduction leads to cleavage of the O-O bond and ultimate formation of Compound I (*8*).

### *2.3.2.4. The structure of ferrous CcP and APX*

The photoreduction occurring during data collection ultimately leads to the formation of ferrous heme. This can be observed in Figure [2. 7] that shows the change in UV-visible absorbance for Compound I of C*c*P and Compound II of APX during X-ray exposure. After a dose equivalent to the collection of a full data set (≈0.35 MGy), the spectrum, in both cases, corresponds to that of fully reduced, ferrous enzyme, although first evidence for formation of this species appears already at about 10-15% of the full dose suggesting that photoreduction occurs very rapidly in the beam. We have used this photoreduction to obtain a structure for ferrous C*c*P (Figure [2. 8]-A) and ferrous APX (Figure [2. 8]-B, statistics shown in Table [2. 3]). In these structures, the bond length to the distal oxygen atom is 2.01 Å and 2.20 Å respectively for C*c*P and APX, which clearly distinguishes them from that of the Compound I (1.63 Å and 1.73 Å) and Compound II (1.83 Å and 1.84 Å) species. It is possible to note that previously published ferric structures of C*c*P (2CYP and 1ZBY), which have bond lengths of 2.40 and 2.33 Å, respectively, would also be expected to be reduced and thus are probably

a mixture of ferrous and ferric states. Furthermore, a similar elongated bond (2.10 Å) is also observed for one of the published structures of ferric APX (1AOF).

**Figure [2. 7]: Photoreduction occurring during X-ray exposure monitored by UV-single crystal spectrophotometry. A, photoreduction observed on Compound I of C*c*P. B, photoreduction observed on Compound II of APX. Insets show comparison of the first (solid line) and last (dotted line) spectra recorded.**

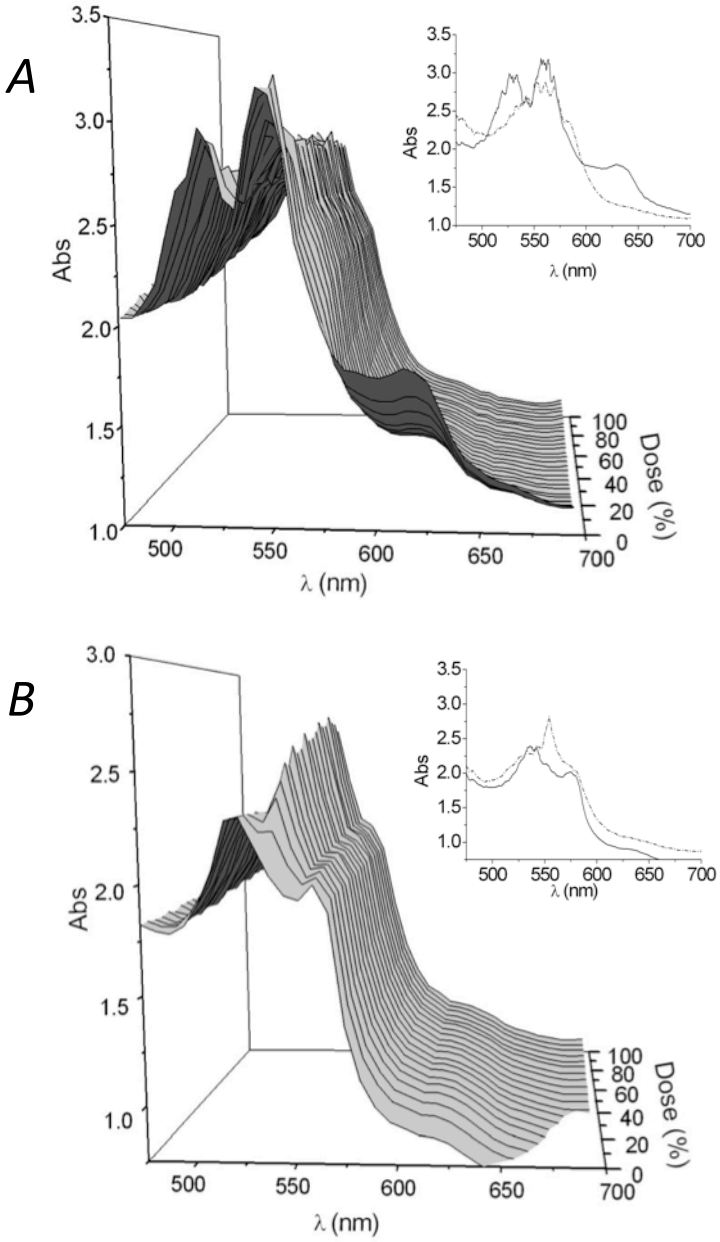

**Table [2. 3]: Statistics of X-ray data collection and refinement for ferrous C*c*P and APX**

| **Data collection**[§] | **Ferrous C*c*P*** | **Ferrous APX**** |
|---|---|---|
| Space group | $P2_12_12_1$ | $P4_22_12$ |
| Cell dimension a, b, c (Å) | 51.05, 75.19, 106.95 | 82.24, 82.24, 75.38) |
| Resolution (Å) | 33.16 - 1.69 (1.78 - 1.69) | 37.67 - 1.70 (1.79 - 1.70) |
| $R_{merge}$ (%) | 6.2 (25.5) | 10.0 (56.0) |
| I /σI[§] | 15.8 (4.0) | 9.1 (2.4) |
| Completeness (%) | 99.4 (97.2) | 94.5 (88.4) |
| Multiplicity | 5.1 (4.5) | 3.7 (3.7) |
| **Refinement** | | |
| Resolution (Å) | 33.15-1.69 | 36.79-1.70 |
| No. reflections | 44336 | 25721 |
| $R_{work}/R_{free}$ (%) | 15.4/19.0 | 15.2/20.2 |
| Protein | 2392 | 1905 |
| Ligand/ion | 97 | 53 |
| Water | 556 | 434 |
| Overall *B*-factors | 17.45 | 15.44 |
| †ESU (Å) | 0.047 | 0.067 |
| R.m.s. deviations | | |
| Bond lengths (Å) | 0.01 | 0.01 |
| Bond angle distances (Å) | 0.024 | 0.026 |

[§]Outer bin data in brackets.

*Data collected at home source at wavelength λ=1.5418 Å merging together the first 9 degrees data from 10 crystals.

**Data collected at Diamond Light Source beam line IO4 at wavelength λ=0.6 Å merging the first 15 degrees data from 3 crystals.

As the atomic cross section decreases with the wavelength (*8*), the use of a high energy beam considerably reduced the photoelectric effect and thus decreased the number of crystals needed.

† Calculated by the maximum likelihood method (*16*).

**Figure [2. 8]: The structures of ferrous CcP (A) and ferrous APX (B) obtained by photoreduction, showing electron density maps calculated with coefficients $2F_o$-$F_c$ contoured at 2σ in blue and the $F_o$-$F_c$ map (contoured at 4σ, shown in green) calculated after refinement omitting the oxygen. Oxygen atoms are shown as red spheres, the heme is in red, and the iron is shown as an orange sphere. Key residues are labelled.**

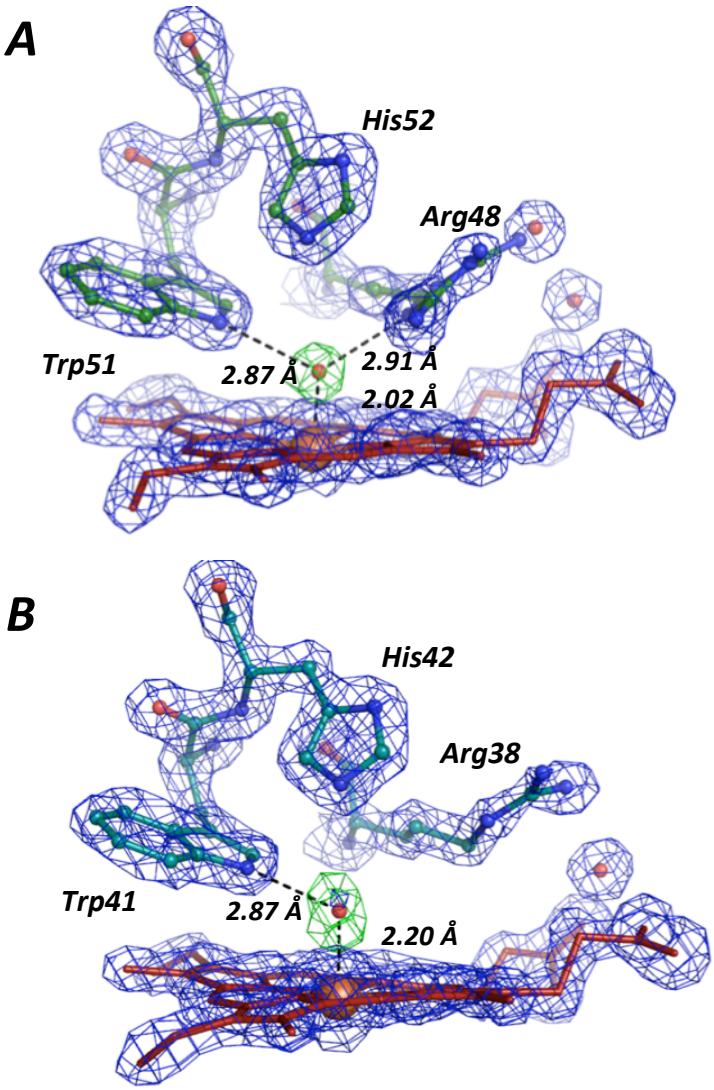

## 2.3.3. DISCUSSION

### *2.3.3.1. The nature of Compound II*

Here two Compound II structures are presented. The APX Compound II structure is the most reliable: APX Compound II is well documented by us (*20*) and others (*29*) as an isolatable species. The single crystal spectra presented for APX Compound II unambiguously confirm this assignment. For Compound II of APX, the bond length is clearly observed as longer (1.84 Å) than for either of the Compound I structures, consistent with a protonated $Fe^{IV}$-OH (single) bond (*11, 30, 31*). This is confirmed in the Compound II structure of C*c*P: in this case, due to the difficulty in isolating the species, the structure is obtained indirectly, by photoreduction of Compound I, but the bond also lengthens (to 1.83 Å).

The experiments therefore provide then evidence for lengthening of the bond on reduction of Compound I to Compound II in both enzymes, consistent (see Chapter 1) with protonation of the ferryl heme on reduction. The convergence of the results obtained here for APX and C*c*P also suggests that the very same mechanism could be conserved in all heme peroxidases in general, and this is supported by other structural analyses (*8, 23*).

Previous studies (*23, 32*) have suggested that the protonation state of the oxygen atom in the ferryl intermediates could be driven by the $pk_a$ of the oxy-ferryl species, which, in turn, was modulated by the proximal heme ligation. The work generally indicated that oxy-ferryl species with a proximal histidine-ligation (HRP, MB and C*c*P) had a low $pk_a$, resulting in an unprotonated oxygen at the pH values of previously published studies (*1-3, 33*). On the contrary, higher $pk_a$, consistent with protonated

oxygen atoms, were observed for oxy-ferryl species with a proximal thiolate-ligation like CPO. However, the crystallographic data reported here, together with what was observed for HRP (*8*), seem to suggest that, regardless of the proximal ligation, Compounds II, in heme peroxidases, present a protonated oxy-ferryl species.

### *2.3.3.2. The nature of Compound III*

As described in Chapter 1, Compound 0 is the very first intermediate formed upon reaction of the heme peroxidases with hydrogen peroxide. Unfortunately Compound 0 is a very unstable species that quickly decays to form Compound I (Scheme [1. 1]) and therefore it has never been isolated. Nevertheless it has been suggested (*8*) that Compound III (also referred to as the ferrous-oxy species, $Fe^{II}$-$O_2$) can be regarded as a species structurally equivalent to Compound 0 and as such, it can report on the very beginning of the reaction of heme peroxidases with hydrogen peroxide. The structure of Compound III of APX reported here (Figure [2. 5]) shows that no structural rearrangements have occurred to accommodate the oxygen molecule and this is secured to the distal side of the heme by means of a number of hydrogen bonds, which involve the side chains of the conserved distal histidine, tryptophan and arginine. By comparison with the structure of the oxy-ferrous species of HRP (pdb entry 1h57 (*8*)) it is possible to observe that in both enzymes the molecules of oxygen have a very similar orientation (Figure [2. 9]). The HRP (belonging to Class III) lacks in the distal tryptophan and in this case only two hydrogen bonds ensure the oxygen to the distal cavity and they involve the histidine and the arginine (Figure [2. 9]-A). Comparison of the two structures, therefore, may suggest that a

major role in binding and activating the hydrogen peroxide is played only by the distal arginine and histidine.

**Figure [2. 9]: Comparison between Compound III of HRP (A) and APX (B). Oxygen atoms are shown as red spheres, the heme is in red, and the iron is shown as an orange sphere. Key residues are labelled.**

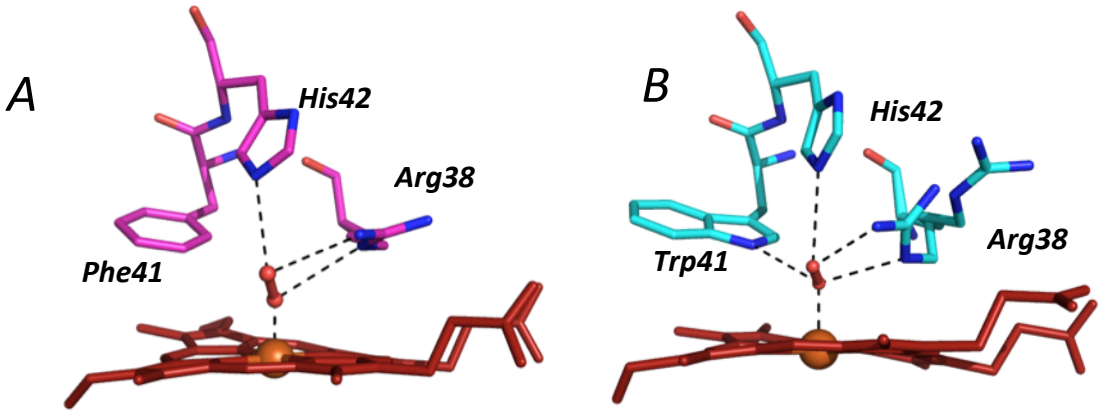

## 2.4. SUMMARY

All of the structures presented in this chapter are summarised and compared in Scheme [2. 1]. The two proteins share high sequence identity, and their overall structures are very similar. This allows a direct and meaningful comparison of the structures of the intermediates in two different proteins. Together with the structures of the ferrous and ferrous-oxy (the latter for APX only) species, this provides a detailed comparative picture of the key redox states (Scheme [2. 1]).

**Scheme [2. 1]: The structures of CcP Compound I and APX Compounds II and III were obtained by reaction with hydrogen peroxide; Compound II of CcP and Compound I of APX were obtained by photoreduction of Compound I and Compound III, respectively. The structures of the ferric CcP and APX enzymes are taken from the Protein Data Bank (2ZBY and 1OAG). $X^{+\bullet}$ represents either a porphyrin π-cation radical or a tryptophan radical (APX or CcP, respectively).**

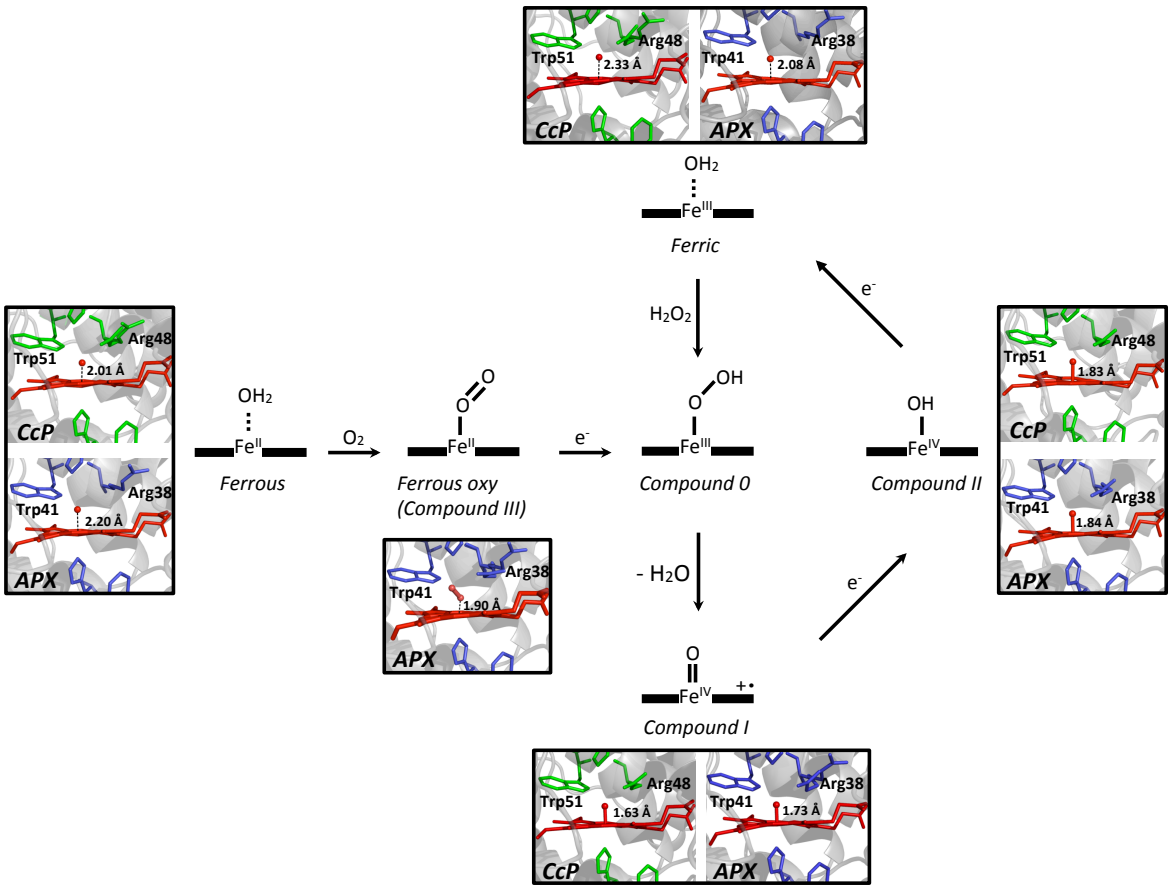

By means of a multicrystal method, it has been possible to rule out the effect of photoreduction and determine, for the first time, the unbiased structure of the isolatable Compound I of C*c*P and Compound II of APX. Data show that the Fe-O bond distance is different for the two species. For Compound I Fe-O distance is 1.63 Å whereas for Compound II the bond length is 1.84 Å. Furthermore, theoretical studies (reported in Chapter 1) have shown that in the first case the reported distance is consistent with formation of a double bond between iron and oxygen and the oxygen atom is unprotonated. In the second case, the oxygen is protonated and only a single bond is between the two atoms.

The structures of Compound I of APX and Compound II of C*c*P have been also determined, although, owing to the practical limitations in isolating these species, they have been obtained indirectly by photoreduction of the relative precursors. Precisely, Compound I of APX has been produced by photoreduction of Compound III whereas Compound II of C*c*P has been obtained by photoreduction of Compound I. Nevertheless, the results obtained draw a consistent picture in which Compound I of APX (Fe-O distance 1.73 Å) compares well with C*c*P Compound I and so does Compound II of C*c*P (Fe-O bond distance 1.83 Å) with APX Compound II. The consistency of these results propose a definitive model for peroxidases in which the oxy-ferryl species in Compound I is unprotonated whereas it is protonated in Compound II. This consideration implies, then, that a proton is delivered to the oxy-ferryl ion during reduction of Compound I to Compound II.

Finally, the structures of APX Compound III, ferrous APX and ferrous C*c*P presented in this chapter have provided models which are important for the

understanding of heme peroxidases and, furthermore, are interesting for the understanding of the other heme enzymes such as the cytochromes P450.

**Reference**


1. Chance, B., Powers, L., Ching, Y., Poulos, T., Schonbaum, G. R., Yamazaki, I., and Paul, K. G. (1984) X-ray absorption studies of intermediates in peroxidase activity, *Arch Biochem Biophys 235*, 596-611.
2. Penner-Hahn, J. E., McMurry, T. J., Renner, M., Latos-Grazynsky, L., Eble, K. S., Davis, I. M., Balch, A. L., Groves, J. T., Dawson, J. H., and Hodgson, K. O. (1983) X-ray absorption spectroscopic studies of high valent iron porphyrins. Horseradish peroxidase compounds I and II and synthetic models, *J Biol Chem 258*, 12761-12764.
3. Penner-Hahn, J. E., Eble, K. S., Mcmurry, T. J., Renner, M., Balch, A. L., Groves, J. T., Dawson, J. H., and Hodgson, K. O. (1986) Structural Characterization of Horseradish-Peroxidase Using Exafs Spectroscopy - Evidence for Fe=O Ligation in Compound-I and Compound-Ii, *Journal of the American Chemical Society 108*, 7819-7825.
4. Chance, M., Powers, L., Poulos, T., and Chance, B. (1986) Cytochrome c peroxidase compound ES is identical with horseradish peroxidase compound I in iron-ligand distances, *Biochemistry 25*, 1266-1270.
5. Hashimoto, S., Teraoka, J., Inubushi, T., Yonetani, T., and Kitagawa, T. (1986) Resonance Raman study on cytochrome c peroxidase and its intermediate. Presence of the Fe(IV) = O bond in compound ES and heme-linked ionization, *J Biol Chem 261*, 11110-11118.
6. Reczek, C. M., Sitter, A. J., and Terner, J. (1989) Resonance Raman characterization of heme Fe(IV)=O groups of intermediates of yeast cytochrome C peroxidase and lactoperoxidase, *Journal of Molecular Structure 214*, 27-41.
7. Fulop, V., Phizackerley, R. P., Soltis, S. M., Clifton, I. J., Wakatsuki, S., Erman, J., Hajdu, J., and Edwards, S. L. (1994) Laue diffraction study on the structure of cytochrome c peroxidase compound I, *Structure 2*, 201-208.
8. Berglund, G. I., Carlsson, G. H., Smith, A. T., Szoke, H., Henriksen, A., and Hajdu, J. (2002) The catalytic pathway of horseradish peroxidase at high resolution, *Nature 417*, 463-468.
9. Bonagura, C. A., Bhaskar, B., Shimizu, H., Li, H., Sundaramoorthy, M., McRee, D. E., Goodin, D. B., and Poulos, T. L. (2003) High-resolution crystal structures and spectroscopy of native and compound I cytochrome c peroxidase, *Biochemistry 42*, 5600-5608.
10. Stone, K. L., Behan, R. K., and Green, M. T. (2005) X-ray absorption spectroscopy of chloroperoxidase compound I: Insight into the reactive intermediate of P450 chemistry, *Proceedings of the National Academy of Sciences of the United States of America 102*, 16563-16565.
11. (1982) *Iron Porphyrins*, Vol. 1, ADDISON-WESLEY Publishing company.
12. Unno, M., Chen, H., Kusama, S., Shaik, S., and Ikeda-Saito, M. (2007) Structural characterization of the fleeting ferric peroxo species in myoglobin: experiment and theory, *Journal of the American Chemical Society 129*, 13394-13395.
13. Hersleth, H.-P., and Andersson, K. K. (2010) How different oxidation states of crystalline myoglobin are influenced by X-rays, *Biochimica et Biophysica Acta (BBA) - Proteins & Proteomics In Press, Corrected Proof*.

14. Meharenna, Y. T., Doukov, T., Li, H. Y., Soltis, S. M., and Poulos, T. L. (2010) Crystallographic and Single-Crystal Spectral Analysis of the Peroxidase Ferryl Intermediate, *Biochemistry 49*, 2984-2986.
15. Pond, A. E., Bruce, G. S., English, A. M., Sono, M., and Dawson, J. H. (1998) Spectroscopic study of the compound ES and the oxoferryl compound II states of cytochrome c peroxidase: comparison with the compound II of horseradish peroxidase, *Inorganica Chimica Acta 275-276*, 250-255.
16. Murshudov, G. N., Vagin, A. A., and Dodson, E. J. (1997) Refinement of macromolecular structures by the maximum-likelihood method, *Acta Crystallogr D Biol Crystallogr 53*, 240-255.
17. Sheldrick, G. (2008) A short history of SHELX, *Acta Crystallographica Section A 64*, 112-122.
18. Edwards, S. L., Nguyen, H. X., Hamlin, R. C., and Kraut, J. (1987) Crystal structure of cytochrome c peroxidase compound I, *Biochemistry 26*, 1503-1511.
19. Lad, L., Mewies, M., Basran, J., Scrutton, N. S., and Raven, E. L. (2002) Role of histidine 42 in ascorbate peroxidase. Kinetic analysis of the H42A and H42E variants, *Eur J Biochem 269*, 3182-3192.
20. Lad, L., Mewies, M., and Raven, E. L. (2002) Substrate binding and catalytic mechanism in ascorbate peroxidase: evidence for two ascorbate binding sites, *Biochemistry 41*, 13774-13781.
21. Pavlinsky, G. V. (2008) *Fundamentals of X-Ray Physics*, Cambridge International Science Publishing, Cambridge, , GBR.
22. Sivaraja, M., Goodin, D. B., Smith, M., and Hoffman, B. M. (1989) Identification by ENDOR of Trp191 as the free-radical site in cytochrome c peroxidase compound ES, *Science 245*, 738-740.
23. Green, M. T., Dawson, J. H., and Gray, H. B. (2004) Oxoiron(IV) in chloroperoxidase compound II is basic: implications for P450 chemistry, *Science 304*, 1653-1656.
24. Sitter, A. J., Reczek, C. M., and Terner, J. (1985) Heme-linked ionization of horseradish peroxidase compound II monitored by the resonance Raman Fe(IV)=O stretching vibration, *J Biol Chem 260*, 7515-7522.
25. Chuang, W. J., Heldt, J., and Van Wart, H. E. (1989) Resonance Raman spectra of bovine liver catalase compound II. Similarity of the heme environment to horseradish peroxidase compound II, *Journal of Biological Chemistry 264*, 14209-14215.
26. Sitter, A. J., Reczek, C. M., and Terner, J. (1985) Observation of the FeIV=O stretching vibration of ferryl myoglobin by resonance Raman spectroscopy, *Biochimica et Biophysica Acta (BBA) - Protein Structure and Molecular Enzymology 828*, 229-235.
27. Behan, R. K., and Green, M. T. (2006) On the status of ferryl protonation, *Journal of Inorganic Biochemistry 100*, 448-459.
28. Hersleth, H. P., Dalhus, B., Gorbitz, C. H., and Andersson, K. K. (2002) An iron hydroxide moiety in the 1.35 A resolution structure of hydrogen peroxide derived myoglobin compound II at pH 5.2, *J Biol Inorg Chem 7*, 299-304.
29. Bursey, E. H., and Poulos, T. L. (2000) Two Substrate Binding Sites in Ascorbate Peroxidase: The Role of Arginine 172, *Biochemistry 39*, 7374-7379.

30. Conradie, J., Swarts, J. C., and Ghosh, A. (2004) Models of High-Valent Heme Protein Intermediates: A Quantum Chemical Study of Iron(IV) Porphyrins with Two Univalent Axial œÄ-Bonding Ligands, *The Journal of Physical Chemistry B 108*, 452-456.
31. Rovira, C., and Fita, I. (2003) The Proximal Hydrogen-Bonded Residue Controls the Stability of the Compound II Intermediate of Peroxidases and Catalases, *The Journal of Physical Chemistry B 107*, 5300-5305.
32. Green, M. T. (2006) Application of Badger's Rule to Heme and Non-Heme Iron, Oxygen Bonds. An Examination of Ferryl Protonation States, *Journal of the American Chemical Society 128*, 1902-1906.
33. Chance, M., Powers, L., Kumar, C., and Chance, B. (1986) X-ray absorption studies of myoglobin peroxide reveal functional differences between globins and heme enzymes, *Biochemistry 25*, 1259-1265.

Chapter 3

# HYDROGEN BONDS IN FERRIC CYTOCHROME *C* PEROXIDASE: A COMBINED X-RAY AND NEUTRON STUDY

## 3.1. INTRODUCTION

Amongst the various aspects of heme peroxidases yet to be clarified, two can be considered the most prominent. The first is related to the nature of the oxy-ferryl intermediates, Compound I and Compound II, and it has been discussed in Chapter 2 (*1*), whereas the second is related to the identification of the protonation states of the key residues and is discussed here.

Crystallographic determination of the protonation states of the key residues allows the identification of the hydrogen bond networks which entail them and control the reactivity of the enzyme. Therefore, characterisation of these bonds may provide crucial insights into the understanding of the reaction mechanism of heme peroxidases. However, crystallographic observation of protons is not an easy task. X-ray crystallographic techniques have limitations in determining protonation states since hydrogen atoms, with only one electron, scatter X-rays very weakly and thus are not normally visible in electron density maps. Although the protonation state may sometimes be deduced from heavy atom bond lengths, when high resolution data are available (better than about 1.2 Å), identification of hydrogen atoms which are exacerbated by their degree of thermal motion, such that labile hydrogen atoms (B factors > ≈10), is nonetheless extremely difficult (*2*).

In neutron diffraction, the scattering centres are the atomic nuclei and the atomic neutron scattering length is independent of the number of electrons. Instead, it depends on the nuclear forces and can vary even between isotopes of the same element. Notably, this is the case for hydrogen (H) and deuterium (D) nuclei. Hydrogen, with a negative scattering length, is easily distinguishable from deuterium with a

positive and greater scattering length, and can be observed with diffraction data at $d_{min}$ of 2.5 Å (*3*). In addition, the neutron scattering magnitude of deuterium atoms is comparable to that of the other atoms of the macromolecule such that they are similarly visible. An additional experimental problem is that X-rays induce a photoreduction effect, which may alter the structure of the molecule in question. This is a particular problem for metal-containing redox enzymes, and has been reported in several heme enzymes (*1, 4, 5*). In contrast, photoreduction is not induced during neutron diffraction experiments, as there is no interaction of the diffracting radiation with the electrons. The absence of radiation-induced damage means that structures do not need to be determined at cryogenic temperatures, thus avoiding freezing-induced artefacts that may arise as a consequence. Neutron crystallography can therefore complement X-ray structure determination by providing a more complete description of the structure.

Historically, neutron crystallography has been limited by a number of factors: the availability of only a few facilities (*6*), the low intensity of the neutron beams, and the requirement for very large crystals. However, improvements in both sample preparation and instrumentation for neutron macromolecular crystallography mean that useful neutron diffraction data can now be obtained from deuterated crystals (*i.e.* crystals exchanged in $D_2O$) with volumes of less than 1 $mm^3$ and from perdeuterated crystals (*i.e.* fully deuterated) with volumes of around 0.1 – 0.2 $mm^3$ (*7*). Combining neutron and X-ray diffraction data allows for robust refinement of heavy atom positions and further increases the scope of the technique (*8*).

C*c*P crystallises very easily (*9*), and relatively large crystals can be grown (up to ≈1 $mm^3$) making it an excellent system to study via neutron diffraction techniques. In this

work, the results from a combined room temperature X-ray and neutron study of ferric C*c*P are presented, in which the final structure has been jointly refined against both types of diffraction data. This is the first neutron structure of a heme enzyme and is also the first structure of ferric C*c*P unaffected by photoreduction at room temperature. Also presented in this chapter are the first X-ray structures of ferric C*c*P and APX, determined under cryogenic conditions (100 K), using multiple crystals to avoid photoreduction (*1*). This allows us to distinguish the effects of temperature from those of photoreduction. The structures presented here are compared and discussed in the context of proton delivery and catalytic mechanism.

## 3.2. RESULTS

### 3.2.1. DEUTERATION AND PERDEUTERATION OF C*c*P.

For this work, both deuteration and perdeuteration of C*c*P crystals were attempted. While deuteration was easily achieved by growing the crystals in normal conditions and finally exchanging them in deuterated mother liquor for at least 24 hours, perdeuteration required a longer procedure, involving the use of a new expression vector, carrying kanamycin resistance (pLEICS-03, see Appendix B), and expression in minimal medium with a deuterated carbon source. Various conditions for C*c*P expression in minimal medium were analysed (see Chapter 5, section 5.2.1.2.) and the corresponding expression levels were assessed by SDS-PAGE. A picture of this gel is reported in Figure [3. 1].

**Figure [3. 1]: Coomassie blue stained 15% SDS-PAGE gel of cell lysate in several conditions for C*c*P expression in minimal medium. Lane A: uninduced expression, after 24h incubation; lane B: 24h incubation after induction with IPTG (final conc. 1 mM); lane C: 60h incubation after induction with IPTG (final conc. 1 mM); lane D: as lane B using media with double concentration of glucose (4 g/L); lane E: as lane C using double concentration of glucose (4 g/L); lane F: as lane B with addition of hemin (final conc. 0.5 mg/L) with IPTG; lane G: as lane C with addition of hemin (final conc. 0.5 mg/L) with IPTG; lane H: Bio-Rad molecular mass standards.**

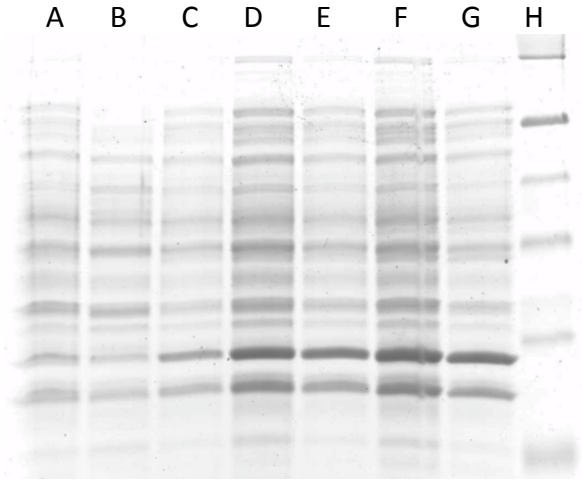

**Figure [3. 2]: Photo of perdeuterated C*c*P crystals.**

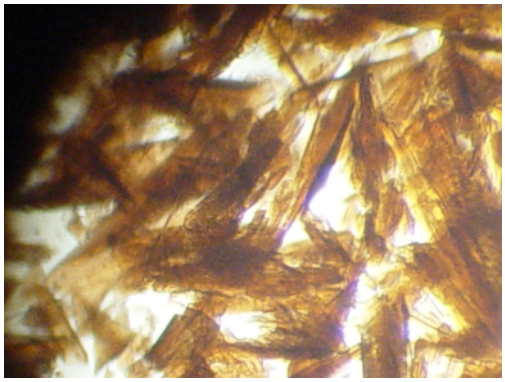

The optimised conditions, corresponding to lane G in Figure [3. 1], were provided to the D-Lab in Grenoble for the expression of the protein with deuterated carbon source. Nevertheless, crystals of perdeuterated C*c*P did not achieve the required size and shape (Figure [3. 2]) and could not be used. Instead, only deuterated crystals were used.

### 3.2.2. COMBINED X-RAY AND NEUTRON REFINEMENT METHODOLOGY

The room temperature C*c*P structure was solved using a joint method that complements neutron diffraction data with X-ray data. X-ray data provide very good positional information but are unable to place the hydrogen atoms. On the contrary, neutron data can provide this but the use of deuterated crystals causes the diffraction data to be partial, as the negative scattering length of the remaining hydrogen atoms cancels out the scattering of closely related atoms. Joint refinement strategy thus permits the full refinement of all the atoms of the structure, leading to an improved model. Combination of these data also increases the data-to-parameter ratio and reduces the influence of systematic errors as they are unlikely to be similar in the two types of data. For this purpose an X-ray structure of C*c*P at room temperature was also

solved but this is not discussed in the chapter and considered only for its use in the refinement of the neutron model. X-ray data collection and refinement are shown in Table [3. 1] whereas neutron data collection statistics are shown in Table [3. 2]. The joint X-ray/neutron refinement statistics are in Table [3. 3].

**Table [3. 1] X-ray data collection and refinement statistics. Values in parentheses are for the highest resolution shell.**

| **Diffraction Data** | **CcP Ferric Room Temperature** | **CcP ferric 100 K** | **APX ferric 100 K** |
|---|---|---|---|
| Number of crystals | 2 | 10 | 3 |
| Unit-cell parameters | $a$ = 51.6 Å, $b$ = 76.7 Å, $c$ = 107.1 Å, $\alpha$ = 90°, $\beta$ = 90°, $\gamma$ = 90° | $a$ = 51.12 Å, $b$ = 75.60 Å, $c$ = 106.75 Å $\alpha$ = 90°, $\beta$ = 90°, $\gamma$ = 90° | $a$ = 81.97 Å, $b$ = 81.97 Å, $c$ = 75.23 $\alpha$ = 90°, $\beta$ = 90°, $\gamma$ = 90° |
| Resolution (Å) | 43.90-2.01 (2.12-2.01) | 12.38-1.81 (1.90-1.81) | 57.97-1.90 (1.95-1.90) |
| Total observations | 78178 (10136) | 143623 (15551) | 146832 (10984) |
| Unique reflections | 26005 (3550) | 35815 (4816) | 36397 (2757) |
| $I/\sigma I$ | 18.7 (2.0) | 16.9 (9.6) | 16.78 (5.97) |
| $R_{merge}$ | 0.076 (0.671) | 0.056 (0.099) | 0.073 (0.294) |
| Completeness (%) | 90.5 (86.9) | 93.2 (87.7) | 94.2% (95.7%) |
| **Refinement** | | | |
| $R_{work}$ | 0.162 | 0.15 | 0.1372 |
| $R_{free}$ | 0.20 | 0.20 | 0.2328 |
| R.M.S.D | | | |
| Bonds (Å) | 0.017 | 0.045 | 0.019 |
| Angles | 1.523 (°) | 0.029 (Å) | 0.019 (Å) |

**Table [3. 2]: Neutron quasi-Laue data collection statistics for the two deuterated C*c*P crystals. Values in parentheses are for the highest resolution shell.**

| **Diffraction data** | |
|---|---|
| Neutron source, guide, instrument | Institut Laue-Langevin, Cold neutron guide H142, LADI-III |
| Wavelength (Å) | 3.2 – 4.18 |
| No. of images | 39 |
| Image width | Stationary |
| Setting spacing (°) | 14, 7 |
| Average exposure time (h) | 13 |
| Space group | $P2_12_12_1$ |
| Unit-cell parameters | $a$ = 51.6Å, $b$ = 76.7Å, $c$ = 107.1Å, $\alpha$ = 90°, $\beta$ = 90°, $\gamma$ = 90° |
| Resolution range (Å) | 53.53 – 2.40 (2.53 – 2.40) |
| No. of observations | 58913 (3361) |
| No. of unique reflections | 12903 (1358) |
| Completeness (%) | 76.3 (56.6) |
| $R_{merge}$ [#] | 0.168 (0.194) |
| $R_{p.i.m.}$(all $I^+$ and $I^-$) [§] | 0.065 (0.114) |
| Mean $I/\sigma(I)$ | 7.8 (5.0) |

**Table [3. 3]: Joint X-ray/neutron refinement statistics**

| **Refinement** | **Neutron** | **X-ray** |
|---|---|---|
| Resolution range (Å) | 53.55-2.40 (2.50-2.40) | 43.90-2.10 (2.17-2.10) |
| $R_{factor}$ (%) | 20.73 (31.60) | 16.63 (25.05) |
| $R_{free}$ (%) | 25.07 (36.87) | 20.33 (31.38) |
| No. of reflections | 12900 | 22900 |
| | **Model** | |
| $RMSD_{bonds}$ (Å) | 0.016 | |
| $RMSD_{angles}$ (°) | 1.651 | |
| Atoms | 5717 | |
| Solvent molecules | 205 | |
| Deuterium atoms | 862 | |
| Ramachandran plot | | |
| Favoured (%) | 98.6 | |
| Outliers (%) | 0.0 | |
| Rotamer outliers (%) | 5.0 | |

### 3.2.3. THE DISTAL HEME POCKET

#### *3.2.3.1. The distal histidine (His52)*

The nuclear scattering density of His52 shows that only the $N_\delta$ of the imidazole is deuterated and that this donates a hydrogen bond to $O_\delta$ of Asn82 (Figure [3. 3]-A and B). The $N_\varepsilon$ of His52 is around 2.90 Å from the oxygen of the water bound above the heme iron and is clearly unprotonated. The water, in turn, lies at 2.80 Å from the iron (W1 in Figure [3. 3]). The role of His52 was first suggested by Poulos and Kraut (*9*) and it was proposed to act first as a base, able to extract a proton from hydrogen peroxide allowing deprotonation and formation of a ferric heme-peroxide complex (Compound 0), and then as an acid (proton donor), leading to heterolytic cleavage of the peroxide with formation of Compound I and a water molecule. The absence of a hydrogen atom in our structure is clearly consistent with this original model (*9*). Also the hydrogen bond between the $O_\delta$ of Asn82 and the deuterated $N_\delta$ of His52 ($O_\delta$ - $N_\delta$ distance of 2.75 Å) is consistent with the idea that His-Asn hydrogen bonding modulates the reactivity (this effect is also referred to as the *pull* effect (10, 11)).

#### *3.2.3.2. The distal arginine (Arg48).*

The nuclear scattering density of Arg48 (Figure [3. 3]) indicates that the residue is flexible as it is observed in two different conformations. In both cases all the hydrogen atoms of the guanidium group are seen to have exchanged with deuterium. Flexibility of Arg48 of C*c*P has been previously observed in X-ray crystal structures and the two positions have been referred to as the "in" (when the side chain points towards the heme iron, Figure [3. 3]-C) and the "out" (when the side chain points towards the

**Figure [3. 3]: Structures and protonation states of the key residues of the distal heme region of CcP obtained by the room temperature joint X-ray/neutron study. The $2F_o - F_c$ nuclear scattering density map of the key residues is in blue (at 2.0 r.m.s.), whereas the deuterium OMIT map is in red (at 2.5 r.m.s.). Arg48 is represented: (A) as an overlapped structure of both the "in" and "out" orientations, (C) only in the "in" position and (D) only in the "out" position. The heme is in red. Waters and key residues are shown as sticks. Hydrogen and deuterium atoms are shown in white. Hydrogen bonds are shown as dashed lines.**

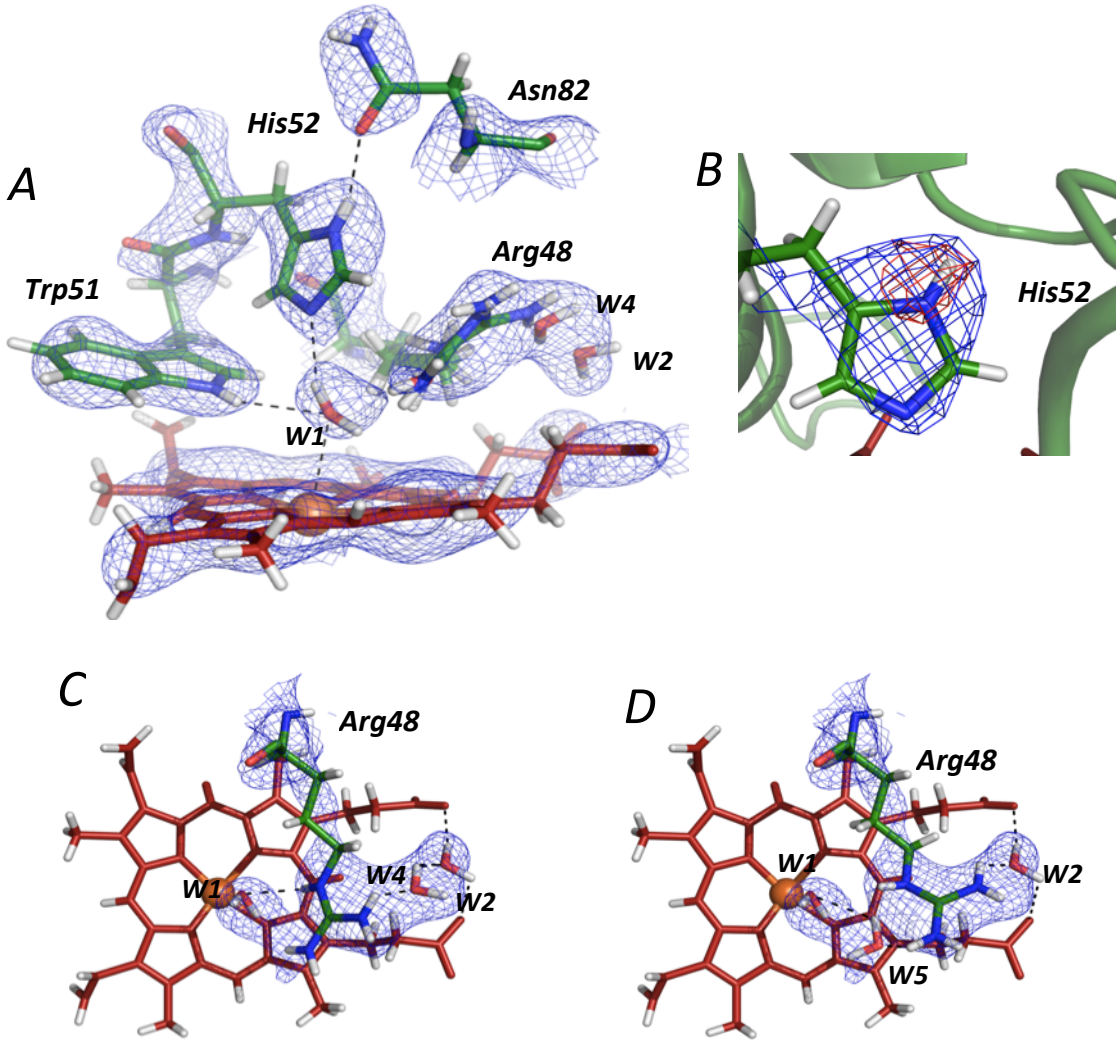


heme propionates Figure [3. 3]-D) (*1, 12*). As shown in Figure [3. 3], the shift of the arginine side chain causes the simultaneous switch of a water molecule from one side of the arginine side chain to the other (water W4 and W5 in Figure [3. 3]-C and D respectively). In both "in" and "out" positions the guanidium group of Arg48 is involved in hydrogen bonds: between $N_\eta 1$ and W4, $N_\varepsilon$ and W1 for the "in" position; $N_\eta 2$ and W5, $N_\eta 1$ and W2, $N_\varepsilon$ and W1 for the "out" position (see Figure [3. 3]-C and D respectively). It can be seen in Figure [3. 3] that the water molecule W2 also bridges

the heme propionates, which are themselves unprotonated. Therefore the shift of the Arg48 side chain is compensated for by the migration of the water molecules such that the hydrogen bond network linking the distal water molecule (W1) to the heme γ-edge is retained.

*3.2.3.3. The distal tryptophan (Trp51).*

The adjacent tryptophan (Trp51, Figure [3. 3]-A), once thought to be implicated in the stabilization of bound peroxide and Compound I (*13*), is deuterated on the indole nitrogen ($N_\varepsilon$). Although the geometry of the distal water molecule (W1, Figure [3. 3], whose position is determined solely from the nuclear density) is not precisely defined, a hydrogen bond between the Trp51 $N_\varepsilon$ and the distal water molecule can be identified, with the water oxygen and the indole nitrogen ($N_\varepsilon$) at a distance of 3.0 Å.

### 3.2.4. THE PROXIMAL HEME REGION

The proximal His-Asp-Trp triad has received considerable attention in C*c*P (*14-19*) and the joint X-ray/neutron structure for this region is shown in Figure [3. 4]. The $N_\varepsilon$ of His175 is not protonated and lies 2.0 Å away from the iron, whereas the $N_\delta$ of His175 is deuterated and is within hydrogen bond distance of the unprotonated $O_\delta 2$ of the charged acid group of Asp235. Likewise, the $O_\delta 1$ atom of Asp235 is unprotonated and at hydrogen bond distance with the deuterated $N_\varepsilon$ of Trp191, the site of the radical delocalisation of C*c*P Compound I (*20*). The hydrogen bonding network is consistent with the general idea that the buried charge of Asp235 helps to stabilise the cationic-indole Trp191 radical of Compound I and, at the same time, stabilises the oxy-ferryl

species through an inductive effect (also referred to as the *push* effect (*10*)) (*11, 14, 16, 17, 21, 22*).

**Figure [3. 4]: Structure and protonation states of the main residues of proximal heme region of CcP obtained by the room temperature joint X-ray/neutron study. The $2F_o- F_c$ nuclear scattering density map of the key residues is shown in blue (at 2.0 r.m.s.). Key residues (labelled) and water molecules are shown as sticks. The heme is in red, hydrogen and deuterium atoms are shown in white. Hydrogen bonds are shown as dashed lines.**

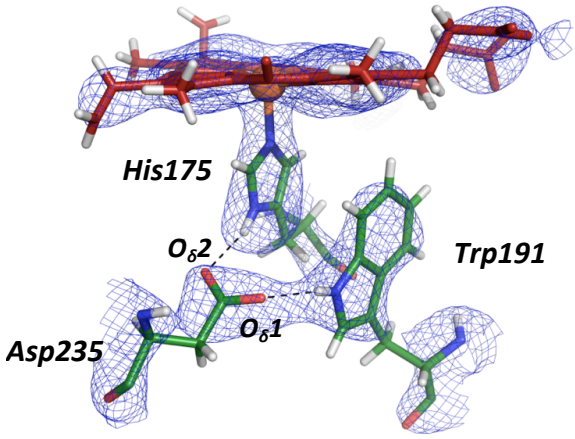


**Figure [3. 5]: A) Structure and protonation states of the main residues of the heme γ-edge region of CcP obtained by joint X-ray/neutron study (room temperature). B) Detail of the His181 showing the deuterium OMIT map (In red). $2F_o- F_c$ nuclear scattering density map of the key residues is shown in blue (at 2.0 r.m.s.) whereas the OMIT map is in red (at 1.5 r.m.s.). Key residues (labelled) and water molecules are shown as sticks. Heme and Arg48 are in silver. Hydrogen and deuterium atoms are shown in white. Hydrogen bonds are shown as dashed lines. Density of W2 has been omitted for clarity.**

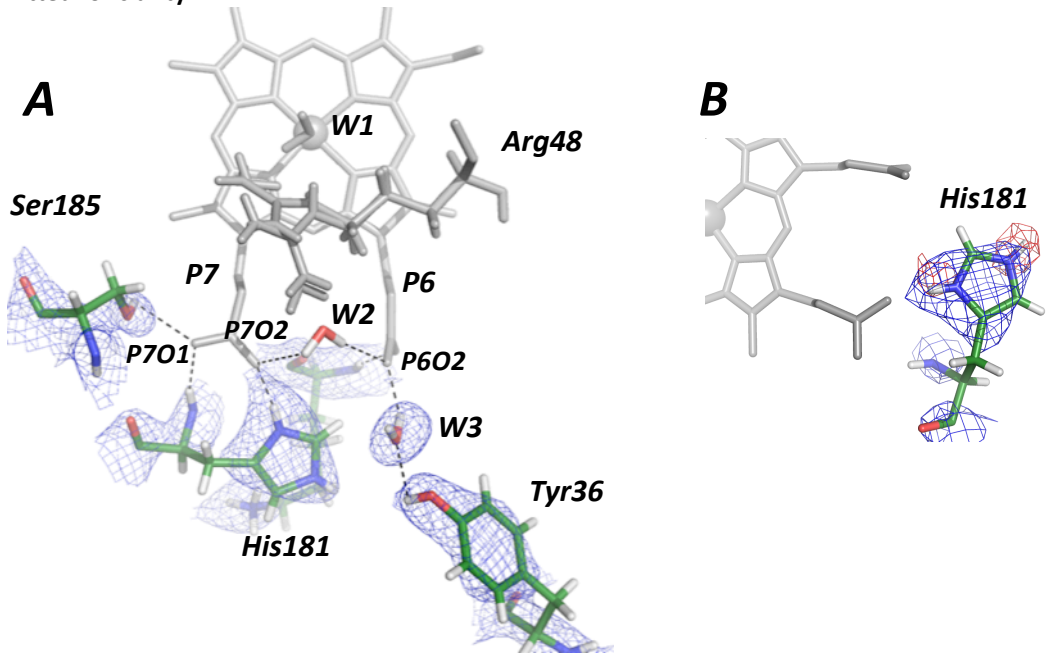

### 3.2.5. THE HEME PROPIONATES AND THE γ-HEME EDGE

The heme propionates have been implicated in the electron pathway that allows the electrons to move from substrates bound at the heme γ-edge to the oxy-ferryl species (Compound I and Compound II) during turnover (*23-25*). As indicated above, both the propionates appear as unprotonated species (Figure [3. 3] and Figure [3. 5]) and are involved in interactions with the protein and ordered water molecules. The heme 7-propionate forms two hydrogen bonds with His181, one involving the propionate O2 (P7O2, Figure [3. 5]) and the deuterated $N_\delta$ of the histidine, and one involving the propionate O1 (P7O1, Figure [3. 5]) and the amide backbone of this histidine. The O1 of the heme 7-propionate (P7O1, Figure [3. 5]) is also close to the side chain of Ser185 and the O2 (P7O2, Figure [3. 5]) is at hydrogen bond distance with the water molecule bridging the heme propionates (W2, Figure [3. 5]), although in both cases the geometry is poor for hydrogen bond formation. Finally, one oxygen atom of the heme 6-propionate (P6O2 Figure [3. 5]) is an acceptor for a hydrogen bond with the backbone nitrogen amide of Lys179, whilst the other oxygen (P6O1 Figure [3. 5]) interacts with the water molecule bridging the heme propionates (W2, Figure [3. 5]). W2 also lies at hydrogen bond distance to either the mobile guanidinium of Arg48 (*26*) or W4, depending on the Arg48 side chain position (Figure [3. 3]-C and D respectively).

### 3.2.6. THE SUBSTRATE BINDING SITE

The crystal structure of the complex between C*c*P and cytochrome *c* (*27*) indicated Glu290, Asp34, Glu35 and Asp37 as the crucial residues for the formation of

the complex between C*c*P and its physiological substrate, cytochrome *c*. This model was supported by other work (*28-31*). All the carboxylic groups of these side chain acids are unprotonated as shown in Figure [3. 6] and this is consistent with these residues acting as hydrogen bond acceptors upon formation of C*c*P-cytochrome *c* complex. The side chain of Glu290 binds a water molecule (W9, Figure [3. 6]) and it is possible that the hydroxyl group of the side chain of Ser246 binds to a symmetry related water molecule (not shown). One oxygen atom of the Asp34 side chain is within hydrogen bonding distance of the NH group of the backbone of Thr2, while Asp35 seems to have no important interactions. Finally, one of the oxygen atoms of the carboxylic group of Asp37 faces the bulk solvent of the protein and forms a hydrogen bond with a water molecule (W6 in Figure [3. 6]) while the second oxygen atom seems not directly involved in any specific interaction. The weak density surrounding the side chain of Asp34 and Asp35, however suggests that these might be unconstrained and therefore assume multiple conformations.

**Figure [3. 6]: Structure and protonation states of the residues involved in the primary binding between C*c*P and cytochrome *c*, obtained by joint X-ray/neutron study. $2F_o$-$F_c$ nuclear scattering density map is in blue (at 2.0 r.m.s.). Key residues and water molecules (sticks) are labelled. The heme and Tyr36 are in silver while hydrogen and deuterium atoms are shown in white. Hydrogen bonds are indicated as dashed lines.**

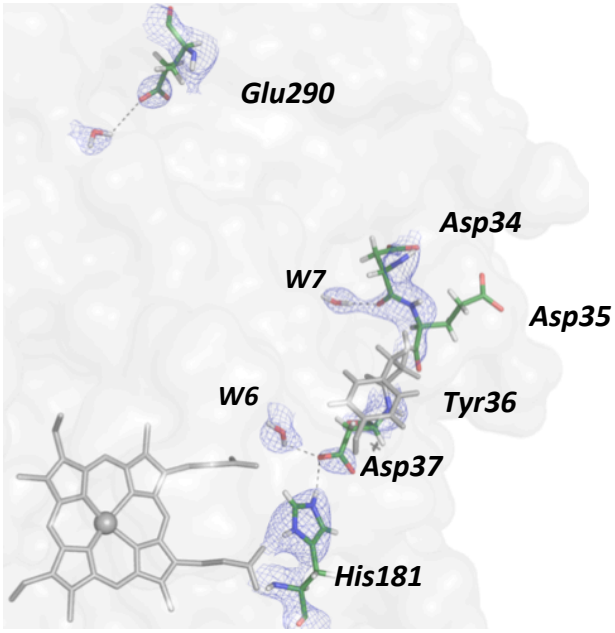

### 3.2.7. THE X-RAY STRUCTURE OF FERRIC C*c*P AT 100 K

The nuclear scattering density map indicates that the distal water molecule (W1 Figure [3. 3]) lies at about 2.8 Å from the iron. However, previously reported X-ray C*c*P structures at 100 K present a shorter distance (2.40 Å and 2.33 Å for 2CYP (*32*) and 1ZBY (*12*), respectively). Therefore, in order to understand the reason for this difference and possibly solve the effect of photoreduction and low temperature, a 1.8 Å C*c*P X-ray structure, obtained by a multi-crystal method (whereby the dose absorbed by each crystal is limited 0.003 MGy to prevent photoreduction) at 100 K is presented (data collection and refinement statistics are presented in Figure [3. 7]). This shows a high overall agreement with the room temperature joint X-ray/neutron structure, with a root-mean-square deviation (calculated on the C$\alpha$ of residues 2-294 (*33*)) of 0.226 Å. In Figure [3. 7] the structure of the heme distal side is shown in the unreduced 100 K structure. Interestingly, the distal water molecule (W1, Figure [3. 7]) is closely coordinated to the iron, with an Fe-O distance of 1.96 Å. The ESUs calculated by inversion of the full normal matrix (*34*), are 0.08 Å and 0.02 Å for the oxygen and the iron atoms respectively. Such a change is consistent with the reported alteration in spectroscopic signature observed upon cooling, which is attributed to a change of the coordination of the iron from a high spin 6- or 5-coordinate system at room temperature to a low spin 6-coordinate system at 100 K (*18, 35-37*). Notably the Fe-O distance in the unreduced 100 K structure determined here is shorter than previously reported in earlier X-ray C*c*P structures at 100 K (2.40 Å and 2.33 Å for 2CYP (*32*) and 1ZBY (*12*)), in which the oxidation state of the iron has probably been reduced from the ferric state to the ferrous by X-ray exposure (*4*).

**Figure [3. 7]: X-ray structure of the heme distal region of ferric CcP, obtained at 100 K by X-ray crystallography, using a multi-crystal approach. The measured oxygen-iron distance is 1.93 Å. Electron scattering density map is in green (at 2.0 r.m.s.). Key residues (labelled) and water molecules are shown as sticks and spheres, respectively, and the heme is in red.**

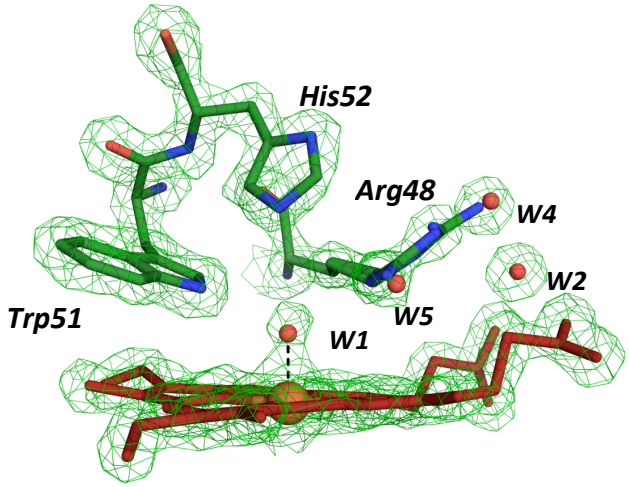


**Figure [3. 8]: X-ray structure of the heme distal region of ferric APX, obtained at 100 K by X-ray crystallography, using a multi-crystal approach. The measured oxygen-iron distance is 1.91 Å. Electron scattering density map is in green (at 2.0 r.m.s.). Key residues (labelled) and water molecules are shown as sticks and spheres, respectively, and the heme is in red.**

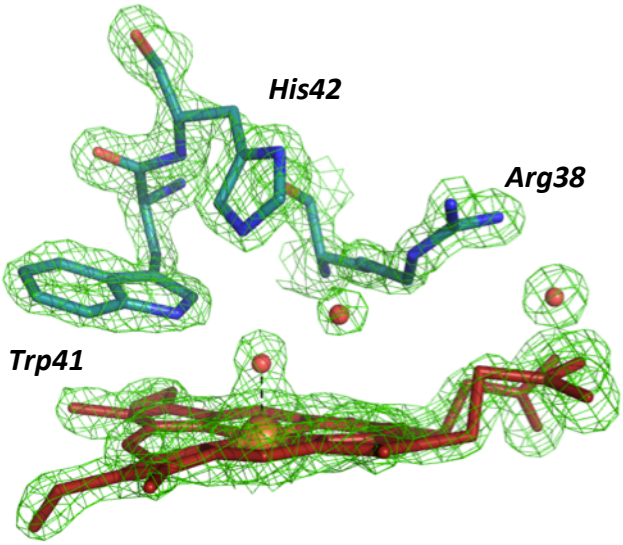

### 3.2.8. THE X-RAY STRUCTURE OF FERRIC APX AND AT 100 K

Spectroscopic data (*38*) indicate that heme in APX undergoes a similar change of coordination upon freezing to cryogenic conditions, moving from a 5- or 6- high spin system to a 6-coordinate low spin species. However, published X-ray structures indicate a distance between Fe and distal water molecule that ranges from 1.95 Å to 2.10 Å (see pdb entries 1OAG and 1OAF respectively (*23*)). In order to understand whether these structures were likewise affected by photoreduction, the X-ray structure of ferric APX at 100 K, using a multicrystal methodology, is also presented and is shown in Figure [3. 8]. The Fe-O distance is 1.91 Å and the positional ESUs, calculated by inversion of the full normal matrix (*34*) is 0.09 Å and 0.02 Å for O and Fe respectively.

## 3.3. DISCUSSION

### 3.3.1. HYDROGEN BOND NETWORK

The joint X-ray/neutron structure, unveiling for the first time the protonation states C*c*P residues, allows for the crystallographic determination of the hydrogen bond networks which control the reactivity of the enzyme. First of all, data show two networks, found below and above the heme plain respectively, which are consistent with previous hypothesis and seem to be the source of an inductive effect that entails the heme and helps to form and stabilise Compound I and Compound II (often referred to as the *push-pull* effect (*11*)). Also the data show another important hydrogen bond network that links together the distal water molecule (W1 in Figure [3. 3]), the Arg48 side chain, the heme propionates and finally the side chain of the Tyr36 (Figure [3. 5]). This network seems to be conserved regardless of the conformation of the Arg48, as the flip in position of this side chain is compensated for by the water, which occupies the corresponding resultant space (Figure [3. 3]). In this way, the distal water molecule (W1 Figure [3. 3]) is always linked to the Arg48 (either directly or through a water molecule, Figure [3. 3]) and similarly, the latter is always linked to the water molecule bridging the heme propionates (W2 Figure [3. 5]). Finally, W2 forms a hydrogen bond with the 6-propionate group (labelled P6, Figure [3. 5]), which, in turn, accepts a hydrogen bond from the water that bridges it to the side chain of Tyr36 (W3 Figure [3. 5]). Beyond this residue, the complexity of the protein does not allow for any further unambiguous interpretation and several structurally equivalent hydrogen bond networks can be proposed. By comparison with APX (*23*) and MnP (*39*) (Figure [3. 9]), it is clear that an equivalent hydrogen bond network model can exist in these heme

peroxidases. The position occupied by the last water molecule described in this model for CcP (W3, Figure [3. 9]-A) is replaced by one of the oxy-ligands of the Mn ion in MnP (Figure [3. 9]-B) or by the ascorbate C2 hydroxyl group in the APX-ascorbate complex (Figure [3. 9]-C). Although the 6-propionate is thought to be part of the electron pathway from the substrate to the heme during turnover in APX (*23, 24*), the networks of hydrogen bonds here suggest that the heme γ-edge could also be involved in proton transfer to the heme. Given the highly conserved structures, this might be a more general mechanism for proton delivery across other heme peroxidases.

**Figure [3. 9]: Comparison of the structures of the heme distal regions of (A) CcP (green), (B) Mn-peroxidase (blue) and (C) APX-ascorbate complex (yellow). The key residues are labelled and the heme is shown in red sticks.**

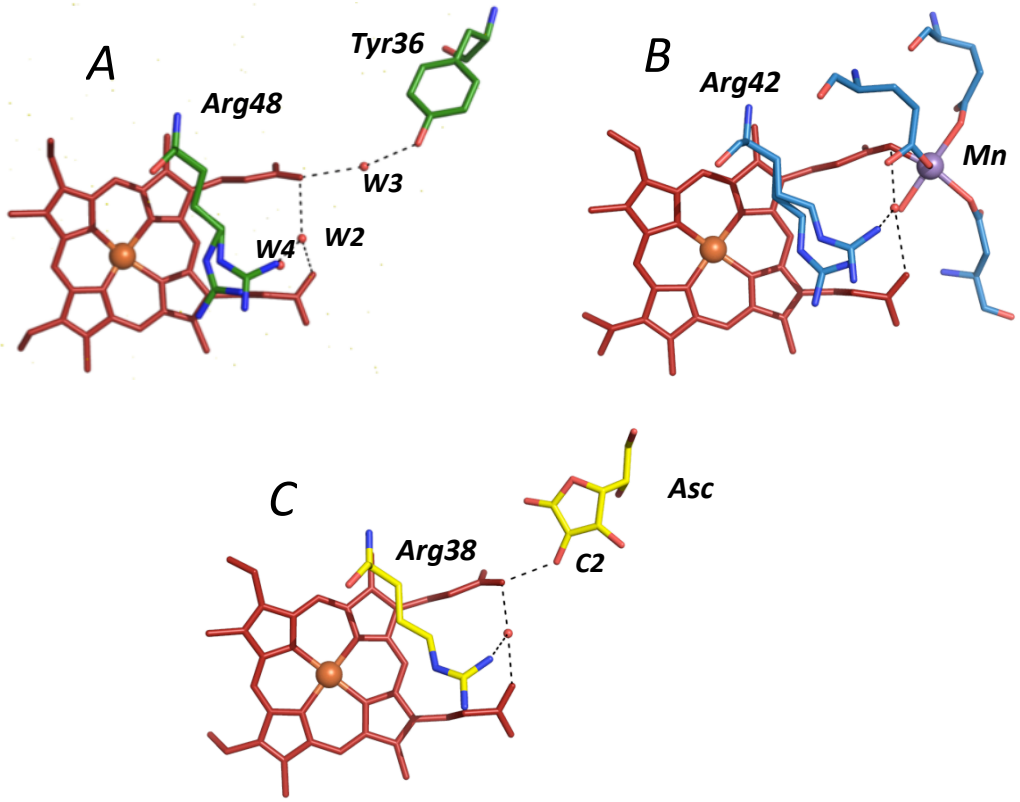

### 3.3.2. COMPARISON BETWEEN ROOM TEMPERATURE JOINT X-RAY/NEUTRON STRUCTURE AND THE MULTI-CRYSTAL STRUCTURE OF FERRIC C*c*P AND APX AT 100 K.

The reported position of the water bound at the distal position (W1 Figure [3. 3]) varies considerably in the literature. This may be due to partial or full reduction of the ferric heme through the photoelectric effect (*1*) or due to the alteration in spin state under cryogenic conditions (proposed on the basis of spectroscopic observations (*18, 35, 36*)). To resolve this, a structure of C*c*P and APX at 100 K was determined, using a multicrystal approach in order to rule out the effects of photoreduction (Figure [3. 7] and Figure [3. 8] respectively). These structures clearly show coordination between the iron and the distal water molecule and suggest that upon cryo-vitrification the heme coordination changes to a 6-coordinate species. By comparison with previously published structures ((*12, 32*) for C*c*P and (*23*) for APX), it is clear that photoreduction is likely to have occurred in these structures, especially for C*c*P, and, as a consequence, the coordination of the heme has been altered. Therefore, the room temperature joint X-ray/neutron structure presented here describes the first authentic ferric structure of C*c*P, representative of the protein in its native, catalytically active ferric state.

## 3.4. SUMMARY

The joint use of X-ray and neutron crystallography has allowed the determination of the protonation states of the residues of C*c*P. From the protonation states, the hydrogen bond networks that entail the key residues have been determined. Precisely, a first hydrogen bond network can be found above the heme plain (Figure [3. 3]-A) and it bridges the side chains of His52 and Asn82, whereas a second network links together the side chains of His175, Trp191 and Asp235, below the heme plain (Figure [3. 5]). The coordination of the residues shown by the study is consistent with the hypothesis that an inductive effect (often referred to as the *push-pull* effect) is generated, which on one side (through the His52) helps to activate the hydrogen peroxide by deprotonation, and on the other side (through the His175) helps to stabilise the ferryl intermediates during the reaction.

Another important hydrogen bond links together the distal water molecule (W1 Figure [3. 3]), the Arg48, the heme propionates and the Tyr36 (beyond the heme γ-edge), and also involves a few other water molecules (see Figure [3. 3]-C and D, and Figure [3. 5]). The position and the extent of this network are consistent with the idea that this could be part of the proton delivery pathway that provides protons to the oxy-ferryl ion during turnover. This hypothesis is also supported by the observation that the same pathway can be found in other heme peroxidases and that the substrate binding site is often found around the heme γ-edge region (Figure [3. 9]).

Finally comparison of the neutron structure, obtained at room temperature, with the X-ray structure at 100 K (obtained by means of a multicrystal method) for ferric C*c*P and APX has indicated that upon cryo-vitrification, the distal water coordinates to

the heme. The Fe-O distance observed in these structure is 1.96 Å and 1.91 Å for C*c*P and APX, respectively, consistent with formation of ferric hydroxyl low spin species ($Fe^{III}$-OH).

## References


1. Gumiero, A., Metcalfe, C. L., Pearson, A. R., Raven, E. L., and Moody, P. C. E. (2011) Nature of the Ferryl Heme in Compounds I and II, *Journal of Biological Chemistry 286*, 1260-1268.
2. Howard, E. I., Sanishvili, R., Cachau, R. E., Mitschler, A., Chevrier, B., Barth, P., Lamour, V., Van Zandt, M., Sibley, E., Bon, C., Moras, D., Schneider, T. R., Joachimiak, A., and Podjarny, A. (2004) Ultrahigh resolution drug design I: details of interactions in human aldose reductase-inhibitor complex at 0.66 A, *Proteins 55*, 792-804.
3. Blakeley, M. P. (2009) Neutron macromolecular crystallography, *Crystallography Reviews 15*, 157 - 218.
4. Berglund, G. I., Carlsson, G. H., Smith, A. T., Szoke, H., Henriksen, A., and Hajdu, J. (2002) The catalytic pathway of horseradish peroxidase at high resolution, *Nature 417*, 463-468.
5. Fulop, V., Phizackerley, R. P., Soltis, S. M., Clifton, I. J., Wakatsuki, S., Erman, J., Hajdu, J., and Edwards, S. L. (1994) Laue diffraction study on the structure of cytochrome c peroxidase compound I, *Structure 2*, 201-208.
6. Blakeley, M. P., Langan, P., Niimura, N., and Podjarny, A. (2008) Neutron crystallography: opportunities, challenges, and limitations, *Curr Opin Struct Biol 18*, 593-600.
7. Petit-Haertlein, I., Blakeley, M. P., Howard, E., Hazemann, I., Mitschler, A., Podjarny, A., and Haertlein, M. (2010) Incorporation of methyl-protonated valine and leucine residues into deuterated ocean pout type III antifreeze protein: expression, crystallization and preliminary neutron diffraction studies, *Acta Crystallographica Section F 66*, 665-669.
8. Brunger, A. T. (2007) Version 1.2 of the Crystallography and NMR system, *Nat Protoc 2*, 2728-2733.
9. Poulos, T. L., Freer, S. T., Alden, R. A., Edwards, S. L., Skogland, U., Takio, K., Eriksson, B., Xuong, N., Yonetani, T., and Kraut, J. (1980) The crystal structure of cytochrome c peroxidase, *J Biol Chem 255*, 575-580.
10. Poulos, T. L., and Kraut, J. (1980) The stereochemistry of peroxidase catalysis, *J Biol Chem 255*, 8199-8205.
11. Nonaka, D., Wariishi, H., Welinder, K. G., and Fujii, H. (2010) Paramagnetic 13C and 15N NMR analyses of the push and pull effects in cytochrome c peroxidase and Coprinus cinereus peroxidase variants: functional roles of highly conserved amino acids around heme, *Biochemistry 49*, 49-57.
12. Bonagura, C. A., Bhaskar, B., Shimizu, H., Li, H., Sundaramoorthy, M., McRee, D. E., Goodin, D. B., and Poulos, T. L. (2003) High-resolution crystal structures and spectroscopy of native and compound I cytochrome c peroxidase, *Biochemistry 42*, 5600-5608.
13. Miller, M. A., Shaw, A., and Kraut, J. (1994) 2.2 A structure of oxy-peroxidase as a model for the transient enzyme: peroxide complex, *Nat Struct Biol 1*, 524-531.
14. Satterlee, J. D., Erman, J. E., Mauro, J. M., and Kraut, J. (1990) Comparative proton NMR analysis of wild-type cytochrome c peroxidase from yeast, the recombinant enzyme from Escherichia coli, and an Asp-235----Asn-235 mutant, *Biochemistry 29*, 8797-8804.

15. Smulevich, G., Wang, Y., Mauro, J. M., Wang, J., Fishel, L. A., Kraut, J., and Spiro, T. G. (1990) Single-crystal resonance Raman spectroscopy of site-directed mutants of cytochrome c peroxidase, *Biochemistry 29*, 7174-7180.
16. Ferrer, J. C., Turano, P., Banci, L., Bertini, I., Morris, I. K., Smith, K. M., Smith, M., and Mauk, A. G. (1994) Active site coordination chemistry of the cytochrome c peroxidase Asp235Ala variant: spectroscopic and functional characterization, *Biochemistry 33*, 7819-7829.
17. Goodin, D. B., and McRee, D. E. (1993) The Asp-His-Fe triad of cytochrome c peroxidase controls the reduction potential, electronic structure, and coupling of the tryptophan free radical to the heme, *Biochemistry 32*, 3313-3324.
18. Smulevich, G., Mantini, A. R., English, A. M., and Mauro, J. M. (1989) Effects of temperature and glycerol on the resonance Raman spectra of cytochrome c peroxidase and selected mutants, *Biochemistry 28*, 5058-5064.
19. Smulevich, G., Mauro, J. M., Fishel, L. A., English, A. M., Kraut, J., and Spiro, T. G. (1988) Heme pocket interactions in cytochrome c peroxidase studied by site-directed mutagenesis and resonance Raman spectroscopy, *Biochemistry 27*, 5477-5485.
20. Sivaraja, M., Goodin, D. B., Smith, M., and Hoffman, B. M. (1989) Identification by ENDOR of Trp191 as the free-radical site in cytochrome c peroxidase compound ES, *Science 245*, 738-740.
21. Dasgupta, S., Rousseau, D. L., Anni, H., and Yonetani, T. (1989) Structural characterization of cytochrome c peroxidase by resonance Raman scattering, *J Biol Chem 264*, 654-662.
22. Vitello, L. B., Erman, J. E., Miller, M. A., Mauro, J. M., and Kraut, J. (1992) Effect of Asp-235-->Asn substitution on the absorption spectrum and hydrogen peroxide reactivity of cytochrome c peroxidase, *Biochemistry 31*, 11524-11535.
23. Sharp, K. H., Mewies, M., Moody, P. C., and Raven, E. L. (2003) Crystal structure of the ascorbate peroxidase-ascorbate complex, *Nat Struct Biol 10*, 303-307.
24. Guallar, V. (2008) Heme electron transfer in peroxidases: the propionate e-pathway, *J Phys Chem B 112*, 13460-13464.
25. Poulos, T. L. (2007) The Janus nature of heme, *Nat Prod Rep 24*, 504-510.
26. Metcalfe, C., Macdonald, I. K., Murphy, E. J., Brown, K. A., Raven, E. L., and Moody, P. C. (2008) The tuberculosis prodrug isoniazid bound to activating peroxidases, *J Biol Chem 283*, 6193-6200.
27. Pelletier, H., and Kraut, J. (1992) Crystal structure of a complex between electron transfer partners, cytochrome c peroxidase and cytochrome c, *Science 258*, 1748-1755.
28. Leesch, V. W., Bujons, J., Mauk, A. G., and Hoffman, B. M. (2000) Cytochrome c Peroxidase,àíCytochrome c Complex: Locating the Second Binding Domain on Cytochrome c Peroxidase with Site-Directed Mutagenesis,Ä†, *Biochemistry 39*, 10132-10139.
29. Mauk, M. R., Ferrer, J. C., and Mauk, A. G. (1994) Proton linkage in formation of the cytochrome c-cytochrome c peroxidase complex: electrostatic properties of the high- and low-affinity cytochrome binding sites on the peroxidase, *Biochemistry 33*, 12609-12614.

30. Zhou, J. S., and Hoffman, B. M. (1994) Stern-volmer in reverse: 2:1 stoichiometry of the cytochrome c-cytochrome c peroxidase electron-transfer complex, *Science 265*, 1693-1696.
31. Zhou, J. S., Tran, S. T., McLendon, G., and Hoffman, B. M. (1997) Photoinduced electron transfer between cytochrome c peroxidase (D37K) and Zn-substituted cytochrome c: Probing the two-domain binding and reactivity of the peroxidase, *Journal of the American Chemical Society 119*, 269-277.
32. Finzel, B. C., Poulos, T. L., and Kraut, J. (1984) Crystal structure of yeast cytochrome c peroxidase refined at 1.7-A resolution, *J Biol Chem 259*, 13027-13036.
33. Adams, P. D., Afonine, P. V., Bunkoczi, G., Chen, V. B., Davis, I. W., Echols, N., Headd, J. J., Hung, L.-W., Kapral, G. J., Grosse-Kunstleve, R. W., McCoy, A. J., Moriarty, N. W., Oeffner, R., Read, R. J., Richardson, D. C., Richardson, J. S., Terwilliger, T. C., and Zwart, P. H. (2010) PHENIX: a comprehensive Python-based system for macromolecular structure solution, *Acta Crystallographica Section D 66*, 213-221.
34. Sheldrick, G. (2008) A short history of SHELX, *Acta Crystallographica Section A 64*, 112-122.
35. Evangelista-Kirkup, R., Crisanti, M., Poulos, T. L., and Spiro, T. G. (1985) Resonance Raman spectroscopy shows different temperature-dependent coordination equilibria for native horseradish and cytochrome c peroxidase, *FEBS Lett 190*, 221-226.
36. Yonetani, T., and Anni, H. (1987) Yeast cytochrome c peroxidase. Coordination and spin states of heme prosthetic group, *J Biol Chem 262*, 9547-9554.
37. Turano, P., Ferrer, J. C., Cheesman, M. R., Thomson, A. J., Banci, L., Bertini, I., and Mauk, A. G. (1995) pH, electrolyte, and substrate-linked variation in active site structure of the Trp51Ala variant of cytochrome c peroxidase, *Biochemistry 34*, 13895-13905.
38. Jones, D. K., Dalton, D. A., Rosell, F. I., and Raven, E. L. (1998) Class I heme peroxidases: characterization of soybean ascorbate peroxidase, *Arch Biochem Biophys 360*, 173-178.
39. Sundaramoorthy, M., Gold, M. H., and Poulos, T. L. (2010) Ultrahigh (0.93A) resolution structure of manganese peroxidase from Phanerochaete chrysosporium: Implications for the catalytic mechanism, *J Inorg Biochem*.

Chapter 4

# CONCLUSIONS

## 4.1. CONSEQUENCES FOR THE REACTION MECHANISM OF HEME PEROXIDASES

In this thesis, new structures for two heme peroxidases are presented (Table [4. 1]). The new information provided about the ferryl intermediates (presented in Chapter 2) and the insights gained about the ferric structure of C*c*P (presented in Chapter 3) form a complete set of data that allows analysis of the reaction mechanism of heme peroxidases. This new overall view, presented in Scheme [4. 1], provides important insights that clarify mechanistic aspects which have been confused up until now.

**Table [4. 1]: Summary of all the structures presented in this thesis with the corresponding figure number.**

| Structures | Protein | |
|---|---|---|
| | C*c*P | APX |
| Ferric enzyme at RT | Figs. [3. 3] – [3. 6] | - |
| Ferric enzyme at 100 K | Fig [3. 7] | Fig. [3. 8] |
| Compound III | - | Fig. [2. 5] |
| Compound I | Fig. [2. 1]-A | Fig. [2. 1]-B |
| Compound II | Fig. [2. 2]-A | Fig. [2. 2]-B |
| Ferrous enzyme | Fig. [2. 8]-A | Fig. [2. 8]-B |

### 4.1.1. THE STRUCTURE OF FERRIC ENZYME

Panel A of Scheme [4. 1] reports on the structure of the ferric enzyme at room temperature. First of all, on the basis of the nuclear scattering density map of ferric C*c*P at room temperature (see Chapter 3), the distal water molecule is not tightly

coordinated to the heme and lies at a distance of about 2.8 Å from the iron. This is consistent with spectroscopic data indicating that ferric C*c*P, at room temperature, mainly exists as a high-spin species (*1*), 5 or 6 coordinate (depending on the conditions and aging). Upon freezing the water molecule coordinates to the heme and a 6-coordinate low spin species is formed. Furthermore, this change in coordination is likely to be of general validity as similar effects are also observed for APX (*2*) (Figure [3. 8]). The nuclear scattering density map shows that in resting C*c*P the $N_{\varepsilon}$ of Trp51, $N_{\delta}$ of His52 and the guanidium group of Arg48 are protonated and the protons are exchangeable (shown is cyan in panel A).

### 4.1.2. REACTION WITH HYDROGEN PEROXIDE: FROM COMPOUND 0 TO COMPOUND I

In step (i) reaction of the ferric enzyme with peroxide leads to the transient Compound 0 (ferric-hydroperoxy) species. Although Compound 0 is not stable enough to be characterised either structurally or spectroscopically, it is considered to be structurally equivalent to a ferrous-oxy (Compound III) species, whose structure has been obtained in this work for APX (Figure [2. 5]), and in previous works for HRP and C*c*P (*3, 4*). A model for this is shown in panel B. The joint X-ray/neutron structure (Chapter 3) confirms that the $N_{\varepsilon}$ of the distal histidine (His52) is unprotonated in the resting state and thus acts as an active site base which first accepts a proton and allows Compound 0 to be formed by deprotonation of hydrogen peroxide, and successively releases the proton to induce heterolytic cleavage of hydrogen peroxide and formation of Compound I (step (ii) Scheme [4. 1]). A recent theoretical model (*5*) has shown that the distal histidine is not likely to

extract the hydrogen atom directly from hydrogen peroxide, as originally proposed (*6*), but a water molecule mediates the process.

### 4.1.3. STRUCTURAL CHARACTERISATION OF COMPOUND I

The structural analysis reported in Chapter 2 indicates that Compound I of C*c*P and APX is characterised by an oxy-ferryl species with an unprotonated oxygen. The corresponding model is shown in panel C. The same analysis also indicates that upon formation of Compound I, the flexible distal arginine is only found in the "in" conformation, and the $N_{\varepsilon}$ of the guanidium group forms a hydrogen bond with the ferryl oxygen.

### 4.1.4. REDUCTION OF COMPOUND I AND FORMATION OF COMPOUND II

Reduction of Compound I to Compound II leads to an increase of the Fe-O bond distance (up to 1.83 Å for C*c*P and 1.84 Å for APX, shown in Chapter 2) that is consistent with protonation of the ferryl oxygen. A model for this species is presented in panel D. The structural analysis reported in Chapter 2 seems also to suggest that upon formation of Compound II the flexibility of the distal arginine increases. The two events (protonation of the oxygen and increase of flexibility of distal arginine), occurring simultaneously, could be consistent with the idea that the distal arginine provides the proton to the oxy-ferryl species. However the $pK_a$ of the guanidium group of the arginine (about 12.5) does not allow formation of a stable deprotonated intermediate and most likely the proton is delivered through a concerted mechanism by which the arginine releases the proton to the oxy-ferryl species and, at the same time, takes a proton up from one of the surrounding water

molecules. In this way no formal change in protonation state of the guanidium group occurs during turnover.

Compound II is stabilised by formation of a series of hydrogen bonds. However, the geometry is not fixed as the Fe-OH bond (consistent with a single bond) can rotate around its axis and it is possible that these hydrogen bonds change with the orientation of the O-H bound. Furthermore, not only do the distal residues (formally the tryptophan and the arginine) participate in these hydrogen bonds, but the network also involves a few water molecules surrounding the ferryl species (not shown).

#### 4.1.5. REDUCTION OF COMPOUND II: THE LAST STEP OF THE CYCLE

Finally, reduction of Compound II leads to formation of ferric enzyme again (step iv). During this process a second hydrogen atom is delivered to the ferryl oxygen. However, given the complexity and the number of possible conformations, it is not possible to infer any preferred pathway and the delivery can occur from the arginine as well as from one of the adjacent water molecules.

The data reported here offer, for the first time, a detailed picture of the reaction mechanism of heme peroxidases and, fulfilling all the gaps previously left in the literature on the nature of the reaction intermediates and on the hydrogen bond networks, they also provide new insights and evidences suggesting models for understanding aspects such as the proton delivery pathway, which has never been studied before.

**Scheme [4. 1]: Schematic representation of the revised reaction mechanism of heme peroxidases. Schematic representation of the heme peroxidase reaction pathway and possible protonation events based on the joint X-ray/neutron structure of ferric CcP here presented and on the structures of heme oxy-intermediates (Compound III, Compound I and Compound II) previously published. The ferric enzyme (resting state) is shown on the basis of the joint X-ray and neutron study and the observed exchangeable hydrogen atoms (as indicated by the nuclear scattering density) are in cyan. The structure of the transient Compound 0 is based on that of Compound III, whereas the structure of Compound I and Compound II shown uses those previously published. The positions of the corresponding hydrogen atoms for Compound 0, Compound I and Compound II are assumed from the ferric neutron structure and shown in white. Refer to text for further details. Heme is in red; nitrogen atoms are in blue and carbon atoms in black.**

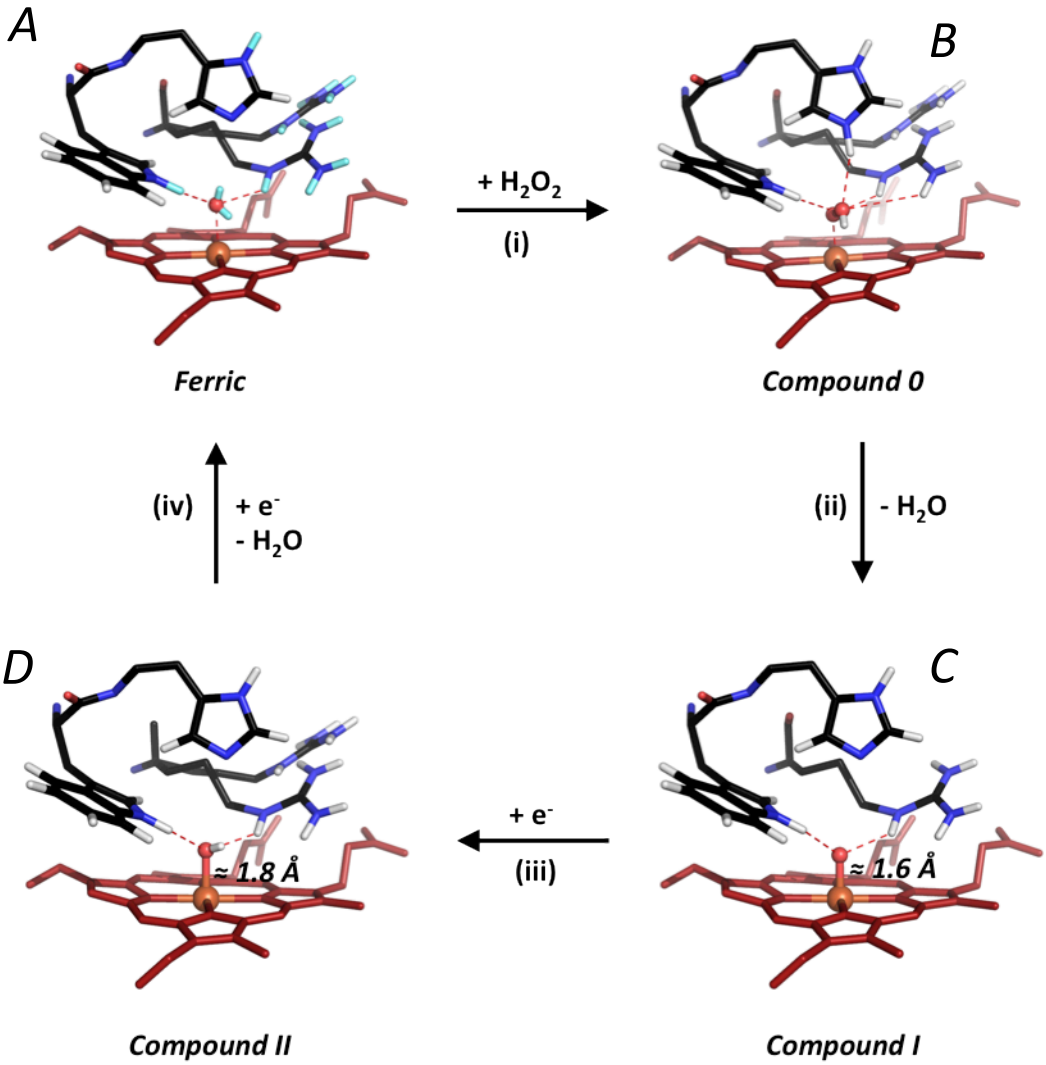

## 4.2. CONSEQUENCES FOR THE SUPERFAMILY OF HEME ENZYMES: A MODEL FOR COMPOUND I OF GENERAL VALIDITY

As mentioned in Chapter 1, some of the steps of the reaction mechanism of heme peroxidases are also conserved across the superfamily of oxygen-activator heme enzymes (*7*). Amongst all, formation of Compound I is the most important as this intermediate is the oxidising species in enzymes such as the cytochromes P450 or NOS.

Isolation of Compound I of cytochrome P450 has proved a very hard task, given the elusive nature of this species in both physiological and non-physiological conditions, and so far, only spectroscopic and kinetic analysis have been performed. Although no structural data are available yet, recent data (*8*) seem to demonstrate that Compound I of cytochrome P450 is an unprotonated oxy-ferryl species which, for many aspects, resembles that of CPO and is consistent with a $Fe^{IV}$=O structure. The most accredited P450 reaction model (the *re-bound* model (*9*)) proposes that the oxygen atom of Compound I reacts directly with the substrate and, through oxidation of a carbon atom of the hydrocarbon chain of the substrate, yields the hydroxylated product. The step-by-step mechanism of the oxidation, though, is not yet completely established. Recent studies (*8*) seem to support the idea that the oxygen of Compound I extracts a hydrogen atom from the substrate, leaving an unstable and oxidised carbon atom (likely a radical). This, in turn, immediately reacts with the just formed hydroxyl group thus to generate a C-OH bond and produce the hydroxylated product. The unprotonated state of the oxy-ferryl species of Compound I, as determined for APX and C*c*P in this thesis, is consistent with the

proposed model of Compound I for cytochrome P450. Moreover, the observation that the ferryl oxygen in Compound II is protonated suggests that extraction of a hydrogen atom from the substrate by Compound I of cytochrome P450 to form a hydroxy-ferryl species (only transiently in a P450-like reaction cycle) is formally possible, supporting thus the P450 *re-bound* reaction model even more.

This all points to the fact that the results presented in this thesis have a wide relevance, not only limited to the field of heme peroxidases, and may have important repercussions on the entire field of heme enzymes.

**References**


1. Yonetani, T., and Anni, H. (1987) Yeast cytochrome c peroxidase. Coordination and spin states of heme prosthetic group, *J Biol Chem 262*, 9547-9554.
2. Jones, D. K., Dalton, D. A., Rosell, F. I., and Raven, E. L. (1998) Class I heme peroxidases: characterization of soybean ascorbate peroxidase, *Arch Biochem Biophys 360*, 173-178.
3. Berglund, G. I., Carlsson, G. H., Smith, A. T., Szoke, H., Henriksen, A., and Hajdu, J. (2002) The catalytic pathway of horseradish peroxidase at high resolution, *Nature 417*, 463-468.
4. Miller, M. A., Shaw, A., and Kraut, J. (1994) 2.2 A structure of oxy-peroxidase as a model for the transient enzyme: peroxide complex, *Nat Struct Biol 1*, 524-531.
5. Vidossich, P., Fiorin, G., Alfonso-Prieto, M., Derat, E., Shaik, S., and Rovira, C. (2010) On the role of water in peroxidase catalysis: a theoretical investigation of HRP compound I formation, *J Phys Chem B 114*, 5161-5169.
6. Poulos, T. L., and Kraut, J. (1980) The stereochemistry of peroxidase catalysis, *J Biol Chem 255*, 8199-8205.
7. Montellano, P. R. O. d. (2005) *Cytochrome P450 Structure, Mechanism, and Biochemistry*, Third edition ed., Springer US.
8. Rittle, J., and Green, M. T. (2010) Cytochrome P450 Compound I: Capture, Characterization, and C-H Bond Activation Kinetics, *Science 330*, 933-937.
9. Groves, J. T. (2003) The bioinorganic chemistry of iron in oxygenases and supramolecular assemblies, *Proceedings of the National Academy of Sciences 100*, 3569-3574.

Chapter 5

# MATERIALS AND METHODS

## 5.1. MATERIALS

All chemicals used were of the highest analytical grade. Chemicals used to make buffer solutions were purchased from Fisher Chemicals, Sigma Aldrich, and Melford Laboratories Ltd. All chemicals and reagents were obtained from commercial sources and used without further purification unless otherwise stated. Water was of high quality, doubly deionised and was drawn from an Elga PureLab Option (DV35) water purifier, which itself was fed with deionised water.

## 5.2. EXPRESION OF PROTEINS

### 5.2.1. CYTOCHROME C PEROXIDASE

The MKT variant of C*c*P (*1*) was cloned by Dr. Yang (PROTEX service, University of Leicester) into the expression plasmid pLEICS-03 (Appendix B) carrying kanamycin resistance and a tobacco etch virus-cleavable N-terminal His tag sequence, in order to ease the protein purification process. Vector amplification was carried out by transformation into *E. coli* strand of supercompetent cells XL1 Blue (Stratagene). The amplified DNA was transformed into the *E. Coli* strand of competent cells BL21 DE3 Gold (Fisher Scientific) for expression (see appendix B for detailed procedures). Agar-LB plates containing kanamycin (30 μg/ml) were streaked with the transformed BL21 DE3 Gold cells and incubated, inverted at 37 °C, overnight.

#### 5.2.1.1. *Expression in LB media*

A single colony from the plate was used to inoculate 5 ml of autoclaved LB media. This was incubated for a maximum of 6 hours and then used to inoculate a flask with

320 ml LB broth containing kanamycin (30 μg/ml) which in turn was incubated overnight at 37 °C and shaken at 225 rpm and formed the starter culture. Starter culture (40 ml per litre) was added to 1 x 8 litre flasks containing autoclaved LB media with kanamycin (30 μg/ml). The flasks were shaken (225 rpm) at 37 °C until the absorbance of the cell culture reached a value between 0.6 and 0.8 at 600 nm (approximately 2 hours). The temperature of the incubator was then reduced to 22 °C and a solution 1 M of isopropyl β-D-1-thiogalactopyranoside (IPTG, final concentration 1 mM) was added to each flask to induce expression. The flasks were incubated overnight with shaking (225 rpm). The cells were finally harvested by centrifugation (5,000 rpm for 30 minutes at 4 °C). The cell pellets were then frozen at -80 °C, until needed.

#### 5.2.1.2. *Expression in minimal medium (M9)*

Expression of C*c*P in minimal medium was developed in order to allow production of perdeuterated protein suitable for neutron crystallography. A single colony of BL21 DE3 Gold transformed with C*c*P expression vector (pLEICS-03, appendix B) was picked from the plate and incubated in autoclaved LB broth (5 ml) for a maximum of 6 hours. The cell suspension was gently spun at 800 x *g* on bench centrifuge for 5 minutes and the supernatant discarded. The pellets were suspended in M9 minimal medium (prepared using $Na_2HPO_4$-$7H_2O$, 25g, $KH_2PO_4$, 6 g, NaCl, 1 g and $NH_4Cl$, 2 g, as indicated in Appendix B) and used to inoculate a flask containing M9 minimal medium (200 ml) with kanamycin (30 μg/ml) and shaken overnight at 37 °C to form a starter culture. Finally, starter culture (50 ml) was used to inoculate a 1 L flask containing M9 minimal

medium. The flasks were shaken (225 rpm) at 37 °C until the absorbance of the cell culture reached a value between 0.6 and 0.8 at 600 nm and then the expression was induced. The temperature of the incubator was reduced to 27 °C. Three different conditions for C*c*P expression were analysed. In the first one only a solution 1 M of isopropyl β-D-1-thiogalactopyranoside (IPTG, final concentration 1 mM) was added to each flask to induce expression. In the second one the same amount of IPTG was added in combination with a solution of hemin (final concentration 0.5 mg/L). In the third one double concentration of glucose was used and expression was induced with the same concentration of IPTG. Each experiment was repeated twice, incubating the flasks either for 24 hours or 60 hours (for a final number of 6 combinations). Expression level of each case was assessed by SDS-PAGE (see Fig. [3. 1]) and the optimised conditions were provided to the D-Lab at ILL for definitive expression of perdeuterated protein.

### 5.2.2. ASCORBATE PEROXIDASE

The vector containing APX gene (pQE-30 plasmid, see Appendix B (*2*)) was amplified by transformation in *E. coli* strand of supercompetent cells XL1 Blue (Stratagene). The amplified DNA was transformed into the *E. coli* competent cell strand SG13009 (Qiagen) for expression (Appendix B). Agar-LB plates (Appendix B) containing ampicillin (100 μg/ml) and kanamycin (30 μg/ml) were streaked with the transformed SG13009 cells and incubated, inverted at 37 °C, overnight. A single colony was used to inoculate 5 ml of autoclaved LB media. This was incubated for a maximum of 6 hours and then used to inoculate a flask with 320 ml LB broth containing both ampicillin (100

μg/ml) and kanamycin (30 μg/ml) which, in turn, was incubated overnight at 37 °C and shaked at 225 rpm and formed the starter culture. Starter culture (40 ml per litre) was added to 1 x 8 litre flasks containing autoclaved LB media with ampicillin (100 μg/ml) and kanamycin (30 μg/ml). The flasks were shaken (225 rpm) at 37 °C until the absorbance of the cell culture reached a value between 0.6 and 0.8 at 600 nm (approximately 2 hours). The temperature of the incubator was then reduced to 27 °C and a 1M solution of isopropyl β-D-1-thiogalactopyranoside (IPTG, final concentration 1 mM) was added to each flask to induce expression. The flasks were incubated overnight with shaking (225 rpm). The cells were finally harvested by centrifugation (5,000 rpm for 30 minutes at 4 °C). The cell pellets were then frozen at -80 °C, until needed.

## 5.3. ISOLATION AND PURIFICATION OF THE PROTEINS

### 5.3.1. CYTOCHROME C PEROXIDASE

C*c*P isolation and purification were carried out with modification of the published method (*1*). The pallets were suspended in sonication buffer A (potassium phosphate 150 mM, pH 6.5; about 20 ml of buffer per litre of culture) and a solution of phenyl-methane-sulfonyl fluoride (PMSF, 1.5 ml) was added, in order to inhibit protease activity. The suspension was then sonicated at 0 °C 8 x 1 minutes and the suspension thus obtained was spun at 20000 rpm for 40 minutes. The supernatant was collected and hemin solution (1 ml) was added to induce protein reconstitution. The solution was stirred for 1h and afterwards loaded onto a DEAE (Sigma) column equilibrated with sonication buffer A. After extensive washing, protein was eluted with sonication

buffer B and the pH adjusted to 8.0 by titration with a solution of NaOH 1 M. Protein solution was thus loaded onto a super flow Ni-nitrilotriacetic (NTA) agarose column (Qiagen), previously equilibrated with sonication buffer A, and washed first with sonication buffer B (200 ml) and finally with wash buffer (500 ml). Protein was eluted using elution buffer (≈ 150 ml), and the first 10-20 ml were discarded. The pH was set to 6 by titration with 1 M $KH_2PO_4$ and the solution concentrated up to 10 mg/ml. Protein purity was assessed by SDS-PAGE (Figure [5. 1]). For crystallographic purposes, C*c*P was finally purified by means of gel filtration chromatography (using a *GE healthcare* 16/60 HiLoad™ Superdex™ 75 column, previously equilibrated with FPLC buffer, potassium phosphate 10 mM, pH 6.5, KCl 150 mM), collecting only the fractions corresponding to the second part of the highest peak on the chromatograph (Figure [5. 2]-A).

### 5.3.2. ASCORBATE PEROXIDASE

APX isolation and purification were carried out as published (*3, 4*). The pallets were suspended in sonication buffer B (potassium phosphate 100 mM, pH 8.0, 300 mM KCl and 10% v/v glycerol; about 20 ml of buffer per litre of culture) followed by addition of phenyl-methane-sulfonyl fluoride (PMSF) solution (1.5 ml), bovine DNase (Sigma, 5 mg) and egg lysozime (Sigma, 5 mg). The suspension was then sonicated at 0 °C 8 x 1 minutes and the suspension thus obtained was spun at 20000 rpm for 40 minutes. The supernatant was collected and loaded onto a super flow Ni-nitrilotriacetic (NTA) agarose column (Qiagen), previously equilibrated with sonication buffer B, and washed first with sonication buffer B (200 ml) and finally with wash

buffer (potassium phosphate 100 mM, pH 6.0, 300 mM KCl and 10% v/v glycerol; 500 ml). Protein was eluted using elution buffer (potassium phosphate 100 mM, pH 4.2, 300 mM KCl and 10% v/v glycerol; ≈ 150 ml), and the first 10-20 ml collected were discarded. The pH was finally adjusted to 7 by titration with 1 M $KH_2PO_4$ (Sigma) and the reconstitution process induced by addition of hemin solution (5 mg of hemin (Sigma) dissolved in 1 ml of 0.1 M NaOH; 1.5 ml). Protein solution was stirred for 4h to allow complete reconstitution, dialysed overnight against FFQ buffer and afterwards loaded onto a fast flow Q-sepharose column (GE healthcare), previously equilibrated with FFQ buffer (potassium phosphate 10 mM pH 7.0). Protein was first washed with FFQ buffer, then eluted using FFQ buffer with 150 mM KCl; the collected fractions were concentrated up to 10 mg/ml and exchanged with deionised water. Protein purity was assessed by SDS-PAGE (Figure [5. 1]). For crystallographic purposes, APX was finally purified by means of gel filtration chromatography (using a *GE healthcare* 16/60 HiLoad™ Superdex™ 75 column, previously equilibrated with FPLC buffer, potassium phosphate 10 mM, pH 7.0, KCl 150 mM), collecting only the fractions corresponding to the second part of the highest peak on the chromatograph (Figure [5. 2]-B).

**Figure [5. 1]: Coomassie Blue-stained 15% SDS-PAGE gel of purified APX (lane A) and Cc*P* (lane C). Bio-Rad molecular mass standard is in Lane B.**

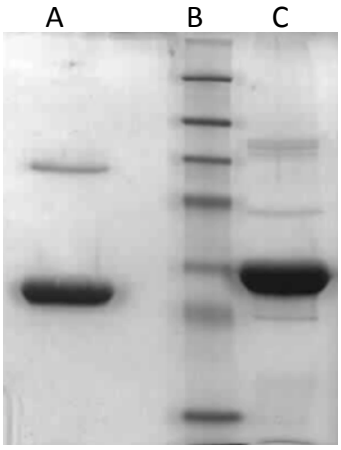


**Figure [5. 2]: Chromatographs of FPLC purification of C*c*P (A) and APX (B).**

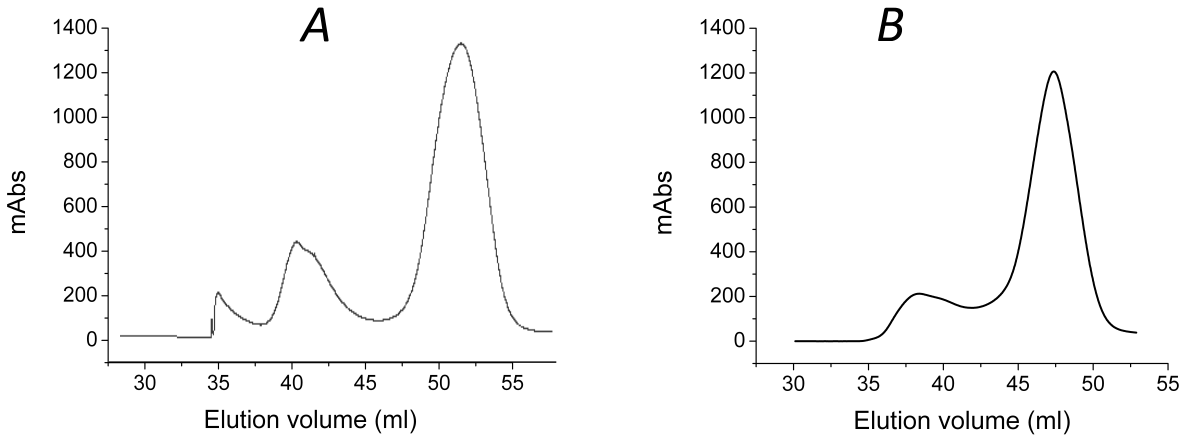


## 5.4. CRYSTALLISATION OF PROTEINS

### 5.4.1. CYTOCHROME *C* PEROXIDASE

C*c*P and perdeuterated C*c*P were crystallised as previously described (*5*). C*c*P solutions were first crystallised by dialysis against double distilled water for 3-5 days. The crystals were then re-dissolved in a solution of potassium phosphate 500 mM, pH 6.5 and the same procedure repeated 4-5 times. Finally C*c*P was crystallised by dialysis, using 100 µL dialysis buttons (Hampton Research), against a solution of 50 mM potassium phosphate, pH 6.0, containing (±)-2-methyl-2,4-pentanediol (30% v/v).

For neutron crystallography, crystals were lately soaked in deuterated mother liquor to allow the exchange of all labile protons.

Compound I of C*c*P was formed by soaking crystals of ferric enzyme in freshly prepared C*c*P mother liquor containing $H_2O_2$ (20 mM) for 5 minutes, and crystals were then flash-frozen at 100 K.

#### 5.4.2. ASCORBATE PEROXIDASE

APX crystals were prepared by vapour diffusion (*6*). Sitting drops, made up of 2 µl protein solution (10 mg/ml) and 2 µl precipitant solution, were allowed to equilibrate with 700 µl of precipitant (2.25 M $Li_2SO_4$ and 0.1 M HEPES, pH 8.3) to give crystals ~150 µm × 75 µm × 75 µm. Crystals thus obtained were directly used for X-ray. Compounds II and III of APX were prepared by soaking crystals of ferric enzyme in APX mother liquor containing $H_2O_2$ (200 µM) or $H_2O_2$ (20 mM) for 5 minutes, respectively, and frozen as above. All reacted crystals were stored in liquid nitrogen.

## 5.5. CRYSTALLOGRAPHIC DATA COLLECTION

### 5.5.1. X-RAY DATA OF OXY-FERRYL INTERMEDIATES

#### 5.5.1.1. *Cytochrome c peroxidase*

For the structure of C*c*P intermediates, X-ray diffraction data were collected in-house at 100 K using CuKα radiation (λ=1.5418 Å) from a Rigaku RU2HB X-ray generator with a copper anode and Xenocs multilayer optics and measured with an R-AXIS IV detector. In all cases, 5% of the data were flagged for the calculation of $R_{free}$

and excluded from subsequent refinement. Data collection statistics are shown in Chapter 2 (Tables [2. 1], [2. 2] and [2. 3]),

Diffraction data for ferric C*c*P at 100 K were collected in-house using CuKα radiation (λ= 1.5418 Å) from a Rigaku MicroMax-007HF generator with a copper anode and Varimax HF optics (75 micrometer focus, 1.2 kW), measured with a CCD Saturn 944+ detector (statistics are presented in Chapter 3, Table [3. 2]).

#### 5.5.1.2. *Ascorbate peroxidase*

For the structures of APX intermediates and ferric APX at 100 K, diffraction data were collected on beam line I04 (wavelength λ=0.6 Å) at Diamond Light Source, Harwell, UK using an ADSC Q315 CCD detector, at 100 K. C*c*P data were indexed, integrated, merged, and scaled, respectively, using MOSFLM, SORTMTZ, and SCALA as part of the CCP4 suite (*7, 8*); APX data were integrated, merged, and scaled using XDS (*9*). In all cases, 5% of the data were flagged for the calculation of $R_{free}$ and excluded from subsequent refinement. Data collection statistics are shown in Chapter 2 (Tables [2. 1], [2. 2] and [2. 3]), and Chapter 3 (Table [3. 2]).

### 5.5.2. X-RAY DATA FOR ROOM TEMPERATURE C*c*P NEUTRON COMBINED STRUCTURE

C*c*P crystals were mounted in 0.7 mm diameter glass capillary tubes (Glaskapillaren, Astrophysics research limited) and sealed with wax. Data were collected using a Rigaku RU2HB X-ray generator with copper anode and Xenocs multilayer optics and an R-Axis IV detector. To minimise the damaging effects of X-ray exposure at room temperature, data were collected from two crystals, with 30 degrees of data (60 images) collected on each. The individual data sets were integrated using

MOSFLM and combined and scaled using SCALA in the CCP4 suite (*8*). Data collection statistics are shown in Chapter 3, Table [3. 2].

### 5.5.3. NEUTRON DATA COLLECTION

Neutron quasi-Laue data to 2.40 Å resolution were collected on the LADI-III Laue diffractometer beam-line (installed on cold neutron guide H142) using a restricted neutron wavelength range ($\delta\lambda/\lambda \approx 25\%$) centred at 3.7 Å and extending from 3.2 to 4.2 Å. As is typical for a Laue experiment, the chosen crystal (in a quartz capillary sealed with wax) was held stationary at a different $\phi$ setting (around the vertical rotation axis of the detector) for each exposure. Data were collected in two experiments. Initially, a deuterated crystal of C*c*P with volume of ≈0.8mm$^3$ was used to collect 9 contiguous images ($\Delta\phi = 14°$) using an exposure time of 15 h per image. Successively, a second deuterated crystal of C*c*P (with volume of ~0.5mm$^3$) was diffracted in order to complete the first data set. For this crystal, first 13 contiguous images ($\Delta\phi = 7°$) with an exposure time of 24 h per image were collected in order to collect the high-resolution data, followed by a low-resolution pass of 17 contiguous images ($\Delta\phi = 7°$) with an exposure time of 3.5 h per image. The neutron Laue data images were processed using the Daresbury Laboratory LAUE suite program LAUEGEN, which was modified to account for the cylindrical geometry of the detector (*10*). The program LSCALE (*11*) was used to determine the wavelength-normalization curve using the intensities of symmetry-equivalent reflections measured at different wavelengths and to apply wavelength-normalization calculations to the observed data. Although not as good as a single crystal data set, the two data sets were sufficiently isomorphous to allow us to

combine and merge them together to produce a single data set of 12,903 unique reflections to 2.40 Å resolution, with an overall merging R factor of 16.8% (12.2% at low to 19.4% at high resolution). Data collection statistics are summarized in Chapter 3 (Tables [3. 1] and [3. 3]).

## 5.6. MULTICRYSTAL X-RAY DATA ANALYSIS

### 5.6.1. CYTOCHROME *C* PEROXIDASE

The structures of C*c*P Compound I and ferric C*c*P at 100 K were solved merging the first 9° of data from 10 different crystals. This corresponds to a maximum absorbed dose of 0.020 MGy (calculated with RADDOSE (*12*)). We established the amount of data that could be collected from each crystal before the effects of photoreduction showed empirically by truncating the data after various doses. We determined that no detectable change in the observed structure was seen with this (or a lesser) dose but was apparent after a higher dose. Compound II of C*c*P and ferrous C*c*P were obtained by the photoreduction of Compound I (absorbed dose of ≈0.15 MGy and ≈0.35 MGy, respectively) and verified by UV-visible single crystal spectrophotometry. Diffraction data were collected following photoreduction by merging together the first 9° of data from 10 crystals.

In order to avoid the crystals being exposed to any X-ray radiation prior to data collection, no test exposure to determine data collection strategy was used. Instead, the crystals were randomly oriented on the beam thus to increase the possibility of collecting complementary, yet cross scalable fractions of data.

### 5.6.2. ASCORBATE PEROXIDASE

The structures of APX Compound II, Compound III and ferric APX at 100 K were solved from three crystals as it was found that by using 0.6 Å radiation the photoelectron effect is significantly reduced (*13*), allowing at least 15° to be collected before there was any indication of photoreduction, despite the high intensity of the synchrotron radiation. This corresponds to an absorbed dose of 0.028 MGy (calculated with RADDOSE (*12*)). Compound I of APX and ferrous APX were produced by photoreduction of Compound III (absorbed dose ≈0.15 MGy and ≈0.35 MGy) and verified by UV-visible single crystal spectrophotometry (see section 5.8.). Diffraction data for Compound I and ferrous were also obtained from three crystals (using the first 15° after the photoreduction). As for C*c*P, APX crystals were randomly oriented so that no exposure occurred prior to data collection.

## 5.7. REFINEMENT OF CRYSTALLOGRAPHIC DATA

### 5.7.1. MULTI-CRYSTAL DATA

Crystallographic refinement initially used REFMAC5 (*14*) from the CCP4 suite (*8*). All C*c*P structures were refined from the 1.70 Å wild-type C*c*P structure (*15*) (1ZBY) whereas structures of APX were refined from the 1.45 Å ferric APX structure (*6*) (1OAG). In all cases water molecules were removed from the model before use. To ensure the unbiased determination of the iron-oxygen distances, the entire protein

structures were refined with the ferryl oxygen atom omitted, and the ferryl oxygen was first fitted to the peak of the $F_o$-$F_c$ difference map and refined in real space using COOT (*16*). The complete models were then refined with SHELX (*17*), allowing the estimation of individual atomic positional uncertainties (Estimated Standard Uncertainty (ESU)). Refinement statistics are presented in Chapter 2, Tables [2. 1], [2. 2] and [2. 3], and in Chapter 3, Table [3. 2].

### 5.7.2. REFINEMENT OF CcP ROOM TEMPERATURE X-RAY DATA

Using the 1.7 Å resolution wild type C*c*P X-ray structure (PDB entry 2CYP) as a starting model, refinement of the structure (positional and B-factor) was performed against the room temperature X-ray data using REFMAC5 (*14*) from the CCP4 suite (*8*). COOT (*16*) was used throughout for manual adjustment, ligand fitting and interpretation of the water structure. Summary data collection and refinement statistics are shown in Chapter 3, Table [3. 2].

### 5.7.3. X-RAY/NEUTRON JOINT REFINEMENT

The X-ray structural model of C*c*P to 2.0 Å resolution determined at room-temperature was used as the starting model for the joint X-ray and neutron refinement using nCNS (*18*) which combines global X-ray data, neutron data and energy refinement with cross-validated maximum likelihood simulated annealing refinement. The model was modified by removing all water molecules and adding hydrogen atoms at calculated positions for non-exchangeable sites. Initially rigid-body

refinement was performed, followed by several cycles of maximum-likelihood-based refinement of individual coordinates and atomic displacement parameters (ADPs). Using the modeling program COOT (*16*), rotamer and torsion angle adjustments were made manually throughout the model according to positive nuclear density in both σA-weighted $2F_o$-$F_c$ and $F_o$-$F_c$ maps. The positions of D-atoms of the protein (*i.e.* at exchangeable sites) and $D_2O$ molecules were added to the model according to positive nuclear density in σA-weighted $F_o$-$F_c$ maps, with manual adjustment of all $D_2O$ molecules completed using both σA-weighted $F_o$-$F_c$ and $F_o$-$F_c$ nuclear density maps. A final refinement process was completed using Phenix (*19*). The final refinement statistics are summarized in Chapter 3, Table [3. 3].

All figures were prepared using Pymol (*20*)

## 5.8. MONITORING OF PHOTOREDUCTION

Changes in UV-visible absorbance spectra during X-ray exposure were monitored at the European Synchrotron Radiation Facility (ESRF) ID14-2 using an on-line spectrophotometer (OCEAN OPTICS DH 2000 light source and HR 2000 detector)(*21*). UV-visible spectra of exposed crystals used to solve the structures of C*c*P Compound II, APX Compound I, ferrous C*c*P, and APX were measured using a 4DX single crystal microspectrophotometer with a Shamrock SR-163 spectrograph and Newton CCD camera (Andor Technology).

## References


1. Goodin, D. B., Davidson, M. G., Roe, J. A., Mauk, A. G., and Smith, M. (1991) Amino acid substitutions at tryptophan-51 of cytochrome c peroxidase: effects on coordination, species preference for cytochrome c, and electron transfer, *Biochemistry 30*, 4953-4962.
2. Dalton, D. A., Diaz del Castillo, L., Kahn, M. L., Joyner, S. L., and Chatfield, J. M. (1996) Heterologous expression and characterization of soybean cytosolic ascorbate peroxidase, *Arch Biochem Biophys 328*, 1-8.
3. Metcalfe, C. L., Ott, M., Patel, N., Singh, K., Mistry, S. C., Goff, H. M., and Raven, E. L. (2004) Autocatalytic formation of green heme: evidence for H2O2-dependent formation of a covalent methionine-heme linkage in ascorbate peroxidase, *J Am Chem Soc 126*, 16242-16248.
4. Zoi Pipirou, A. R. B., Dimitri A. Svistunenko, Igor Efimov, Jaswir Basran, Sharad C. Mistry, Christopher E. Cooper, and Emma Lloyd Raven. (2007) The Reactivity of Heme in Biological Systems: Autocatalytic Formation of Both Tyrosine-Heme and Tryptophan-Heme Covalent Links in a Single Protein Architecture, *Biochemistry 46*, 13269-13278.
5. Metcalfe, C., Macdonald, I. K., Murphy, E. J., Brown, K. A., Raven, E. L., and Moody, P. C. (2008) The tuberculosis prodrug isoniazid bound to activating peroxidases, *J Biol Chem 283*, 6193-6200.
6. Sharp, K. H., Mewies, M., Moody, P. C., and Raven, E. L. (2003) Crystal structure of the ascorbate peroxidase-ascorbate complex, *Nat Struct Biol 10*, 303-307.
7. Evans, P. (2006) Scaling and assessment of data quality, *Acta Crystallogr D Biol Crystallogr 62*, 72-82.
8. Project, C. C. (1994) The CCP4 suite: programs for protein crystallography, *Acta Crystallographica Section D 50*, 760-763.
9. Kabsch, W. (1993) Automatic processing of rotation diffraction data from crystals of initially unknown symmetry and cell constants, *Journal of Applied Crystallography 26*, 795-800.
10. Campbell, J. W., Hao, Q., Harding, M. M., Nguti, N. D., and Wilkinson, C. (1998) LAUEGEN version 6.0 and INTLDM, *Journal of Applied Crystallography 31*, 496-502.
11. Arzt, S., Campbell, J. W., Harding, M. M., Hao, Q., and Helliwell, J. R. (1999) LSCALE - the new normalization, scaling and absorption correction program in the Daresbury Laue software suite, *Journal of Applied Crystallography 32*, 554-562.
12. Paithankar, K. S., and Garman, E. F. (2010) Know your dose: RADDOSE, *Acta Crystallographica Section D 66*, 381-388.
13. Unno, M., Chen, H., Kusama, S., Shaik, S., and Ikeda-Saito, M. (2007) Structural characterization of the fleeting ferric peroxo species in myoglobin: experiment and theory, *Journal of the American Chemical Society 129*, 13394-13395.
14. Murshudov, G. N., Vagin, A. A., and Dodson, E. J. (1997) Refinement of macromolecular structures by the maximum-likelihood method, *Acta Crystallogr D Biol Crystallogr 53*, 240-255.

15. Finzel, B. C., Poulos, T. L., and Kraut, J. (1984) Crystal structure of yeast cytochrome c peroxidase refined at 1.7-A resolution, *J Biol Chem 259*, 13027-13036.
16. Emsley, P., and Cowtan, K. (2004) Coot: model-building tools for molecular graphics, *Acta Crystallographica Section D 60*, 2126-2132.
17. Sheldrick, G. (2008) A short history of SHELX, *Acta Crystallographica Section A 64*, 112-122.
18. Brunger, A. T., Adams, P. D., Clore, G. M., DeLano, W. L., Gros, P., Grosse-Kunstleve, R. W., Jiang, J. S., Kuszewski, J., Nilges, M., Pannu, N. S., Read, R. J., Rice, L. M., Simonson, T., and Warren, G. L. (1998) Crystallography & NMR system: A new software suite for macromolecular structure determination, *Acta Crystallogr D 54*, 905-921.
19. Adams, P. D., Afonine, P. V., Bunkoczi, G., Chen, V. B., Davis, I. W., Echols, N., Headd, J. J., Hung, L.-W., Kapral, G. J., Grosse-Kunstleve, R. W., McCoy, A. J., Moriarty, N. W., Oeffner, R., Read, R. J., Richardson, D. C., Richardson, J. S., Terwilliger, T. C., and Zwart, P. H. (2010) PHENIX: a comprehensive Python-based system for macromolecular structure solution, *Acta Crystallographica Section D 66*, 213-221.
20. DeLano, W. L. (2010) The PyMOL Molecular Graphics System, DeLano Scientific LLC, San Carlo.
21. McGeehan, J., Ravelli, R. B. G., Murray, J. W., Owen, R. L., Cipriani, F., McSweeney, S., Weik, M., and Garman, E. F. (2009) Colouring cryo-cooled crystals: online microspectrophotometry, *Journal of Synchrotron Radiation 16*, 163-172.

Appendix A

# STRUCTURAL AND SPECTROSCOPIC CHARACTERISATION OF DISTAL POCKET VARIANTS OF APX

## A.1. INTRODUCTION

Over the last few years several APX variants have been produced and characterised. The information gained has not only led to new insights into the reaction mechanism of this heme peroxidase, but it has also provided an insight into aspects related to other heme enzymes (*1-9*). One of such variants is the APX W41A, which has been recently studied in our lab (*6, 9*). The structural and chemical studies have shown that by removing the bulky distal Trp41, allows the His42 to gain a certain flexibility, allowing the His42 side chain to coordinate to the heme and produce an enzyme with a bis-histidine heme ligation, mimicking the structure of electron transfer proteins such as the cytochromes *b*. Nevertheless, data indicated that the His42-heme coordination was reversible and that the APX W41A variant was still able to reduce $H_2O_2$ in the presence of ascorbate. In addition, it was observed that the His42-heme coordination was affected by changes in the Fe oxidation state.

On the basis of these results, three APX mutants were prepared in order to further investigate the possible consequences of the increased flexibility of position 42. The three variants were produced with the crucial Trp41Ala mutation and in addition different residues were introduced in position 42: cysteine, methionine and tyrosine, respectively (Table [A. 1]). Due to a lack of time, only part of the planned studies has been completed and these are reported below. Data collected consist of crystallographic determination of the mutant structures and the spectroscopic characterisation of the resting mutants and upon reaction with hydrogen peroxide.

**Table [A. 1]: List of APX double mutants**

| APX mutant | Mutations | |
|---|---|---|
| 1 | W41A | H42C |
| 2 | W41A | H42M |
| 3 | W41A | H42Y |

## A.2. RESULTS

### A.2.1. CRYSTALLOGRAPHIC CHARACTERISATION

Figure [A. 1] presents the distal heme side three double mutants. In all cases the mutations have induced formation of a large, empty cavity on the heme distal side. In all these variants the side chain of the mutated residue in position 42 lies away from the heme plane and there is no evidence of formation of a 6-coordinated heme, as observed in the W41A variant (*9*). The distal side of the heme is occupied by a large electron density, which could arise from the presence of a few water molecules that are not precisely ordered. However, for the case of the W41A/H42Y mutant, this electron density can be fitted by a molecule of HEPES (4-(2-hydroxyethyl)-1-piperazineethanesulfonic acid, used as a pH buffer in the mother liquor), although with an occupancy less than 1.0 (*9*). A closer view of the W41A/H42Y structure (Figure [A. 2]) indicates that HEPES is particularly allowed in the above site by the rearrangement of Leu131. The side of this residues is flipped with respect to the wild type APX (Figure [A. 3]) and points “outwards” the heme pocket, towards the solvent, allowing thus the sulphonate group of the HEPES to fit within the region adjacent to the amidic oxygen of the Thr42 backbone, Gly45 backbone and the Leu131 backbone. Furthermore, the

sulphonate group of the HEPES is stabilised by formation of three hydrogen bonds (Figure [A. 3]). In the other two mutants, the electron density map mainly indicates that Leu131 retains its original conformation, (Figure [A. 4]), although a possible equilibrium between the two different conformations, with a very low occupancy of the second one, cannot be completely ruled out. This equilibrium would also be consistent with the possibility that a molecule of HEPES could fit inside the heme distal pocket of the W41A/H42C and W41A/H42M mutants, although with a very low occupancy, and partially explain the circular character of the electron density map above the heme plane.

**Figure [A. 1]: Structures of the distal heme side of the APX double mutants. W41A/H42C (A) is shown in cyan, W41A/H42M (B) in purple and W41A/H42Y (C) in green. HEPES is shown as yellow sticks, heme as red sticks. Oxygen atoms are in red, sulphur atoms in dark yellow and nitrogen atoms in blue. Electron density maps, calculated with coefficients 2Fo-Fc contoured at 2σ, are shown in blue.**

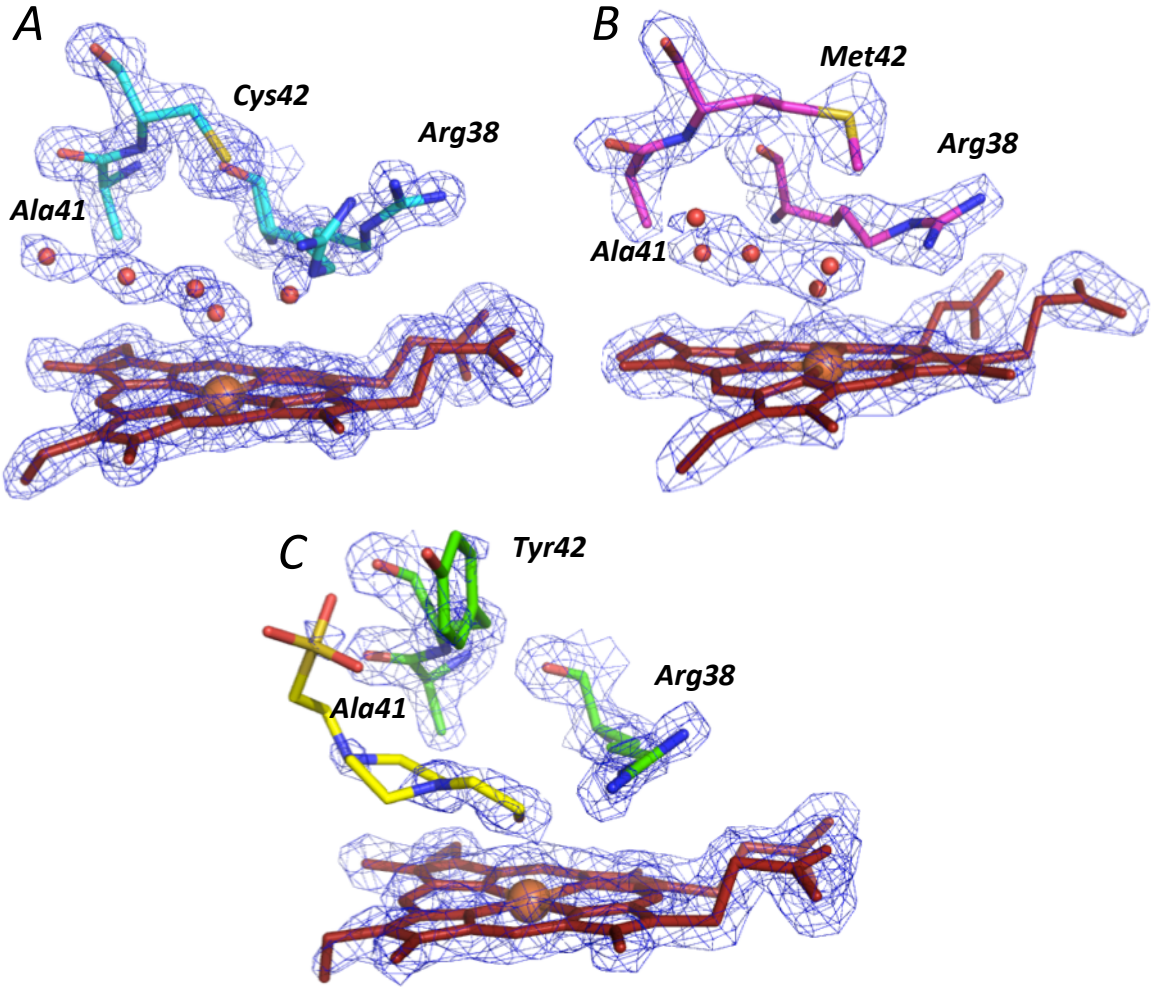

**Figure [A. 2]: A structure of the distal heme region of the W41A/H42Y variant. The mutation produced a cavity, which is able to accommodate and bind a molecule of HEPES (shown in yellow). W41A/H42Y is shown as green sticks and the heme in red. Oxygen atoms are in red and nitrogen atoms are in blue. Hydrogen bonds are shown as red dashed lines and the main residues are labelled.**

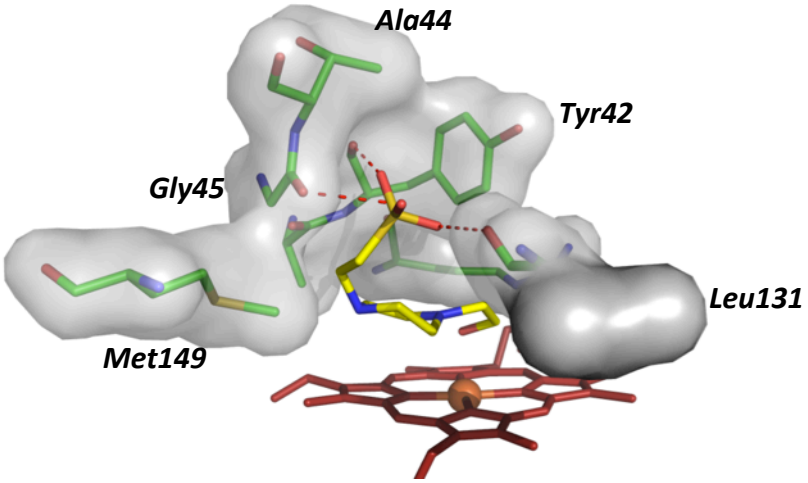


**Figure [A. 3]: Superimposition of the structure of the distal heme side of wild type APX with that of the HEPES occupying the active site of the W41A/H42Y variant. The wild type APX is shown as white sticks, the HEPES in yellow and the heme in red. Oxygen atoms are in red and nitrogen atoms are in blue. Main residues are labelled.**

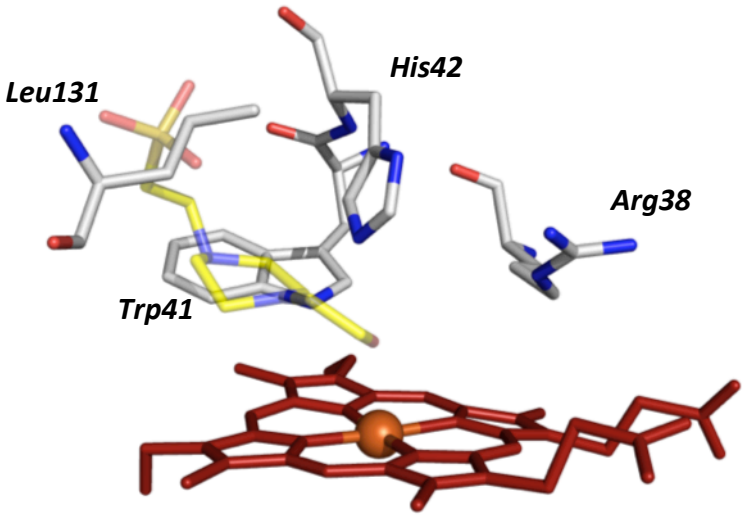

### A.2.2. SPECTROSCOPIC CHARACTERISATION

Values of the absorption coefficient calculated at the Soret band (*10*) for these mutants are reported in Table [A. 3]. UV-visible spectra of the mutants in solution are reported in Figure [A. 5] and they show very similar features: in all cases the Soret band maxima are at 402 nm whereas the β-band maxima are at 500 nm, with a shoulder at about 540 nm. The α-band maxima are slightly different: 633 nm for W41A/H42M and W41A/H42C mutants and 636 nm for the W41A/H42Y variant. Comparison of these values with those reported for wild type APX (*11*) ($\lambda_{max}$ (nm) = 407, 525, ≈630) and W41A mutant (*9*) ($\lambda_{max}$ (nm) = 405, 525, $564^{sh}$, 630) indicates a blue shift of both the double mutants' Soret peaks and β-bands that is mainly consistent with the presence of high-spin heme. This interpretation would also be consistent with the crystallographic evidence that no strong ligation (either internal or external) occur on the distal side of the heme.

**Figure [A. 4]: Superimposed structure of the distal heme side of the W41A/H42C variant (cyan) and W41A/H42M variant (purple), with that of the HEPES occupying the distal pocket of W41A/H42Y. The steric hindrance of the Leu131 side chain does not allow HEPES to access the distal pocket. The HEPES is in yellow and the heme in red. Oxygen atoms are in red and nitrogen atoms are in blue. Main residues are labelled.**

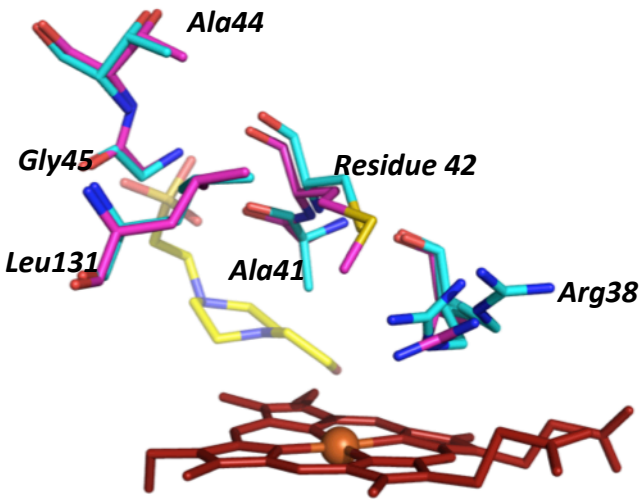

**Table [A. 2]: Data collection and refinement statistics for the three APX double mutants (Statistics for the outer resolution bin are shown in parentheses).**

| **Data collection** | **Mutant** | | |
|---|---|---|---|
| | W41A-H42C | W41A-H42M | W41A-H42Y |
| Space group | $P4_22_12$ | $P4_22_12$ | $P4_22_12$ |
| Cell dimension a, b, c (Å) | 82.29, 82.29, 75.28 | 82.75, 82.75, 75.00 | 82.01, 82.01, 75.06 |
| Resolution (Å) | 37.64 - 1.49 (1.57 - 1.49) | 55.57 - 2.20 (2.32 - 2.20) | 37.53 – 1.85 (1.95 – 1.85) |
| $R_{merge}$ (%) | 6.8 (36.3) | 7.4 (13.8) | 6.3 (28.8) |
| I/σI | 18 (5.4) | 20.9 (12.4) | 15.3 (4.9) |
| Completeness (%) | 99.9 (100) | 99.2 (98.1) | 98.4 (99.0) |
| Multiplicity | 8.3 (8.5) | 8.4 (8.6) | 4.0 (4.1) |
| **Refinement** | | | |
| Resolution (Å) | 36.80 - 1.49 | 46.13 - 2.20 | 36.67 - 1.85 |
| No. of reflections | 40457 | 12896 | 20789 |
| $R_{work}/R_{free}$ (%) | 16.3/19.5 | 16.19/22.81 | 16.58/21.02 |
| Protein Ligand/ion | 2/3 | 2/2 | 2/3 |
| Water | 362 | 259 | 258 |
| Overall B-factors | 18.59 | 19.63 | 19.76 |
| r.m.s. deviations | | | |
| Bond lengths (Å) | 0.032 | 0.023 | 0.027 |
| Bond ang | 2.588 | 1.841 | 2.12 |

**Table [A. 3]: Molar extinction coefficients of the APX variants calculated at the Soret band, by means of a hemochromogen assay, and wavelength of absorbance maxima observed by UV-visible spectroscopy (Figure [A. 5]).**

| Mutant | ε ($mM^{-1}$ $cm^{-1}$) | Soret band (nm) | α–band (nm) | β–band (nm) |
|---|---|---|---|---|
| W41A_H41C | 122 | 402 | 633 | 500 |
| W41A_H41M | 120 | 402 | 633 | 500 |
| W41A_H41Y | 103 | 402 | 636 | 500 |

**Figure [A. 5]: UV-visible spectra of the solutions of W41A/H42C (solid line), W41A/H42M (dotted-dashed line) and W41A/H42Y (dotted line). Proteins were dissolved in 50 mM phosphate buffer, pH 7.0. Spectra were collected at 25° C. Absorbance in the visible region was multiplied by a factor of 5 times for clarity.**

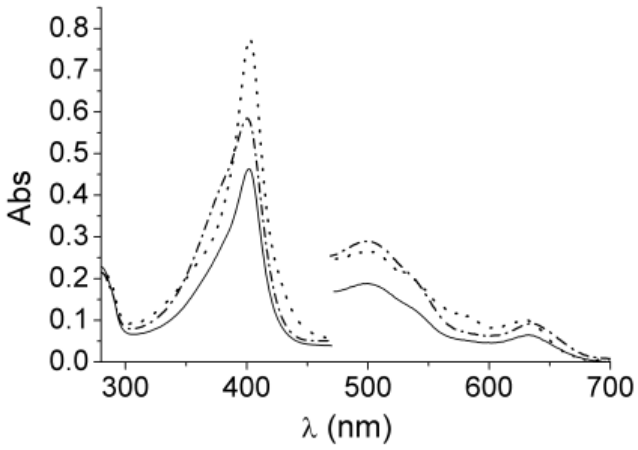


**Figure [A. 6]: Changes of the UV-visible spectrum of (A) W41A/H42Y and (B) W41A/H42M, upon reaction with hydrogen peroxide. Enzymes were reacted with 5 equivalents and 2 equivalents of hydrogen peroxide, respectively, in 50 mM phosphate buffer pH 7. Spectra were collected every 30 and 60 seconds respectively.**

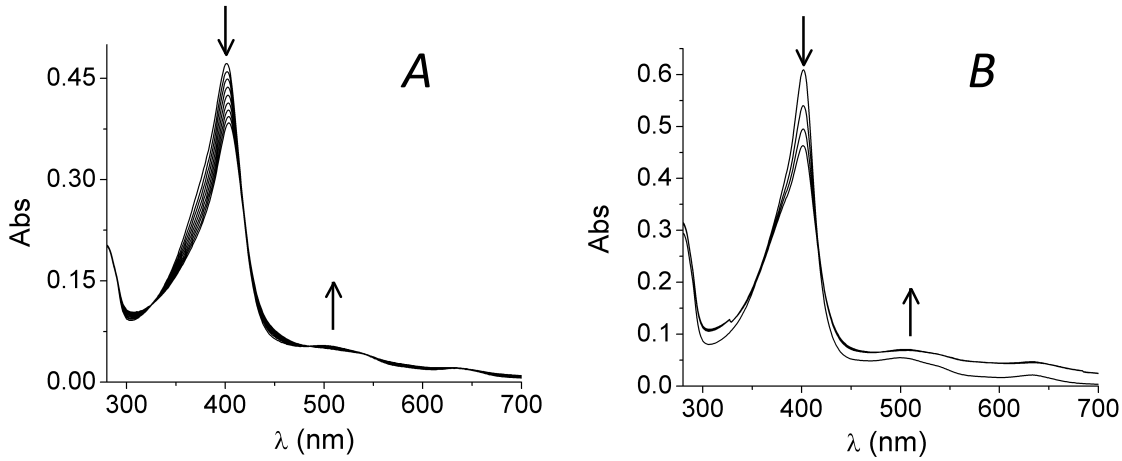

### A.2.3. REACTIVITY AGAINST HYDROGEN PEROXIDE

#### *A.2.3.1. UV-visible spectroscopy*

The reaction of the APX double mutants with hydrogen peroxide, in the absence of ascorbate, did not lead to formation of any intermediate stable enough to be observed and trapped at room temperature, but it only produced a quick and general decay of the absorbance intensity, possibly consistent with degradation of the protein (Figure [A. 6]). However, for the W41A/H42Y variant, a change of the wavelength of the Soret band maximum occurred during decay, and the peak red-shifted, moving from 402 nm to 404-405 nm. (Figure [A. 6]-A). These observations could be consistent with formation of a relatively unstable species, not formed in the other two APX variants. For this reason this species has been further investigated by EPR.

#### *A.2.3.2. EPR analysis of the $H_2O_2$-reacted W41A/H42Y mutant*

A preliminary EPR study of the species formed upon reaction of the W41A/H42Y APX variant with hydrogen peroxide in equimolecular concentration is reported in Figure [A. 7]. This shows a signal at $g$=2.0 consistent with formation of a protein radical, perhaps localised on the side chain of the Tyr42. The signal at $g$=5.6 could be consistent with the presence of some unreacted ferric heme in the sample, whereas the signal at $g$=4.7 might arise either from a spin-coupling effect or from the presence of a heme spin admixture.

**Figure [A. 7]: EPR derivative spectrum of W41A/H42Y APX mutant (0.2 mM) in 50 mM potassium phosphate, pH 7; microwave frequency, 9.51 GHz; microwave power, 2.0 mW; modulation amplitude, 10.00 G; modulation frequency, 100 kHz; field sweep rate, 35.76 G/s; time constant, 0.327 s; gain, 70 dB.**

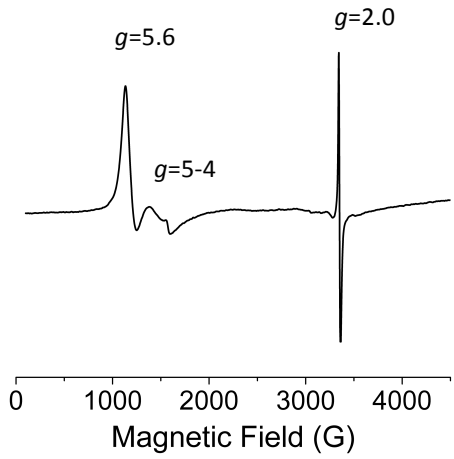

## A.3. DISCUSSION AND FUTURE WORK

The presented APX variants show structural feature that evidently diverge from the wild type. As for the W41A mutant (*9*), the absence of the bulky Trp41 creates a large distal cavity and increases the flexibility of the residue in position 42. However, the mutations introduced in position 42 cause visible changes even at the level of the backbone, around Leu131. For the W41A/H42Y mutant these changes are particularly evident and result in a complete inversion of the orientation of the Leu131 side chain, allowing for the formation of an even larger distal cavity (see Figure [A. 2] and Figure [A. 3]). Moreover, owing to the specific orientation of the amide oxygen atoms of the Leu131 and surrounding residues, the enlarged cavity shows a rather hydrophilic character, which inverts the original hydrophobic properties of the heme distal pocket. It is interesting to note that a similar effect was also observed for the His52Tyr variant of C*c*P (*12*).

Interestingly, the variation of polarity of the heme distal pocket, together with the formation of a wider cavity, can potentially allow for various polar and large molecules to fully access the heme distal side (as observed for the HEPES). Therefore, these modified enzymes can be considered new catalysts, potentially able to oxidise substrates with specific, polar and structural properties. Furthermore, these studies evidence the possibility that polarity of the APX active site can be engineered in order to be adapted to specific substrates. However more kinetic studies are required to definitely prove these possibilities.

Finally the presence of a radical species in the $H_2O_2$-reacted W41A/H42Y variant evidenced by EPR, suggests that the mutations might have effects on the APX reaction

mechanism and further investigation could provide new insight into the understanding of heme enzymes in general. A previous study on C*c*P (*12*) pointed out that reaction of the His52Tyr variant with hydrogen peroxide caused the introduced Tyr52 to form a covalent bond with the distal tryptophan (Trp51). In the W41A/H42Y variant of APX the distal tryptophan has been removed. However, on the basis of these results, it would be interesting to observe whether structural rearrangements, upon reaction with hydrogen peroxide, also occur in the APX double mutants, as this would provide precise information about the way the introduced mutations have modified the activity of the enzyme.

**References**


1. Zoi Pipirou, A. R. B., Clive M. Metcalfe, Sharad C. Mistry, Sandip K. Badyal,, and Bernard J. Rawlings, a. E. L. R. (2007) Autocatalytic Formation of a Covalent Link between Tryptophan 41 and the Heme in ascorbate Peroxidase, *Biochemistry 46*, 2174-2180.
2. Metcalfe, C. L., Ott, M., Patel, N., Singh, K., Mistry, S. C., Goff, H. M., and Raven, E. L. (2004) Autocatalytic formation of green heme: evidence for H2O2-dependent formation of a covalent methionine-heme linkage in ascorbate peroxidase, *J Am Chem Soc 126*, 16242-16248.
3. Lad, L., Mewies, M., Basran, J., Scrutton, N. S., and Raven, E. L. (2002) Role of histidine 42 in ascorbate peroxidase. Kinetic analysis of the H42A and H42E variants, *Eur J Biochem 269*, 3182-3192.
4. Zoi Pipirou, A. R. B., Dimitri A. Svistunenko, Igor Efimov, Jaswir Basran, Sharad C. Mistry, Christopher E. Cooper, and Emma Lloyd Raven. (2007) The Reactivity of Heme in Biological Systems: Autocatalytic Formation of Both Tyrosine-Heme and Tryptophan-Heme Covalent Links in a Single Protein Architecture, *Biochemistry 46*, 13269-13278.
5. Badyal, S. K., Eaton, G., Mistry, S., Pipirou, Z., Basran, J., Metcalfe, C. L., Gumiero, A., Handa, S., Moody, P. C., and Raven, E. L. (2009) Evidence for heme oxygenase activity in a heme peroxidase, *Biochemistry 48*, 4738-4746.
6. Badyal, S. K., Metcalfe, C. L., Basran, J., Efimov, I., Moody, P. C., and Raven, E. L. (2008) Iron oxidation state modulates active site structure in a heme peroxidase, *Biochemistry 47*, 4403-4409.
7. Metcalfe, C., Macdonald, I. K., Murphy, E. J., Brown, K. A., Raven, E. L., and Moody, P. C. (2008) The tuberculosis prodrug isoniazid bound to activating peroxidases, *J Biol Chem 283*, 6193-6200.
8. Macdonald, I. K., Badyal, S. K., Ghamsari, L., Moody, P. C., and Raven, E. L. (2006) Interaction of ascorbate peroxidase with substrates: a mechanistic and structural analysis, *Biochemistry 45*, 7808-7817.
9. Badyal, S. K., Joyce, M. G., Sharp, K. H., Seward, H. E., Mewies, M., Basran, J., Macdonald, I. K., Moody, P. C., and Raven, E. L. (2006) Conformational mobility in the active site of a heme peroxidase, *J Biol Chem 281*, 24512-24520.
10. Antonini, E., and Brunori, M. (1971) Hemoglobin and myoglobin in their reactions with ligands., illustrated ed., North-Holland Pub. Co.
11. Lad, L., Mewies, M., and Raven, E. L. (2002) Substrate binding and catalytic mechanism in ascorbate peroxidase: evidence for two ascorbate binding sites, *Biochemistry 41*, 13774-13781.
12. Bhaskar, B., Immoos, C. E., Shimizu, H., Sulc, F., Farmer, P. J., and Poulos, T. L. (2003) A Novel Heme and Peroxide-dependent Tryptophan-tyrosine Cross-link in a Mutant of Cytochrome c Peroxidase, *Journal of Molecular Biology 328*, 157-166.

Appendix B

# PROCEDURES AND BUFFERS

## B.1. TRANSFORMATION INTO XL1 BLUE SUPERCOMPETENT CELLS FOR DNA AMPLIFICATION

XL1-Blue supercompetent cells (Stratagene) were gently thawed on ice. A small aliquot of APX or C*c*P DNA (5 μl) was transferred into a pre-chilled Falcon® 2059 polypropylene tube and the cell suspension (70 μl) was placed on top and gently mixed. Reaction mixture was incubated on ice for 30 minutes, heat-shocked for 45 sec at 42 °C and placed on ice for another 2 minutes. A solution of 1 M $MgCl_2$ (70 μl) and one of 1 M $MgSO_4$ (70 μl) were added to 5 ml of LB-media; an aliquot of the solution thus obtained (700 μl) was added to the Falcon tube and mixed gently. The suspension of cells in LB-broth (775 μl) was then incubated with shaking for 60 minutes at 37 °C, 225 rpm and finally harvested using a bench centrifuge (800 x *g* for 3 minutes at 5˚ C). Part of supernatant (625 μl) was removed by pipetting and the pellet was resuspended into the remaining 150 μl. The suspension thus obtained (150 μl) was spread on either LB-Amp (for APX) or LB-Kan plate (for C*c*P) (see paragraph B.3) and incubated at 37 °C overnight. A single colony from the plate was picked and suspended into LB-media (5 ml) and the solution, supplemented with a small aliquot of a solution either 1 g/10 ml of ampicillin (5 μl) for APX or 0.5 g/10 ml of kanamycin (3 μl), was incubated with shaking at 37 °C, 225 rpm overnight. DNA was extracted from the cells following the QIAprep Spin Miniprep Kit protocol (using a microcentrifuge) from QIAGEN. A small aliquot was hence submitted for sequencing to the PNACLE service (University of Leicester).

## B.2. TRANSFORMATION INTO SG13009 OR BL21 DE3 GOLD

### COMPETENT CELLS FOR PROTEIN EXPRESSION

C*c*P was expressed in the *E. coli* strain of competent cells BL21 DE3 Gold (Stratagene), whereas APX was expressed in the *E. Coli* strain of competent cells SG13009 (Fisher Scientific). The same procedure was followed for both cases. Cells were gently thawed on ice. A small aliquot of amplified DNA (5 μl) was transferred into a pre-chilled Falcon® 2059 polypropylene tube and the cell suspension (70 μl) was placed on top and gently mixed. Reaction mixture was incubated on ice for 30 minutes, heat-shocked for 45 sec at 42 °C and placed on ice for another 2 minutes. A solution of 1 M $MgCl_2$ (70 μl) and one of 1 M $MgSO_4$ (70 μl) were added to 5 ml of LB-media; an aliquot of the solution thus obtained (700 μl) was added to the Falcon tube and mixed gently. The suspension of cells in LB-broth (775 μl) was then incubated with shaking for 60 minutes at 37 °C, 225 rpm and finally harvested using a bench centrifuge (800 x *g* for 3 minutes at 5˚ C). Part of supernatant (625 μl) was removed by pipetting and the pellet was resuspended into the remaining 150 μl. The suspension thus obtained (150 μl) was spread on either an LB-Amp-Kan plate (for APX) or LB-Kan (for C*c*P) (see paragraph B.3) and incubated at 37 °C overnight. A single colony from the plate was picked and suspended into LB-media (5 ml) and the solution, supplemented with a solution of both 1 g/10 ml of ampicillin (5 μl) and for APX and only 0.5 g/10 ml of kanamycin (3 μl) for C*c*P, was incubated with shaking at 37 °C, 225 rpm overnight. DNA was extracted from the cells following the QIAprep Spin Miniprep Kit protocol (using a microcentrifuge) from QIAGEN. A small aliquot was hence submitted for sequencing to the PNACLE service (University of Leicester).

The cell suspension was either directly used to inoculate the flasks for expression or stored in glycerol stock (50% v/v) at -80 °C.

## B.3. LB AGAR PLATES

Per litre: LB-broth (Melford) (20 g), agar (15 g) supplemented with glucose (2 g) and made up to 1 litre with water. The solution was sterilised and allowed to cool ≈55 °C before supplementing with ampicillin to a final concentration of 100 μg/ml and/or kanamycin to a final concentration of 30 μg/ml. Antibiotics were filter sterilised using 0.2 μm syringe-top filters (Acrodisc).

## B.4. LB MEDIA

Per litre: LB-broth powder (Melford) (20 g) was supplemented with glucose (Sigma) (2 g) and made to up to 1 litre with double distilled water. Sterilised by autoclave and allowed to cool to ≈55 °C before addition of antibiotics ampicillin (to a final concentration of 100 μg/ml) and/or kanamycin (to a final concentration of 30 μg/ml). Antibiotics were filter sterilised using 0.2 μm syringe-top filters (Acrodisc).

## B.5. MINIMAL MEDIA 2XM9

$Na_2HPO_4$-$7H_2O$ (25g) was mixed with $KH_2PO_4$ (6 g), NaCl (1 g) and $NH_4Cl$ (2 g). Distilled water was added up to 900 ml and the solution stirred until dissolved. Volume was adjusted to 900 ml with distilled H2O. Broth thus produced was sterilised by autoclaving. Finally the solution was implemented with sterilised

solutions of 1M $MgSO_4$ (2 ml), 20% w/v glucose (20 ml) and 1M $CaCl_2$ (100 µl). Volume was adjusted to 1 L using sterilised distilled water.

## B.6. SODIUM DODECYL SULPHATE POLYACRYLAMIDE GEL ELECTROPHORESIS (SDS-PAGE)

### B.6.1. PROCEDURE

All proteins were analysed on 15% acrylamide gels containing 4% polyacrylamide stacking gel. Gels were prepared to a thickness of 0.75 mm and run using Mini-Protein II gel systems (Bio-Rad). Samples were prepared by adding an equal volume of sample buffer and incubated at 100 °C for 5 minutes and cooled briefly on ice before being loaded onto the gel. The gels were run in SDS running buffer at 180 V until the dye front reached the end of the gel. Gels were stained by soaking in Coomassie Brilliant Blue R250 for 15 minutes and then destained by soaking in destaining buffer.

### B.6.2. RESOLVING GEL MIX

Acrylamide solution (3.25 ml), resolving buffer (1.9 ml) water (2.4 ml), 10 % ammonium persulphate (25 µl), TEMED (12.5 µl), add TEMED last and proceed immediately).

### B.6.3. RESOLVING BUFFER

Tris base (30.3 g) in 100 ml water, adjusted to pH 8.8, plus sodium dodecyl sulphate (0.66 g), made up to 160 ml with water.

### B.6.4. STACKING GEL MIX

Acrylamide solution (325 µl), stacking buffer (625 µl) water (1.5 ml), saturated bromophenol blue (2 µl), 10 % ammonium persulphate (12.5 µl), TEMED (6.5 µl, add TEMED last and proceed immediately).

### B.6.5. STACKING BUFFER

Tris base (6.05 g) in 40 ml water, adjusted to pH 6.8, plus sodium dodecyl sulphate (0.4 g), made up to 100 ml with water.

### B.6.6. SDS RUNNING BUFFER

Glycine (14.4 g), Tris-HCL (3 g) and sodium dodecyl sulphate (0.5 g) diluted to 500 ml with water.

### B.6.7. COOMASSIE BRILLIANT BLUE R250

Solution of Coomassie blue R-250 (0.1% w/v), methanol (40% v/v) and acetic acid (10%) made up in water.

### B.6.8. DESTAINING BUFFER

Solution of methanol (40% v/v) and acetic acid (10% v/v) made up in water.

### B.6.9. SAMPLE BUFFER

Solution of dithiothreitol (0.77 g), 10% sodium dodecyl sulphate (10 ml), 1 M Tris-HCl (1.25 ml, pH 6.8), glycerol (5 ml) and bromophenol blue in ethanol (0.5% w/v), diluted to 50 ml with water.

## B.7. SONICATION BUFFER A

Solution of 150 mM potassium phosphate, pH 6.5.

## B.8. SONICATION BUFFER B

Solution of 100 mM potassium phosphate, pH 8.0, 300 mM KCl and 10% v/v glycerol.

## B.9. WASH BUFFER

Solution of 100 mM potassium phosphate, pH 6.0, 300 mM KCl and 10% v/v glycerol.

## B.10. ELUTION BUFFER

Solution of 100 mM potassium phosphate, pH 4.2, 300 mM KCl and 10% v/v glycerol.

## B.11. FFQ BUFFER

Solution of 10 mM potassium phosphate pH 7.0.

## B.12. FAST PROTEIN LIQUID CHROMATOGRAPHY (FPLC) BUFFER

Solution of 10 mM potassium phosphate, pH 6.5 (C*c*P) or pH 7.0 (APX), 150 mM KCl.

## B.13. HEMIN SOLUTION

5 mg of hemin (Sigma) dissolved in 1 ml of 0.1 M NaOH.

## B.14. PHENYL-METHANE-SULFONYL FLUORIDE (PMSF) SOLUTION

34 mg of phenyl-methane-sulfonyl fluoride (Sigma) dissolved in 1 ml of propanol.

## B.15. PLASMIDS

### B.15.1. PLEICS03

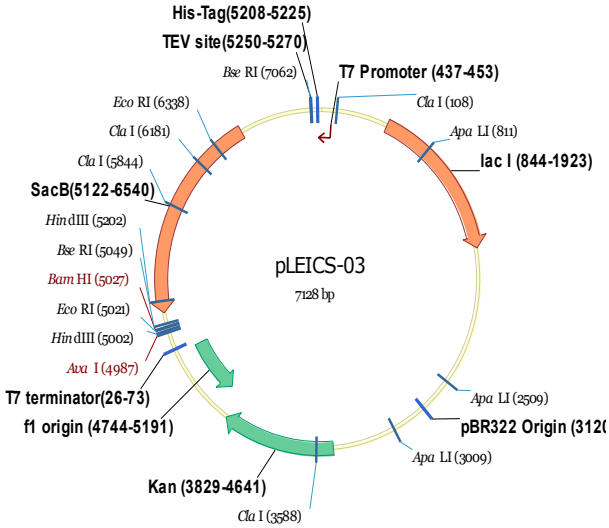


### B.15.2. PQE-30

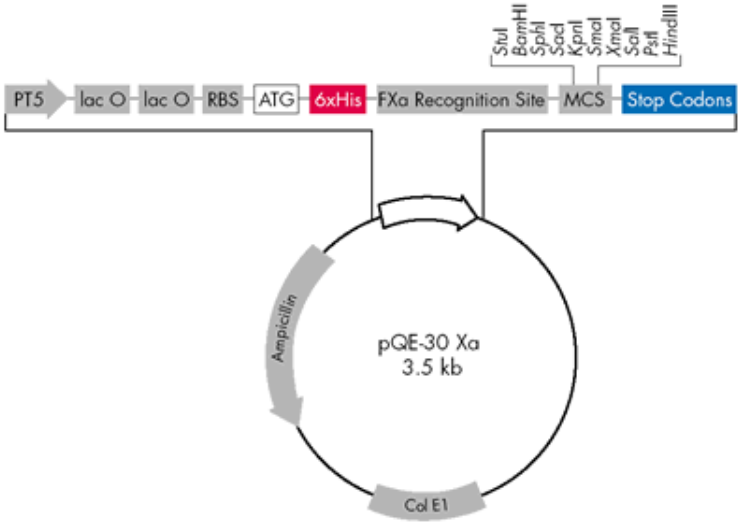
StuI
BamHI
SphI
SacI
KpnI
SmaI
XmaI
SalI
PstI
HindIII
PT5
lac O
lac O
RBS
ATG
6xHis
FXa Recognition Site
MCS
Stop Codons
Ampicillin
pQE-30 Xa
3.5 kb
Col E1

Appendix C

# BASIS OF X-RAY CRYSTALLOGRAPHY

# C.1. X-RAY DIFFRACTION

Amongst the various effects that occur upon interaction of X-ray radiation with matter, the elastic scattering is the one by which the irradiated sample is able to re-emit the received radiation as waves with the same wavelength as the incoming one. The scattering is caused by the electrons of the sample, which, upon irradiation, themselves become X-ray sources and scatter the radiation in all directions. However, when the sample is a regular and ordered solid such as a crystal, the emerging radiation beams can interfere with each other giving rise to a further phenomenon. This phenomenon, the diffraction, can be described by a simple equation, known as Bragg's law, and this is briefly discussed below.

## C.1.1. BRAGG'S LAW

Crystals are particular solids in which atoms and molecules repeat regularly. The fundamental, smallest unity of a crystal, the asymmetric unit, has no inherent symmetry or symmetry elements or, if present, they do not coincide with any symmetry operators of the crystal. The asymmetric units repeat in the crystal and the relative position of each asymmetric unit is determined by specific symmetry operations, which, all together, define the space group. The smallest set of asymmetric units, whose relative positions are determined by the space group, forms a unit cell. The unit cells repeat throughout the crystal to form a lattice (the crystal lattice).

Given a unit cell defined by the vectors $\vec{a}, \vec{b}, \vec{c}$, it is possible to identify a series of planes, also known as reticular planes, characteristic of each crystal lattice, and

determined by $\frac{\vec{a}}{h}, \frac{\vec{b}}{k}, \frac{\vec{c}}{l}$, where $h, k, l$ are integer ($h, k, l \in N$) and known as Miller's indexes.

**Figure [C. 1]: Schematic representation of Bragg's law. The incoming beams are reflected by two contiguous elements (belonging to contiguous planes *i.e.* defined by the same Miller's indexes) and because of the different position of the two elements, the scattered beams have a different path, equal to 2dsinθ (public domain image via Wikipedia Creative Commons).**

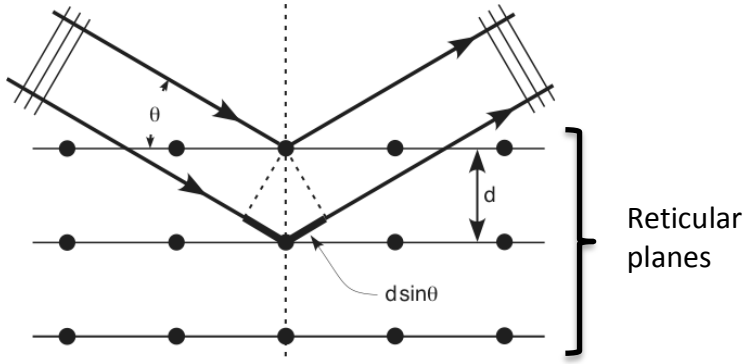


In the case of a distant source (*i.e.* when beams hitting a sample can be considered parallel), the beams scattered by two contiguous elements belonging to the same family of reticular planes (*i.e.* planes identified by the same Miller's indexes) posses a different phase that is proportional to the distance *d* between the two planes and the incident angle θ (Figure [C. 1]). In the particular case of radiation whose wavelength is comparable to the distance *d*, the various scattered beams interfere with each other. However, Bragg demonstrated that constructive interference will only occur for those beams whose phase difference correspond to an integer multiple (n) of the wavelength of the radiation:

$$n\lambda = 2d \sin\vartheta \qquad \textbf{Eq. C 1}$$

Equation Eq. C 1 is known as Bragg's law and it provides a correlation between the structure of a crystal (which determine the reticular planes) and its corresponding diffraction image.

### C.1.2. THE STRUCTURE FACTOR AND THE GENERALISATION OF DIFFRACTION

A more general approach can be used to describe the phenomenon of diffraction. It is possible to define the structure factor of an atom as the ratio between function of the scattered wave and the function of the incoming wave.

$$T(S) = \frac{E(S)}{E_0} \qquad \textbf{Eq. C 2}$$

In the simple case of two identical and contiguous atoms, the wave scattered can be described as the product of two functions:

$$T(S) = f(S) \cdot T(S)_L \qquad \textbf{Eq. C 3}$$

where $f(S)$ is the atomic structure factor and depends on the nature of the atom (*i.e.* its electronic distribution), whilst $T(S)_L$ is a function that only depends on the relative position of the two atoms and can be explicated as:

$$T(S)_L = e^{2\pi i \vec{S}\cdot\vec{r}} \qquad \textbf{Eq. C 4}$$

where $\vec{S}$ is the vector difference between the vectors of the diffracted radiation $\vec{s}$ and the incoming radiation $\vec{s}_0$, $\vec{S} = \frac{\vec{s} - \vec{s}_0}{\lambda}$, whereas $\vec{r}$ is the vector distance between the two atoms.

Extending this approach to a crystal, it simply follows that the overall structural factor $T(S)$ is the sum, over all the *n* atoms of the crystal, of the single structural factors:

$$T(S) = \sum_n f_n(S) \cdot e^{2\pi i \vec{S}\cdot\vec{r}_n} \qquad \textbf{Eq. C 5}$$

where $\vec{r}_n$ represents the positions of the various atoms with respect to the origin and $f(S)_n$ is the structure factor of each atom. It is possible to demonstrate that this summation is a mathematical series and that the series result is not zero only for certain values of the scalar product $\vec{S} \cdot \vec{r}_n$. Specifically, only when $\vec{S} \cdot \vec{r}_n = m$, with $m \epsilon N$, (conditions of von Laue), $T(S)$ assumes finite values and the diffracted waves interfere constructively to produce what is shown as a spot on the detector.

It is also possible to demonstrate that the application of the conditions of von Laue for which $\vec{S} \cdot \vec{r} = m$ results in formulating an equation that is Bragg's law. In order for the von Laue conditions to be verified, the vectors $\vec{S}$ and $\vec{r}$ must be parallel and this, geometrically, corresponds to describe a series of parallel planes, all perpendicular to $\vec{S}$, and separated by a distance $\frac{1}{S}$. In the particular case of $m = 1$, for instance, $\vec{S} \cdot \vec{r}_n = m$ can be written as $Sr = 1$ and considering that $\vec{S} = \frac{\vec{s} - \vec{s}_0}{\lambda}$, it is possible to write

$$r \equiv d = \frac{\lambda}{2 \sin \vartheta}, \qquad \textbf{Eq. C 6}$$

where $r$ is exactly *d*, the distance between two planes of the crystal lattice as expressed in Bragg's law (Eq. C 1). The Eq. C 6 is thus the same as Bragg's law, for the particular case of two contiguous planes (*i.e.* n=1). On these bases, it is possible to conclude that $T(S) = \sum_n f_n(S) \cdot e^{2\pi i \vec{S} \cdot \vec{r}_n}$ can be regarded as a general expression of Bragg's law.

## C.2. FROM DIFFRACTION TO THE STRUCTURE OF A CRYSTAL

When a crystal is irradiated with X-rays, diffraction occurs and this is described by Bragg's law. The diffraction images obtained are determined by the both the

crystal lattice and the nature of the atoms. In other words, the diffraction images carry information about the crystal structure. In principle, then, it should be possible to determine a crystal structure starting just from the diffraction images it produces when irradiated with X-ray. However, this process is not straightforward and it requires important considerations.

On the basis of mathematical considerations, it can be obtained that the structure factor $T(S)$ of a crystal (that describes the diffraction) is exactly the Fourier transform of the function of its electron density $\rho(r)$ (that describes the structure of the crystal):

$$T(S) = \Phi[\rho(r)] \qquad \textbf{Eq. C 7}$$

Eq. C 3 can be generalised to the case of a protein crystal, where the repeating unit is not a single atom, but it is a unit cell made of one or more protein molecules. The scattering factor of the crystal, then, can be written as:

$$T(S) = f(S)_m \cdot T(S)_L \qquad \textbf{Eq. C 8}$$

where $f(S)_m$ is the structure factor of the unit cell and is determined by the scattering of each single atom in the unit, whereas $T(S)_L$ is the function that only depends on the geometric properties of the crystal lattice.

Considering then Eq. C 7 and applying the theorem of the convolution, we can write:

$$T(S) = f(S)_m \cdot T(S)_L = \Phi[\rho(r)_m \cdot L(r)] = \Phi[\rho(r)_m] \cdot \Phi[L(r)] \qquad \textbf{Eq. C 9}$$

where $\rho(r)_m$ is a function of the sole electron distribution in unit cell of the crystal, and $L(r)$ is a function of the sole crystal lattice. Through Eq. C 9 and by inversion of the Fourier transform it is possible to obtain that $\rho(r)_m = \Phi^{-1}[f(S)_m]$ and $L(r) = \Phi^{-1}[T(S)_L]$.

Determination of $L(r)$ is a rather straightforward process and the function can be obtained directly by the geometric characteristic of the diffraction pattern.

However, more complex is the determination of $\rho(r)_m$, the important function that reports on the electronic density of unit cell and actually tells about the positions of the atoms in the crystal unit cell. Determining this function requires knowledge of $f(S)_m$, the structural factor of a unit cell. $f(S)_m$ is a wave and as such is determined by amplitude and phase. However, the diffraction images provide information only about the amplitude of the function, as this is determined by the square root of the intensity of the diffraction spots, but it does not provide any information about the phase of the scattered wave, which reports on the positions of the atoms in the unit cell. The limitations in the possibility to determine the phase of the structure factor is generally indicated as the *phase problem* and various methods have been developed in order to overcome this issue.

### C.2.1. DETERMINATION OF THE PHASE.

Various techniques, such as isomorphous replacement, anomalous scattering, heavy atoms method and molecular replacement, have been used to determine the phase of the unit cell structure factor and thus solve the structure of a protein. However in this thesis only isomorphous molecular replacement has been used and this is briefly discussed below.

When proteins have a very similar structure and form isomorphous crystals (*i.e.* the crystals belong to the same space group), as for the case of mutants of the same protein, for instance, it is possible to imagine that their diffraction will be very similar

too. Therefore, starting from the available protein structure it is possible to apply the Fourier transform and determine a structure factor, which possesses both information of amplitude and phase. Given the similarity between the model and the analysed crystal, it is correct to think that the calculated phases are very similar to the experimental ones. Applying thus the calculated phases to the observed amplitudes provides the missing information to the experimental structure factor, and the structure of the analysed protein can be resolved. However, the model obtained will present important differences to the experimental data and, in order to improve it and obtained a better matching, refinement is required.

### C.2.2. REFINEMENT WITH DIFFERENCE FOURIER SYNTHESIS

Usually, refinement is achieved by modifying the model so that the difference between the observed amplitude $F_o$ (*i.e.* determined by the measured diffraction intensities) and the amplitudes calculated from the model $F_c$, is minimised. Most of the work is done iteratively by software, which achieves such agreement by means of least-square minimisation or maximum likelihood methods. Nonetheless, the difference between the model and the experimental data can also be observed by means of difference Fourier method. In this case, instead of the solely observed wave amplitudes $F_o$, the inverted Fourier transform of the structural factor $f(S)_m$ ($\Phi^{-1}[f(S)]$) is calculated using the difference between the observed amplitude $F_o$, or twice its value $2F_o$, and the amplitudes calculated from the model $F_c$. In the first case (when $F_o$ - $F_c$ amplitude is used), the density function determined, $\rho(r)$ (the difference density map), will be null when $F_o = F_c$, that is to say in all the cases where

the agreement between the model and the real data is almost perfect, whereas it will be $\rho(r) \neq 0$ when the model disagree with the data. In the second case (when $2F_o$ - $F_c$ amplitude is used) $\rho(r)$ will assume positive values when $F_o = F_c$ (*i.e.* when model and data are in agreement) and also when $F_o > F_c$ (*i.e.* where the model should be). In any case, the difference density maps allow the precise identification of those areas of the model where evidently disagreement with the experimental data occurs. The model can thus be manually modified to better fit with the experimental data.

# PUBLICATIONS

(1) Gumiero, A., Metcalfe, C. L., Pearson, A. R., Raven, E. L., and Moody, P. C. E. (2011) Nature of the Ferryl Heme in Compounds I and II, Journal of Biological Chemistry 286, 1260-1268 (**Enclosed**).

(2) Gumiero, A., Murphy, E. J., Metcalfe, C. L., Moody, P. C. E., and Raven, E. L. An analysis of substrate binding interactions in the heme peroxidase enzymes: A structural perspective, *Archives of Biochemistry and Biophysics* **2010**, *500*, 13 (**Enclosed**).

(3) Barbetta, A., Gumiero, A., Pecci, R., Bedini, R., and Dentini, M. (2009) Gas-in-liquid foam templating as a method for the production of highly porous scaffolds, Biomacromolecules 10, 3188- 3192.

(4) Gumiero A., Blakeley M. P., Metcalfe C. L., Murphy E. J., Raven E. L., Moody P. C. E., (submitted), Hydrogen bonds in heme peroxidases: a Neutron and X-ray combined study on cytochrome c peroxidase.

(5) Badyal, S. K., Eaton, G., Mistry, S., Pipirou, Z., Basran, J., Metcalfe, C. L., Gumiero, A., Handa, S., Moody, P. C., and Raven, E. L. (2009) Evidence for heme oxygenase activity in a heme peroxidase, Biochemistry 48, 4738-4746.

(6) Efimov I., Badyal S. K., Metcalfe C. L., Macdonald I., Gumiero A., Raven E. L., and Moody P.C. E., (Submitted), Proton delivery to ferryl heme in a heme peroxidase: Enzymatic use of the Grotthuss Mechanism, JACS.